Czech Technical University in Prague

Faculty of Electrical Engineering

Department of Electromagnetic Field

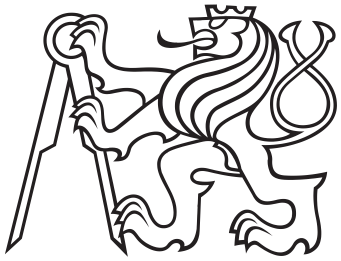

Controlling the propagation of electromagnetic waves using artificial materials

Doctoral Thesis

Ing. Michal Červený

Prague, February 2022

Ph.D. programme: P 2612 Electrical Engineering and Information Technology
Branch of study: 2601V010 Radioelectronics

Supervisor: doc. Ing. Pavel Hazdra, Ph.D.
Supervisor specialist: prof. Ing. Pavel Pechač, Ph.D.

Declaration

I hereby declare I have written this doctoral thesis independently and quoted all the sources of information used in accordance with methodological instructions on ethical principles for writing an academic thesis. Moreover, I state that this thesis has neither been submitted nor accepted for any other degree.

In Prague, February 2022 Ing. Michal Červený

Acknowledgement

In this section I would like to thank my supervisor Pavel Hazdra for giving me the best possible support I could ask for during my studies. I really appreciate his encouraging attitude, friendly manner and always positive and helpful approach.

Also I want to thank Pavel Pechač, my secondary supervisor, for his continued support. Thanks to him I started a doctoral internship abroad straight after my master's degree which helped to shape my career and this experience opened my eyes in many ways.

Also, this work would not be possible without my family and my partner Kristýna, who was very understanding when I devoted extra time to the research and projects I had to do on top of my day-to-day work and for agreeing to convert our small living room into a workshop where I could turn my ideas into reality.

Finally, I would like to thank my employer, The University of Sheffield, my previous and current supervisors namely Jonathan Rigelsford, Kenneth Lee Ford, Alan Tennant and our partners and sponsors thanks to whom I have the opportunities to work on interesting and challenging projects that I enjoy. Various published results from this research are also presented in this thesis.

Contents

1 Abstract

This thesis deals with artificial materials based on periodic structures such as frequency selective surfaces and metasurfaces. Although the list of applications can be very long, this work mainly focuses on the control of electromagnetic propagation inside buildings and the design of antennas.

In the case of buildings, signal enhancement or attenuation is required depending on the application. For instance, frequency selective surfaces are capable of spatial frequency filtering which can be useful for electromagnetic management inside secure buildings. Reconfigurable intelligent surfaces are capable of changing the scattering parameters based on the requirements with low power consumption and can improve the signal coverage inside buildings. From an antenna design perspective, antennas based on metasurfaces can provide broadband and low-profile properties. A combination of active metasurfaces with antennas can be advantageous for polarisation switching, phase control or beam-steering.

Studies from the basic concepts to complex structures are presented in this thesis: propagation measurement inside a building with and without a blocking carpet; impedance characterisation of dipole elements; optically transparent frequency selective surfaces; the design of a sparse frequency selective surface for the control of radio coverage in buildings for signal enhancement inside a room; a comparison of state-of-the-art methods for metasurface synthesis; a study of printed scattering reflectors made of a standard two-layer circuit board as well as a textile metasurface manufactured by an electroplating process; the design of a reflective switchable polarisation rotator with PIN diodes allowing adaptive beamforming or antenna polarisation switching; the design of a broadband GNSS antenna system for interference mitigation and localisation; the design of a short backfire antenna (SBA) for satellite communication based on metasurface.

Key words

GNSS antenna, Satellite antenna, Switchable metasurface, Textile metasurface, Frequency selective surface, Holographic technique, Polarisation rotator.

Abstrakt

Tato práce se zabývá problematikou uměle vytvořených materiálů na bázi periodických struktur, konkrétně frekvenčně selektivními povrchy a metapovrchy. Hlavní důraz je kladen především na ovlivňování elektromagnetického pole uvnitř budov a na návrhy konstrukcí antén.

V případě budov se v závislosti na aplikaci vyžaduje zesílení nebo zeslabení signálů v určitých částech frekvenčního spektra. K tomu lze využít frekvenčně selektivní povrchy, které umožňují prostorovou frekvenční filtraci. Rekonfigurovatelné inteligentní povrchy jsou schopny na základě požadavků měnit své odrazné parametry při nízké spotřebě energie a mohou zvýšit pokrytí signálem uvnitř budov.

Z hlediska návrhu antén mohou antény založené na metapovrších mít širokopásmové vlastnosti i při jejich nízkém profilu. Kombinací aktivních metapovrchů s anténami lze docílit přepínání polarizace, kontroly fáze nebo směrování vyzařovaného elektromagnetického pole.

V této práci jsou uvedeny studie od základních konceptů až po komplexní struktury a zahrnují následující témata: měření šíření uvnitř budovy při použití elektromagneticky neprůhledného koberce, impedanční charakterizace dipólových prvků, návrh opticky transparentního frekvenčně selektivního povrchu, návrh frekvenčně selektivního povrchu pro zesílení signálu uvnitř místnosti, srovnání metod pro syntézu metapovrchů, návrh a studie reflektorů vyrobených ze standardní dvouvrstvé desky plošných spojů a textilního metapovrchu vyrobeného galvanickým procesem, návrh reflexního přepínatelného polarizačního rotátoru s PIN diodami umožňujícího adaptivní formování paprsku nebo přepínání polarizace antény, návrh širokopásmového anténního systému GNSS pro potlačení a lokalizaci zdroje rušení, návrh SBA antény pro družicovou komunikaci na bázi metapovrchu.

Klíčová slova

GNSS anténa, Satelitní anténa, Přepínatelný metapovrch, Textilní metapovrch, Frekvenčně selektivní povrch, Holografie, Polarizační rotátor.

2 Introduction

Radio, wireless internet, mobile phones, satellite communication, deep space communication, RF (radio frequency) sensing systems, medical imaging, microwave heating; the list of devices and use cases where electromagnetic waves play a crucial role is extensive. Therefore, the ability to control electromagnetic waves is a mandatory requirement for well-functioning RF systems. As the demands for new technologies are getting more challenging, new approaches need to be found.

Very often, antennas are restricted due to space and weight limitations. This is particularly important in space applications where large parabolic reflectors [1] are expensive to transport [2, 3]. A modern aircraft contains around 30 to 50 antennas [4]. To be able to design low-profile antennas with reduced drag is therefore a mandatory requirement in aviation as many antennas are placed on the fuselage, resulting in reduced fuel economy. Furthermore, there are additional challenging requirements such as controlled multi-beam radiation patterns [5, 6] and broadband/multi-band operation [7, 8]. Power consumption [9], efficiency [10, 11] and costs of manufacturing [12, 13] are also very important factors.

These challenges can be addressed by utilising periodic structures such as frequency selective surfaces (FSS) [14] and metasurfaces [15]. Even though research of such surfaces has been very extensive, this technology has not yet been fully adopted.

There are many applications of such surfaces. Subreflectors based on FSS allow multi-band operation of parabolic antennas and radio telescopes. For instance, a space probe Voyager 1 [16] and its twin Voyager 2 [17] have an FSS subreflector in front of the main 3.66m parabolic reflector. This configuration allows dual-band (X and S) operation. The antenna works as a Cassegrain parabolic antenna at X-band where the FSS reflects, and as a prime focus radiator at S-band where the FSS is transparent [18]. The Cassini spacecraft developed for Saturn exploration had a four-band antenna based on FSS which could operate at S, X, Ku and Ka bands [19].

A very important application are radomes [20] which protect the antennas and electronics inside. Antennas need to be protected against weather conditions such as wind, moisture, rain, dust etc. Radomes should be transparent for electromagnetic waves transmitted or received by the antennas inside and should not bend the electromagnetic waves. Utilising FSSs can help solve such problems [21].

Mutual coupling reduction between antennas is a very common challenge for RF engineers; however, metasurfaces can be used to increase the isolation between planar antennas [22, 23]. Furthermore, metasurfaces allow the replacement of bulky parabolic antennas with flat reflectarrays [24, 25, 26, 27]. As an example, this technology is now being adopted on 12-unit CubeSat GomX-5 where a flat reflectarray will be unfolded in orbit in 2022 [28].

FSSs can also control electromagnetic propagation inside buildings [29] and, depending on the application, they can either suppress or enhance propagation in such environments [30, 31]. Network capabilities have grown exponentially [32]

and the more wireless networks [33] are present, the higher risk of interference [34] can be expected. Furthermore, protecting wireless networks against suspicious activity [35, 36] is extremely important for privacy protection in secure buildings [37, 38, 39]. There can be some other requirements for the FSS such as optical transparency when the surfaces are placed into window frames while the frequency response needs to remain unchanged [40, 41]. The scattering properties of the rooms can be further modified by using lossy FSSs (absorbers) [42, 43]. In addition, energy-efficient solutions are required [44] to reduce energy consumption.

The aim of this thesis was to address several topics in the area of frequency selective surfaces and metasurfaces. Particular emphasis was given to the study of FSSs used for signal enhancement or reduction inside buildings. Furthermore, the design of new metasurfaces and their synthesis was studied. Finally, the development of novel antennas based on metasurfaces was carried out.

As there are many definitions of both FSSs and metasurfaces and they often overlap, in this thesis FSS is understood as a spatial filter that affects the magnitude of the incoming wave by its transmission or reflection. On the other hand, metasurfaces are considered in this thesis as more complex structures which affect magnitude, phase but also polarisation and thus allow the control of wave fronts.

2.1 State-of-the-Art

Frequency selective surfaces (FSSs) have been studied intensively since World War II [14]. When a conductive sheet is hit by an electromagnetic wave, the wave is reflected back from the sheet and the angle of reflection is determined by Snell's law [45] (the effects of the finite sheet are not considered for simplicity [46]).

The conductive sheet (reflector) can take the shape of a parabola used in parabolic antennas [47, 48, 49, 50]. The solid parabolic reflector can be replaced by parallel rods to reduce weight and increase the wind loads [51]. This configuration only works for linearly polarised waves that are oriented parallel to the rods. It is worth noting that such surfaces can be used as a polarisation filter as the electromagnetic waves parallel to the rods are reflected while the waves with perpendicular polarisation to the rods can propagate through this structure. This principle has been used not only at microwave frequencies [52] but also in optics [53]. The distance between the rods is critical as it affects the overall performance of the antenna system such as the front-to-back ratio [54]. In this case, the reflector itself does not have any resonation frequency as the equivalent circuit of the long rods can be considered as an inductor. If the rods are split and an air gap is present, the capacitance between the rod parts and the inductance of the conductive rods will act as a resonation circuit and therefore resonation will occur. Such a reflector will work as a band-stop FSS [14].

Many types and shapes of FSSs have been published e.g., all-dielectric FFSs [55], or FSSs made purely from a conductive sheet which can be further divided into capacitive [56] and inductive FSSs [57, 58]. Hybrid versions combining dielectric and conductive structures have also been designed [59, 60, 61].

FSSs can take the geometrical shape of a Jerusalem cross [62], circular loop [63], rectangular loop [64], circular, rectangular or hexagonal patch [65] to name a few. The shapes can be interleaving and also based on a multi-layer design [66]. If an array of ring or square loops is replaced by an array of slots, the surface changes its characteristics from a band-stop filter to a band-pass filter. The combination of multi-layer complementary arrays can be used for electromagnetic interference (EMI) shielding [67, 68, 69].

With the increasing use of wireless systems, the applications and effects of FSSs inside buildings were studied. They could be an alternative solution for reducing interference. They can also increase the security of wireless networks, enhance or block signal while keeping the walls transparent to systems such as broadcast radio or cellular telephone [70]. Therefore, the impact of the walls on the FSS response was studied [71]. It was found that isolation and passive amplification capabilities of FSSs can be used in buildings for signal reduction or enhancement [72, 73].

When the inter-element spacing is greater than $\lambda/2$, grating lobes [74] occur. As the length of simple FSS shapes equals approximately $\lambda/2$, the FSS is then sensitive to oblique angles of incidence. In such cases, even though the surface can work well at a normal incidence, at oblique incidence the energy can be radiated

into unwanted directions and therefore efficiency can be reduced. Loaded elements were developed for grating lobes mitigation as they allow smaller inter-element distance [14]. On the other hand, there might be cases, where grating lobes are desirable. For instance, they can be used for propagation enhancement in corridors inside buildings [75].

Parameters such as the reflection/transmission coefficient, bandwidth and angular stability [76] are of main concern when FSSs are designed. Furthermore, FSSs can improve the antennas for satellite communications with very strict requirements for the radiation pattern [77] or they can be used for microwave lenses [78].

Metamaterials are very often designed as 2D surfaces with a small (sub-wavelength) thickness, therefore such planar structures are called metasurfaces [19]. They can be based on a resonance of a periodic layout which allow for the changing of the value of magnitude, phase and polarisation of reflected/transmitted electromagnetic waves.

Metasurfaces have mainly been designed for interaction with a plane wave or a surface wave. From a surface wave perspective, corrugated surfaces were developed. Depending on the direction of the propagation, they either support the propagation (hard surfaces) or stop the propagation (soft surfaces). Hard surfaces can be used for quasi-TEM waveguides [79, 80] or for corrugated horn antennas which have the benefits of symmetric radiation pattern and low cross-polarisation [81] in comparison with standard horn antennas. For GNSS applications choke ring antennas eliminate multipath reflections from the ground [82, 83, 84].

Taking it a step further, mushroom-type impedance surfaces [85] or electromagnetic band gap (EBG) metasurfaces [23] were developed. They consist of conductive patches that are connected to the ground layer through a vertical interconnect access (VIA). As a result, mushroom-type metasurfaces suppress the surface waves in both directions due to their symmetry [86]. As an example, they can also be used for reducing multipath interference [87]. For the antenna design, surface waves can be excited on an artificial impedance surface. Such a modulated surface can produce the desired radiation pattern [88]. This technique allows for antennas to be designed on curved surfaces and for the antennas to be integrated into complex objects [89].

A very important aspect of metasurfaces is the response to the plane wave coming from the broadband direction. Metamaterials allow for the reflecting of electromagnetic waves with a phase shift of 0° instead of 180° as it is usual for perfect electric conductors (PEC). Therefore, such surfaces are also called artificial magnetic conductors (AMC) or high impedance surfaces (HIS) [90]. Such unique behaviour has been used to design low-profile antennas [91, 92, 93].

Even though metamaterials were developed as periodic structures, the discovery of quasi-periodic structures [94] helped to extend their usage since quasi-periodic structures allow manipulation of electromagnetic wavefronts. To achieve the desired scattering behaviour, the surface first has to be synthesised to achieve the phase/amplitude distribution. Several methods for synthesis have been pub-

lished [95, 96, 88, 97]. Even though they are based on the analytical calculations and do not consider all the electromagnetic phenomena, they are very useful for metasurface design. Therefore, knowledge of their limitations is very important.

There are many practical use cases where the quasi-periodic structures are utilised. For instance, the standard curved parabolic reflectors can be replaced by flat reflectarray antennas [98, 99]. Furthermore, a focusing metasurface based on gradient AMC surface [100] and a metasurface scattering the electromagnetic waves into arbitrary angle/angles [101] have been published. The quasi-periodic metasurfaces can also be used for antenna lenses. For example, a lens antenna using three metasurface layers in front of a feeding array [102] or a high-gain short horn antenna based on metasurface-corrected lens were designed [103].

Metamaterials can be made active which means that their scattering properties can be changed dynamically [104, 105, 106]. Usually, their active components are either PIN diodes or varactor diodes. Currently, reflecting intelligent surfaces (RIS) [107, 108] based on this technology have been studied intensively for future wireless networks (6G). RIS could be used for improving the signal-to-noise ratio especially for non-line-of-sight (NLOS) radio propagation [109]. If this technology is implemented, RIS offers lower power consumption compared to standard access points with transmitters. This technology can also be used for secure wireless communication systems. As an example, a time-coding spread-spectrum RIS has been designed and published [110].

Moreover, metasurfaces can be designed for polarisation conversion. Many designs have been published for both reflective and transmissive surfaces. The transmissive polarisation rotators usually consist of a multilayer structure. For instance, designs consisting of three metallic layers based on split rings [111, 112] or split square loops [113] have been published and rotated the polarisation by 90°. Furthermore, linearly polarised waves can be converted to circular polarisation [114]. A four-layer, electronically tunable polarisation rotator allowing the polarisation tilt angle of a linearly polarised wave to be arbitrarily controlled was also presented [115]. Another tunable design consisted of four PCBs where eight conductive layers were used in total [116]. The second group of polarisation rotators are reflective metasurfaces [117]. They work as reflectors and are designed with a ground plane similar to high-impedance surfaces. They can also be based on asymmetric structures such as split-ring resonators [118, 119, 120], concentric rings [121], hexagonal split ring resonators [122], H-shaped metasurfaces [123] or L-shaped metallic patches [124] to name a few. Polarisation rotators can be also active. Designs using PIN diodes for switching of their states [125, 113] were published. Another metasurface with varactor diodes was used for frequency and polarisation reconfigurability [126].

Furthermore, metasurfaces designed on textile surfaces are another topic of interest. There are several techniques that have been published such as screen printing with conductive inks [127], weaving [128], a knitting process with conducting yarns [129] or using a liquid metal alloy embedded within a flexible silicone elastomer [130].

3 Author's Contribution

As mentioned in the State-of-the-Art section, many publications have been written in the field of frequency selective surfaces and metasurfaces. On the other hand, with the rapid development of wireless technology and the increasing number of practical challenges and applications, new solutions need to be explored. Therefore, I focused on specific topics that seemed promising for further research.

3.1 Goals of the Thesis

The goals of the thesis can be summarized into several main points and were covered in the papers presented later in the thesis:

- study of a technique for faster calculation of electromagnetic fields within resonant environments
- study of frequency selective surfaces for use in buildings
- study of techniques for metasurface synthesis
- design of novel metasurfaces
- using metasurfaces for novel antenna designs.

Despite the increasing accuracy of RF solvers and computational power, it is good practice to avoid relying on these tools only as understanding of RF techniques, theory and an educated guess are important factors. Furthermore, practical tests and measurements should be performed as some designs provide promising results in simulation software but they might not work in practice for mechanical and other reasons such as significant sensitivity to manufacturing tolerances. Therefore, in this thesis, emphasis was given to practical tests and the structures were designed with the limitations of the real world in mind. This approach, based on practical testing, is more time-consuming and expensive as it requires designing, manufacturing, measuring and when the tested structure does not meet the given criteria, this process has to be repeated until the requirements are fulfilled.

In this thesis, the covered topics were split into the following sections: Electromagnetic simulations, Electromagnetic propagation inside buildings and Antenna design based on metasurfaces.

The published articles are highlighted in ***bold and italics*** in the following text. The entire list of publications is presented at the end of this chapter followed by the articles themselves.

3.2 Electromagnetic Simulations

Modern electromagnetic components are becoming very complex in terms of the shapes to obtain the maximum performance for a given task [131]. Electromagnetic simulations based on Maxwell's equations play a crucial role in designing electromagnetic components such as frequency selective surfaces, metasurfaces and antennas. Very often, several numerical methods and approaches are combined [132]. Usually, a design starts with an analytical calculation. The final structure is then numerically calculated based on a parametric analysis to achieve the best results possible. There are many aspects that affect the final behaviour of the designed structure e.g., accuracy of numerical calculations and manufacturing, available computational resources or quality of mesh.

For instance, available RAM memory determines the amount of detail that can be considered in simulations with a finite element method (FEM). Performing full-wave electromagnetic simulations of complex, resonant and electrically large structures such as partially flooded vessels can be a challenging task. As the permittivity of water is high (approximately 80 [133]), the generated mesh of water is significantly denser in comparison to the same environment filled with air. This scenario can easily lead to memory overflow. For that reason, a new technique had to be found which was then tested with a large cavity containing 4 ports. The cavity was filled with water and the S parameters were measured and compared with the numerical results calculated by FEM method. This work was published in ***A Simplification Technique For S-parameter Calculations within Partially Loaded Resonant Cavities*** [134] (page 17). More details and measurements can be found in Appendix 6.1.

Furthermore, analytic approaches are useful for a quick and efficient solution for a design of an antenna or a reflecting surface. Usually, they provide a good approximation without the need of using complex and often expensive full-wave electromagnetic tools.

Evaluation of the Input Impedance and Impedance Quality Factor of a Dipole in Spatial and Spectral Domains [135] (page 19) was performed with EMF method and a spectral domain method. Both methods were numerically implemented in Matlab [136] and the quality factor of the dipole antenna was calculated based on the results of both methods and compared.

Moreover, two methods for metasurface synthesis were compared. The first one was based on a holographic technique, the second one calculated the reflection coefficients with susceptibility tensors. Both methods provided reflection coefficients (magnitude and phase distribution) across the metasurface based on a required scattering pattern. More information can be found in ***Metasurface synthesis using susceptibility tensors and holographic technique*** [137] (page 23).

3.3 Electromagnetic Propagation Inside Buildings

With the increasing demand for fast and reliable wireless services inside buildings, wireless networks have to adapt. There are two main concerns. The first one is the signal-to-noise ratio (SNR). With a higher SNR, faster data transfers are possible as well as using less robust modulation and coding schemes which provide higher speeds. This situation becomes even more challenging at high frequencies such as mmWaves. The second concern is the security aspect and the ability to separate networks or to block unwanted signals. Therefore, solutions for the optimisation of electromagnetic propagation inside buildings need to be found. Such a solution should not be expensive and should not consume too much power. A project named ***Wireless Friendly and Energy Efficient Buildings (WiFEEB)*** [138] (page 27) addressed such problems.

The technique of controlling the electromagnetic propagation inside a room by changing the inter-element spacing is presented in ***A Sparse FSS for Control of Radio Coverage in Buildings*** [139] (page 28). Such concepts can be further converted into switchable surfaces which are able to change the propagation properties based on a controlling algorithm. This approach can be easier and cheaper to implement compared to complex transmission metasurfaces with the same goal. Furthermore, the effect of a conductive carpet placed on a floor of a Victorian house is presented in Appendix 6.2.

Compared to walls, which can be covered by wallpaper with a desired frequency response, windows are more challenging as the optical transparency needs to be maintained. Such a combination was presented in ***An Inductive Frequency Selective Surface for Use in Secure Facilities*** [140] (page 30) and further built and measured. The photos and results from this measurement can be seen in Appendix 6.3.

Metasurfaces allow the electromagnetic waves to be scattered in a controlled way. Therefore, they can be used for controlling the propagation inside buildings and can be part of the wireless networks of future generations. Such metasurfaces can be passive or active. Active metasurfaces based on programmable electronics allow to dynamically change the scattering properties of the metasurface. When the metasurface is made of textile, it can be part of curtains which can be stretched when needed to obtain the required properties inside an indoor environment. Such a solution requires power only during the slide as the metasurface can be completely passive. For such application, a textile metasurface needs to be developed and a sufficient manufacturing process found. In this thesis, ***Study of Printed Scattering Reflectors based on Discretised Metasurface*** [141] (page 34) presents an example of a textile metasurface designed and fabricated using an electroplating process.

3.4 Antenna Design Based on Metasurfaces

Antennas play a crucial role in wireless systems. Therefore, this thesis highlights the use of metasurfaces for antenna design. The combination of metasurfaces and antennas allows for much greater possibilities and freedom during the design process.

A standard dipole placed in front of a reflector is a common setup that provides linear polarisation and can be seen in many different antenna designs. When circular polarisation (CP) and swapping between right-hand circular polarisation (RHCP) and left-hand circular polarisation (LHCP) is required, complex antenna systems such as phased crossed dipoles placed perpendicular to each other have to be built. Furthermore, such a system requires relay switching and delay transmission lines. The same functionality can be achieved with a single dipole and a switchable polarisation rotator as presented in ***Reflective Switchable Polarization Rotator Based on Metasurface with PIN Diodes*** [142] (page 39). When this novel metasurface was in the off state, it allowed for the reflection of the waveform as a standard reflector. When in the on state, it rotated the polarisation of reflected signals by 90° and based on the polarity, it controlled the phase shift of the rotated waveform by 180°.

Global navigation systems are becoming crucial for many services as they are widely used not only for positioning but also as a precision reference of time or frequency. Therefore, interference mitigation and localisation is an important safety feature of a critical RF system. For such a task, antenna arrays are needed for creating nulls in their radiation patterns to minimise the signal level of an interference. Unfortunately, not every antenna design is suitable to be placed into an antenna array. The mutual coupling between the elements can affect the input impedance as well as the radiation pattern significantly. With such an antenna system, the resulting radiation pattern could be unpredictable and interference localisation could be a very difficult or even impossible task. Therefore, a new design ***GNSS Sector Antenna for Interference Mitigation and Localisation using a High Impedance Reflector*** [143] (page 49) was developed. The combination of a metasurface and an array of two sleeve dipoles with a feeding point in the centre provided the required radiation pattern across a wide frequency range as well as a good impedance match. The construction details can be found in Appendix 6.4.

Short backfire antennas (SBFAs) became popular for their high directivity and compact dimension in comparison to antennas such as Yagi-Uda or helix antennas which require a relatively long beam. Furthermore, SBFAs are easier and cheaper to build in comparison to a parabolic dish. As an example, they were used during the Apollo missions [144] or as prime focus feed on The Green Bank Telescope [145] located in West Virginia, US. In this thesis, the reflective properties of a metasurface were used for design of a novel short backfire antenna for communication with the geostationary satellite Es'hail-2 (QO-100). The antenna consisted of a sub-reflector based on metasurface that worked as a power divider and a phase

shifter, and allowed for the creation of a rotating field (circular polarisation). The antenna also contained a high impedance which made it possible to reduce the height of the sub-reflector above the main reflector. This antenna was designed with ease of manufacture in mind. Therefore, a simple patch as a feeder was used which reduced the need for a complex feeding network with a power divider and a phase shifter. Furthermore, the complex manufacturing process of dipoles with baluns was mitigated in this design. Even though this antenna can be used for other services, the main motivation was to design a new antenna for ham-radio community. For this reason, the antenna had to be compact as many amateur radio operators have limited space for their antennas. The proposed design is presented in ***Compact Uplink RHCP 2.4GHz Short Backfire Antenna for Geostationary Amateur Radio Satellite Es'Hail-2 (QO-100)*** (page 54). Further details on the construction can be found in Appendix 6.5.

3.5 List of Publications

- **Conferences:**
  - J. M. Rigelsford and **M. Cerveny**, "A simplification technique for s-parameter calculations within partially loaded resonant cavities," in 2016 Progress in Electromagnetic Research Symposium (PIERS), 2016, pp. 4673–4674, doi: 10.1109/PIERS.2016.7735719.
  - **M. Cerveny**, K. L. Ford, and A. Tennant, "Metasurface synthesis using susceptibility tensors and holographic technique," in Loughborough Antennas Propagation Conference (LAPC 2017), 2017, pp. 1–4, doi: 10.1049/cp.2017.0297.
  - J. M. Rigelsford, K. L. Ford, **M. Cerveny**, and sixteen more authors., "Wireless Friendly and Energy Efficient Buildings (WiFEEB)," in PIERS 2015 in Prague Abstracts, Jul. 2015, p. 1674.
  - **M. Cerveny** and J. M. Rigelsford, "An inductive frequency selective surface for use in secure facilities," in 2015 Loughborough Antennas Propagation Conference (LAPC), 2015, pp. 1–4, doi: 10.1109 /LAPC.2015.7366073.
  - **M. Cerveny**, J. M. Rigelsford, and R. J. Langley, "A sparse FSS for control of radio coverage in buildings," in 2016 IEEE International Symposium on Antennas and Propagation (APSURSI), 2016, pp. 1449–1450, doi: 10.1109/APS.2016.7696431.
  - **M. Cerveny**, K. L. Ford, and A. Tennant, "Metasurface synthesis using susceptibility tensors and holographic technique," in Loughborough Antennas Propagation Conference (LAPC 2017), 2017, pp. 1–4, doi: 10.1049/cp.2017.0297.
  - **M. Cerveny**, K. L. Ford, and A. Tennant, "Study of Printed Scattering Reflectors Based on Discretised Metasurface," in 2020 14th European Conference on Antennas and Propagation (EuCAP), 2020, pp. 1–5, doi: 10.23919/EuCAP48036.2020.9136042.
- **Journals:**
  - **M. Cerveny** and P. Hazdra, "Evaluation of the input impedance and impedance quality factor of a dipole in spatial and spectral domains," Radioengineering, vol. 26, no. 4, Art. no. 4, 2017.
  - **M. Cerveny**, K. L. Ford, and A. Tennant, "Reflective Switchable Polarization Rotator Based on Metasurface With PIN Diodes," IEEE Transactions on Antennas and Propagation, vol. 69, no. 3, Art. no. 3, 2021, doi: 10.1109/TAP.2020.3026883.

  - **M. Cerveny** and P. Hazdra, "GNSS Sector Antenna for Interference Mitigation and Localization Using a High-Impedance Reflector," IEEE Antennas and Wireless Propagation Letters, vol. 19, no. 10, Art. no. 10, 2020, doi: 10.1109/LAWP.2020.3013910.

- **Journals - submitted:**

  - **M. Cerveny** and P. Hazdra, "Compact Uplink RHCP 2.4GHz Short Backfire Antenna for Geostationary Amateur Radio Satellite Es'Hail-2 (QO-100)".

- **Journals - contribution on measurement:**

  - A. Vallecchi, R. J. Langley, and A. G. Schuchinsky, "Bistate Frequency Selective Surfaces Made of Intertwined Slot Arrays," IEEE Transactions on Antennas and Propagation, vol. 65, no. 6, Art. no. 6, 2017, doi: 10.1109/TAP.2017.2689025.

The list of citations can be found in Appendix 6.6 (page 96).

A Simplification Technique For *S*-parameter Calculations within Partially Loaded Resonant Cavities

Jonathan M. Rigelsford[1] and Michal Cerveny[2]

[1]Department of Electronic & Electrical Engineering
The University of Sheffield, Mappin Street, Sheffield, S1 3JD, UK
[2]Department of Electromagnetic Field, Czech Technical University
Technická 2, 166 27 Praha, Czech Republic

Abstract— Wireless sensor networks are being deployed for engine health monitoring on marine vessels, which enables longer periods of time between engine servicing while reducing the risk of component failure. Due to the nature construction of such vessels this type of wireless sensor network must be able to operate within a highly resonant environment. To ensure reliability of suitable communication systems electromagnetic modelling can be performed. Several techniques are available for such modelling including ray tracing, finite element method, method of moments, and FDTD based methods. Each has its own relative merits and disadvantages including, material characterisation, computational time and required memory.

This work considers a technique for reducing the numerical complexity of finite element method calculations within a resonant cavity under normal and partially flooded scenarios. Computational resources required to calculate electromagnetic fields within a cavity scenario when water is present are considerably higher than for the equivalent empty model. Simulations have been experimentally validated using a cylindrical four port resonant cavity (see Figure 1) having internal dimensions of 1 m × 0.2 m. Two methods are presented to reduce this additional computational burden. Consider the cavity shown rotated by 90° and filled with 100 mm of water. Firstly we consider a 55 mm thick slab of water below which we use an open boundary, allowing us to ignore the cavity below this point. Secondly we consider a very thin layer of water (0.1 mm thick) representing the surface of the water above an open boundary.

Figure 2 shows a comparison between simulated and measured *s*-parameter data for the two methods proposed. Additionally, simulated full-wave results for the 100 mm of water calculated using time domains over within CST Microwave Studio are shown. It can be seen that simulated results are in good agreement with the measured experimental data. The proposed techniques

Figure 1: The experimental 4-port resonant cavity.

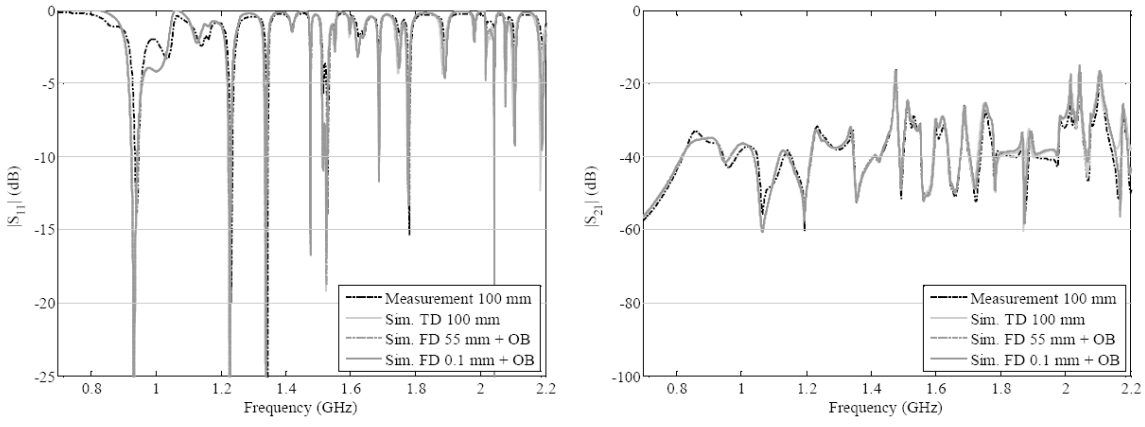

(a) (b)

Figure 2: A comparison between simulated and measured data (a) $|S_{11}|$ and (b) $|S_{21}|$ for the cavity filled with 100 mm of water.

reduce the computation time and memory requirement from 6 hr 3 min and 104.6 GB RAM, to 2 hr 11 min and 56.3 GB RAM for the 55 mm water layer above an open boundary, to just 7 min and 4.7 GB RAM for the thin layer model above an open boundary. The thin layer method is therefore 52 times faster than the equivalent full wave method and requires 22 times less system memory.

Evaluation of the Input Impedance and Impedance Quality Factor of a Dipole in Spatial and Spectral Domains

Michal CERVENY, Pavel HAZDRA

Dept. of Electromagnetic Field, FEE, Czech Technical University, Technicka 2, 166 27 Prague, Czech Republic

cervemi5@fel.cvut.cz, hazdrap@fel.cvut.cz

Submitted May 5, 2017 / Accepted August 7, 2017

Abstract. *In classic antenna analysis, there exist several methods of calculating input impedance when the source distribution of an antenna is known. The well-known induced EMF method, based on spatially distributed currents, is typically applied for this purpose and, thereby, serves as a reference for this research. Conversely, the spectral domain method takes the opposite approach for the input impedance and is evaluated using a far-field pattern. This paper compares the induced EMF method and the spectral domain method. Furthermore, the quality factor of the dipole antenna, based on the impedance variation with frequency, is calculated for both methods. This study shows that the induced EMF method and the spectral domain method are in close agreement.*

Keywords

Dipole, input impedance, quality factor, spatial domain, spectral domain, EMF method

1. Introduction

Quality factor Q [1] is one of the most fundamental characteristics of an antenna because of its connection to a bandwidth [2]. There are many ways to evaluate quality factor Q, both in the time [3] and frequency domains [4].

The most popular method is probably the one based on input impedance frequency changes [1], [4]. If the distribution of currents on an antenna is known, the input impedance, and, consequently, quality factor Q [4], can be evaluated by the complex power balance in the spatial domain. This approach is known as the induced EMF method or the Poynting vector method [5].

Another way to determine Q is by spectral analysis, which is, in turn, based on the integration of the radiation pattern in visible and invisible space [6–8]. Integration in visible space (over real angles), which is well-known and demonstrated in the literature [5], facilitates the classic calculation of the radiation resistance of an antenna. A less well-known fact is that extending the integration to invisible space (complex angles) also allows the information pertaining to the reactance to become available thanks to the special properties of the radiation pattern as explained in [6].

In this paper we study the quality factor Q of a thin dipole from its input impedance by both methods, i.e., in the spatial and spectral domain method. The source current is prescribed as sinusoidal (one-term approximation which permits the semi-analytical evaluation of the background integrals).

2. The Induced EMF Method

When considering a thin linear antenna oriented in the z-axis, the input impedance (referred to current maximum) is given by the following double spatial integral [9]:

$$Z = \frac{\mathrm{j}30}{k\left|I_0\right|^2}\iint_{zz'}\left[k^2 I(z)\cdot I(z') - \frac{\partial}{\partial z}I(z)\frac{\partial}{\partial z'}I(z')\right]\frac{\mathrm{e}^{-\mathrm{j}kR}}{R}\mathrm{d}z\mathrm{d}z' \tag{1}$$

where the current is assumed as:

$$I = I_0 \sin[k(\frac{L}{2} - |z|)] \tag{2}$$

where k is wavenumber and L is dipole length respectively. The wire radius a is incorporated in the thin-wire kernel by

$$R = \sqrt{(z-z')^2 + a^2}\ . \tag{3}$$

The result of (1) is available in closed form [5] and is used as a reference.

3. Spectral Domain Method

The spectral domain approach considers a z-oriented thin-strip dipole of length L and width w. However, it was shown [7] that thin-strip and small-radius dipoles are electromagnetically equivalent when

$$a = \frac{w}{\mathrm{e}^{\frac{3}{2}}} \approx \frac{w}{4.48}. \tag{4}$$

Hence, the above equation allows a comparison to be made between the thin-wire and thin-strip structures which is subsequently used to calculate the results.

The thin-strip current is assumed to be constant along the dipole width:

$$I = \frac{I_0}{2w} \sin\left[k\left(\frac{L}{2} - |z|\right)\right]. \tag{5}$$

Following the approach from [7], the far-field pattern is a Fourier transform of (5):

$$F = \frac{kZ_0 I_0}{(2\pi)^2} \frac{\sin\frac{k_y w}{2}}{\frac{k_y w}{2}} \frac{\cos\frac{k_z L}{2} - \cos\frac{kL}{2}}{k^2 - k_z^2} \tag{6}$$

where k_y and k_z are vector propagation constant components and $k^2 = k_y^2 + k_z^2$. Consequently, the real and imaginary parts of the input impedance are given by [6]:

$$R = \frac{2Z_0 k}{\pi^2} \int_0^k \frac{\left(\cos\frac{k_z L}{2} - \cos\frac{kL}{2}\right)^2}{k^2 - k_z^2} \cdot \left[\int_0^{\sqrt{k^2 - k_z^2}} \left(\frac{\sin\frac{k_y w}{2}}{\frac{k_y w}{2}}\right)^2 \frac{\mathrm{d}k_y}{\sqrt{(k^2 - k_z^2) - k_y^2}}\right] \mathrm{d}k_z, \tag{7}$$

$$X = \frac{2Z_0 k}{\pi^2} \left\{ \int_0^k \frac{\left(\cos\frac{k_z L}{2} - \cos\frac{kL}{2}\right)^2}{k^2 - k_z^2} \left[\int_{\sqrt{k^2 - k_z^2}}^{\infty} \left(\frac{\sin\frac{k_y w}{2}}{\frac{k_y w}{2}}\right)^2 \frac{\mathrm{d}k_y}{\sqrt{k_y^2 - (k^2 - k_z^2)}}\right] \mathrm{d}k_z - \int_k^{\infty} \frac{\left(\cos\frac{k_z L}{2} - \cos\frac{kL}{2}\right)^2}{k_z^2 - k^2} \left[\int_0^{\infty} \left(\frac{\sin\frac{k_y w}{2}}{\frac{k_y w}{2}}\right)^2 \frac{\mathrm{d}k_y}{\sqrt{k_y^2 + (k_z^2 - k^2)}}\right] \mathrm{d}k_z \right\}. \tag{8}$$

The numerical evaluation of these integrals will be discussed in Sec. 5.

4. Quality Factor

For the purpose of this paper, we use a well-established definition of the quality factor based on the variation of the input impedance with frequency [1], [4]:

$$Q = \frac{f}{2R_0} \left|\frac{\partial Z}{\partial f}\right|_{f=f_0}. \tag{9}$$

5. Numerical Validation

Equations (7–9) have been numerically evaluated in Matlab [10] using the rectangle method for integration. The input impedance and the untuned quality factor (9) of a dipole antenna have been investigated and compared with the analytical solution of (1).

Since equation (8) for the reactance contains the definite integrals with infinite upper limits, the numerical implementation is not straightforward making it necessary to estimate how large a number is needed to replace the infinite limits, and how many subintervals must be used to obtain a calculation with sufficient accuracy.

The initial value for the upper limits has been chosen ($N = 20\,000$) and the integrals have been calculated in 20 000 subintervals. The input impedance of a strip dipole of length L, ranging from 0.15 λ to 0.6 λ, with widths of 0.01 λ, 0.001 λ and 0.0001 λ of the dipole, are presented in Fig. 1 which depicts both the EMF method and the spectral domain method.

It can be seen that the input reactance for both methods, in particular the short dipole, is very similar for $w = 0.01$ λ and 0.001 λ. The results for the longer lengths show greater variation. Furthermore, the radiation resistance R (the spectral domain method) and R_{EMF} (the EMF method) provide the same results with only negligible differences as both methods overlap perfectly for all three widths in the graph.

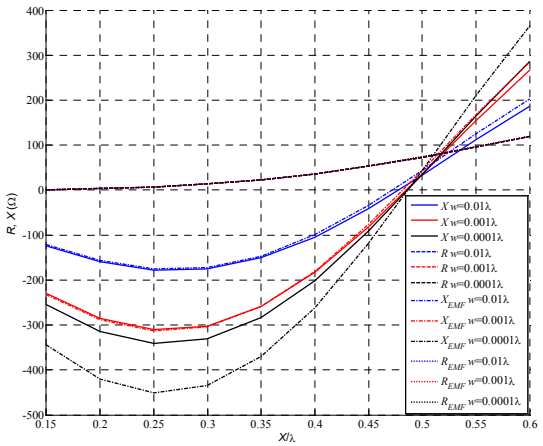

Fig. 1. Input impedance evaluated by (7), (8) of a dipole vs. electrical length for $N = 20\,000$, compared with EMF.

How the number of subintervals changes the results of the spectral domain method can be seen in the following scenario. A dipole antenna of width 0.001 λ and length 0.6 λ has been considered and the upper limit has been set again to $N = 20\,000$. For 20 000, 50 000 and 100 000 subintervals the differences between X_{EMF} and X are 16.5 Ω, 11.4 Ω and 8.7 Ω, respectively. The expected trend shows that increasing the number of subintervals decreases the differences between the two methods. From the results it can also be seen that the convergence of the rectangle method, which was used for integration, is slow and the presented differences between the two methods are given mainly by this numerical error.

The effect of the low value of the upper limit can be seen in Fig. 1 where the shifted black solid line ($w = 0.0001$ λ) does not reach the dash-dotted EMF line.

To determine which upper limit of the integrals is suitable, the convergence of the spectral domain method has been investigated. Figure 2 clearly illustrates the differences between the EMF and spectral domain methods. The input reactance is shown for the width of 0.0001 λ and lengths 0.4, 0.5 and 0.6 λ. The results are displayed for the upper limit N from 5 000 to 640 000. It can be seen that the input reactance requires the upper limit to be set to approximately 300 000 in this case where the spectral domain method converges for all three widths of the dipole.

According to the previous results, the upper limits have been set to $N = 300\,000$ and every integral has been calculated in 300 000 subintervals. Now it can be seen that both methods agree well for the width of 0.0001 λ, especially the short dipoles.

In the next step, the untuned quality factor Q has been calculated for both methods using (9) as it is presented in Fig. 4. The width of the dipole antenna is 0.01 λ, $N = 20\,000$ and 10 000 subintervals have been chosen for a faster but still reliable calculation as the graph is constructed from 60 different samples of L/λ. It can be seen

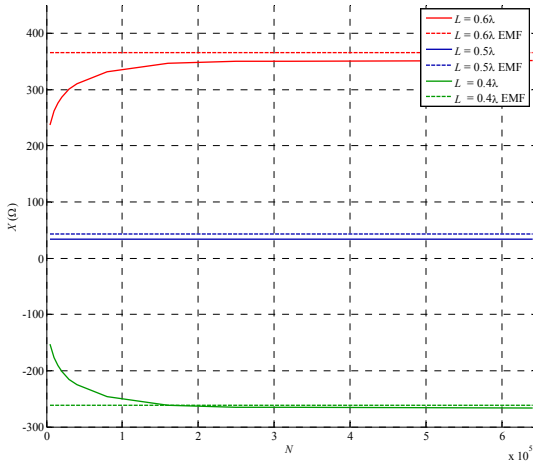

Fig. 2. Input reactance of dipoles of varying lengths with width 0.0001 λ versus integration limit N.

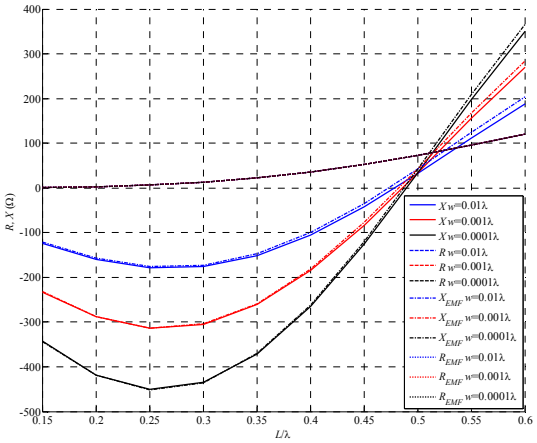

Fig. 3. Input impedance of a dipole versus electrical length, $N = 300\,000$, compared with EMF.

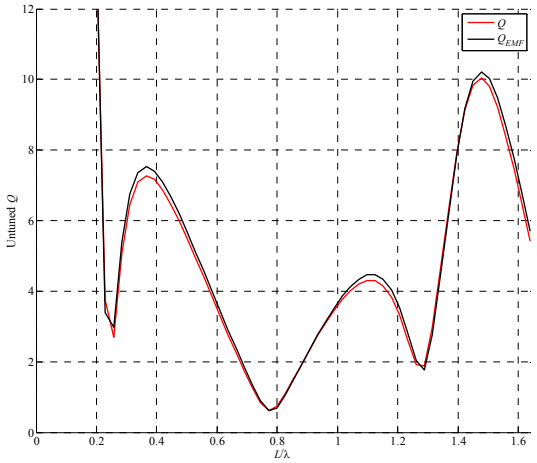

Fig. 4. Untuned quality factor of a dipole antenna of length L.

that both methods present a very similar pattern of quality factor Q.

The last graph (Fig. 5) shows the quality factor Q of a dipole antenna ($L = 0.5$ λ) for both methods versus the width of the antenna. Moreover, the results of the closed-form equation for radiation Q are displayed for comparative purposes [11]. The well-known fact that wider dipole antennas have a lower quality factor can be seen in the figure. In this case, the same settings that were used in previous calculations have been used when calculating the Q factor.

The differences between the results can be caused by several factors. The first is the previously mentioned numerical error in the integration where an increased number of subintervals is required and, unfortunately, it will cause a significant increase in the calculation time. Thus, future work could incorporate more advanced techniques for the numerical evaluation of integrals. Secondly, the Induced EMF method is only valid for very thin dipoles in terms of wavelength which is also true for the calculation of the equivalent radius in (8).

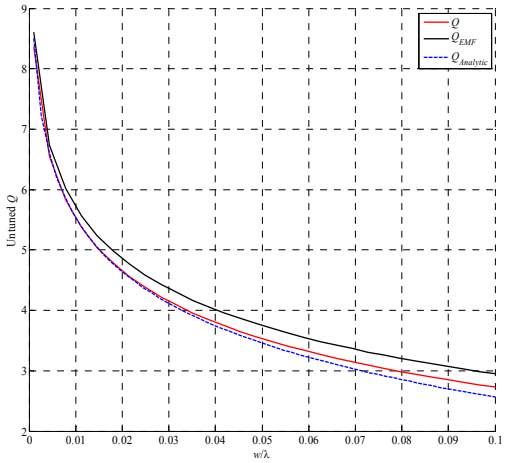

Fig. 5. Quality factor of a dipole antenna of width *w*.

6. Conclusion

In this paper we have studied two completely different methods for the calculation of the complex input impedance of a dipole antenna. The first one (EMF method) is based on spatially distributed currents on a thin dipole while the second one (spectral domain method) evaluates the input impedance from a far-field pattern obtained by the Fourier transform of the current's density. While the radiation resistance in the spectral domain method can be easily calculated with a classic numerical approach, the reactance requires more effort as the integrals with infinite upper limits need to be evaluated.

For the numerical calculation of the reactance, the infinite upper limits have been replaced by a finite number. From our graphs it can be seen that the number can be estimated via a convergence of the results. Furthermore, the number of subintervals can be estimated when the characteristics calculated by the EMF method are known. The disadvantage of this numerical approach lies in the calculation time, as it can take several days for a ubiquitous, generic PC to complete the calculations. In order to improve the accuracy and the computation time more advanced integration techniques are required.

In conclusion, the upper limit can be lower for thicker dipoles. When a calculation of a thin dipole is required, a higher upper limit has to be set. To maintain the accuracy of the results, the number of subintervals has to be increased appropriately, especially for dipoles longer than 0.4 λ.

The quality factor of the dipole antenna has been calculated by both methods and the results are in close agreement.

Finally, from the application point of view, for its simplicity and closed-form, the induced EMF method is more convenient for determining dipole impedance and consequently, the quality factor.

Acknowledgments

This work has been supported by the project 17-00607S "Complex Artificial Electromagnetic Structures and Nanostructures".

References

[1] YAGHJIAN, A. D., BEST, S. R. Impedance, bandwidth and Q of antennas. *IEEE Transactions on Antennas and Propagation,* 2005, vol. 53, no. 4, p. 1298–1324. DOI: 10.1109/TAP.2005.844443

[2] CAPEK, M., JELINEK, L., HAZDRA, P. On the functional relation between quality factor and fractional bandwidth. *IEEE Transactions on Antennas and Propagation,* 2015, vol. 63, no. 6, p. 2787–2790. DOI: 10.1109/TAP.2015.2414472

[3] CAPEK, M., JELINEK, L., VANDENBOSCH, G. A. E., HAZDRA, P. Time domain scheme for stored energy evaluation. In *IEEE International Symp. on Antennas and Propagation & USNC/URSI National Radio Science Meeting.* Vancouver (Canada), 2015, p. 1706–1707. DOI: 10.1109/APS.2015.7305242

[4] CAPEK, M., JELINEK, L., HAZDRA, P., EICHLER, J. The measurable Q factor and observable energies of radiating structures. *IEEE Transactions on Antennas and Propagation,* 2014, vol. 62, no. 1, p. 311–318. DOI: 10.1109/TAP.2013.2287519

[5] JORDAN, C. *Electromagnetic Waves and Radiating Systems.* 2nd edition, Prentice Hall, 1968. ISBN: 10: 0132499959

[6] RHODES, D. R. On a fundamental principle in the theory of planar antennas. *Proceedings of the IEEE*, 1964, vol. 52, no. 9, p. 1013–1021. DOI: 10.1109/PROC.1964.3231

[7] RHODES, D. R. On the stored energy of planar apertures. *IEEE Transactions on Antennas and Propagation,* 1966, vol. 14, no. 6, p. 676–683. DOI: 10.1109/TAP.1966.1138801

[8] TIWARI, A. K., PODDAR, D. R., DAS, B. N. On the equivalent radius of a radiating slot in impedance calculations. *Progress In Electromagnetic Research,* 2007, vol. 74, p. 47–56. DOI: 10.2528/PIER07041904

[9] HAZDRA, P., CAPEK, M., MASEK, M., LONSKY, T. An introduction to the source concept for antennas. *Radioengineering,* 2016, vol. 25, no. 1, p. 12–17. DOI: 10.13164/re.2016.0012

[10] MathWorks. [Online] Cited 2017-01-20. Available at: www.mathworks.com

[11] HAZDRA, P., CAPEK, M., EICHLER, J., MAZANEK, M. The radiation Q-factor of a horizontal λ/2 dipole above ground plane. *IEEE Antennas and Wireless Propagation Letters,* 2014, vol. 13, p. 1073–1075. DOI: 10.1109/LAWP.2014.2329421

About the Authors ...

Michal CERVENY received his M.Sc. from the Czech Technical University (CTU) in Prague in 2014. He is working towards his Ph.D. focused on the behavior of metasurfaces for RCS limitation.

Pavel HAZDRA received his M.Sc. and Ph.D. from the Czech Technical University (CTU) in Prague in 2003 and 2009, respectively and was appointed an Associate Professor in 2012. His research interests include antenna and EM theory, computational electromagnetics and special prime-feed antenna structures.

Metasurface synthesis using susceptibility tensors and holographic technique

Michal Cerveny, Kenneth Lee Ford, Alan Tennant

Dept. of Electronic and Electrical Engineering, University of Sheffield, Sheffield, S1 3JD, UK, Email: m.cerveny@sheffield.ac.uk

Keywords: Metasurface, susceptibility tensor, holographic technique, scattering.

Abstract

For a conventional, conducting surface, Snell's law applies such that the incident and reflected waves have the same angle to the surface normal. Two methods are studied in this paper that allow the design of planar metasurfaces which reflect wavefronts to prescribed directions. Two techniques are investigated; the first is based on the calculation of electric and magnetic susceptibility tensors and the second uses a holographic technique.

1 Introduction

Controlling electromagnetic scattering via metasurfaces is a topic of current interest both in acaemia and industry. Applications of metasurfaces include antennas, antenna arrays, lenses and controlled electromagnetic wave scattering such as cloaking.

In this paper we study two different methods to allow the design of planar metasurfaces. Our preliminary investigations concentrate on the design of surfaces which do not conform to standard specular scattering behaviour as described by Snell's law (Fig. 1). The first method is based on calculation of electric and magnetic susceptibility tensors whereas the second method is based on a holographic technique. Both approaches are compared for plane wave to plane wave scattering from a theoretical perspective.

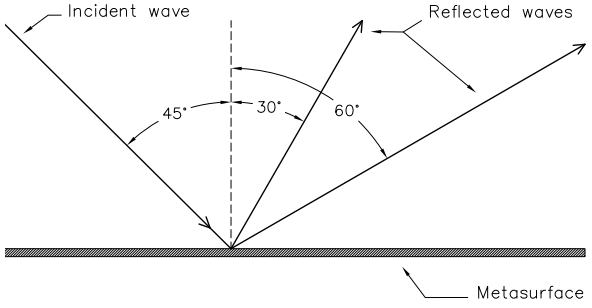

Fig. 1: Non-Snell's law scattering concept

2 Synthesis based on susceptibility tensors

This method [1, 2] describes the surface via susceptibility tensors in the spacial domain and offers closed-form solutions. In this method the synthesis defines susceptibility tensors $\chi_{ee}(\boldsymbol{\rho})$, $\chi_{mm}(\boldsymbol{\rho})$, $\chi_{em}(\boldsymbol{\rho})$ and $\chi_{me}(\boldsymbol{\rho})$ for an arbitrary specified reflected and transmitted plane wave where $\boldsymbol{\rho} = x\hat{\boldsymbol{x}} + y\hat{\boldsymbol{y}}$. The metasurface is normal to the z-axis and the differences between the E or H fields on either side of the surface are defined as

$$\Delta E_x^t = E_x^t - (E_x^i + E_x^r) \tag{1}$$

and the average fields are defined as

$$\Delta E_{x,av} = \frac{E_x^t + (E_x^i + E_x^r)}{2}, \tag{2}$$

where the subscripts t, i, r denote transmitted, incident and reflected fields.

Then the electric and magnetic fields on either side of the metasurface are defined as

$$\begin{aligned}\begin{pmatrix} -\Delta H_y \\ \Delta H_x \end{pmatrix} &= j\omega\epsilon \begin{pmatrix} \chi_{ee}^{xx} & \chi_{ee}^{xy} \\ \chi_{ee}^{yx} & \chi_{ee}^{yy} \end{pmatrix} \begin{pmatrix} E_{x,av} \\ E_{y,av} \end{pmatrix} \\ &+ j\omega\sqrt{\epsilon\mu} \begin{pmatrix} \chi_{em}^{xx} & \chi_{em}^{xy} \\ \chi_{em}^{yx} & \chi_{em}^{yy} \end{pmatrix} \begin{pmatrix} H_{x,av} \\ H_{y,av} \end{pmatrix}\end{aligned} \tag{3}$$

$$\begin{aligned}\begin{pmatrix} \Delta E_y \\ -\Delta E_x \end{pmatrix} &= j\omega\mu \begin{pmatrix} \chi_{mm}^{xx} & \chi_{mm}^{xy} \\ \chi_{mm}^{yx} & \chi_{mm}^{yy} \end{pmatrix} \begin{pmatrix} H_{x,av} \\ H_{y,av} \end{pmatrix} \\ &+ j\omega\sqrt{\epsilon\mu} \begin{pmatrix} \chi_{me}^{xx} & \chi_{me}^{xy} \\ \chi_{me}^{yx} & \chi_{me}^{yy} \end{pmatrix} \begin{pmatrix} E_{x,av} \\ E_{y,av} \end{pmatrix},\end{aligned} \tag{4}$$

where ω is an angular frequency, ϵ is free-space permittivity, μ is permeability, χ is electric/magnetic susceptibility of the surface. As it can be seen the equations contain 16 unknown susceptibility components. These equations can be simplified and as a result only 4 susceptibility components have to be calculated for both TE and TM polarizations.

TM polarization:

$$\chi_{ee}^{xx} = \frac{-\Delta H_y}{j\omega\mu E_{x,av}} \tag{5}$$

$$\chi_{mm}^{yy} = \frac{-\Delta E_x}{j\omega\mu H_{y,av}} \tag{6}$$

TE polarization:

$$\chi_{ee}^{yy} = \frac{\Delta H_x}{j\omega\mu E_{y,av}} \tag{7}$$

$$\chi_{mm}^{xx} = \frac{\Delta E_y}{j\omega\mu H_{x,av}}. \tag{8}$$

Then reflection and transmission coefficients for TM polarization are given by

$$T_x = \frac{4 + \chi_{ee}^{xx}\chi_{mm}^{yy}k^2}{(2 + jk\chi_{ee}^{xx})(2 + jk\chi_{mm}^{yy})} \tag{9}$$

$$R_x = \frac{2jk(\chi_{mm}^{yy} - \chi_{ee}^{xx})}{(2 + jk\chi_{ee}^{xx})(2 + jk\chi_{mm}^{yy})} \tag{10}$$

and for TE polarization the coefficients are defined as

$$T_y = \frac{4 + \chi_{ee}^{yy}\chi_{mm}^{xx}k^2}{(2 + jk\chi_{ee}^{yy})(2 + jk\chi_{mm}^{xx})} \tag{11}$$

$$R_y = \frac{2jk(\chi_{mm}^{xx} - \chi_{ee}^{yy})}{(2 + jk\chi_{ee}^{yy})(2 + jk\chi_{mm}^{xx})}. \tag{12}$$

In the results this method is referred to as *Method I*.

3 Holographic technique

The holographic technique [3, 4, 5] is used to compute an interference pattern, or computer generated hologram (CGH), from a simulated incident wave-front and a back-propagated representation of the desired scattered wave-pattern. Illumination of the CGH by the incident wave-front then results in an approximation the prescribed scattered wave-front.

Firstly, an interference pattern (CGH) that would exist on the scattering surface, S, has to be calculated. The field on S due to the incident field is $I(x, y)$ and the field on S due to the scattered field (traveling in backward direction) is $S^*(x, y)$. Then the interference pattern can be written as

$$H(x, y) = S^*(x, y)I(x, y). \tag{13}$$

If we now create the surface H* and illuminate it from the angle θ_i we get

$$\begin{aligned} R(x, y) &= I(x, y)H^*(x, y) \\ &= S(x, y)I^*(x, y)I(x, y) = S(x, y). \end{aligned} \tag{14}$$

Hence, the surface S will radiate as an aperture (or phased array) with a field distribution $S(x, y)$ and produce a main beam in the direction given by θ_s.

Practically, a computer-generated hologram is calculated using equation 13 where the incident and reflected plane waves are expressed as exponentials:

$$H(x) = e^{jk\sin(\theta_i)x}e^{-jk\sin(\theta_s)x}. \tag{15}$$

In the results this method is referred to as *Method II*.

4 Surface reflection coefficient comparison

Both methods have been implemented in Matlab scripts and compared in terms of the phase and magnitude of the reflection coefficients on the surface S. For the simulations the surface S was a square of side 10 λ. For simplicity, but without loss of generality, spatial variations were only considered in one linear (x) direction.

Firstly, an example conforming to Snell's law was considered. In this special case the surface should perform as a simple perfect magnetic conductor (PMC) reflector, so no surface variation in phase or magnitude is expected. The angle of incidence was chosen 45° and the results are shown in Fig. 2 and Fig. 3.

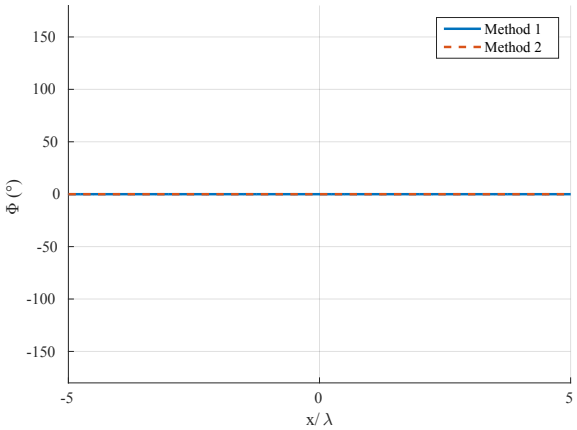

Fig. 2: Reflection phase - Angle of incident/reflected wave: 45°/45°

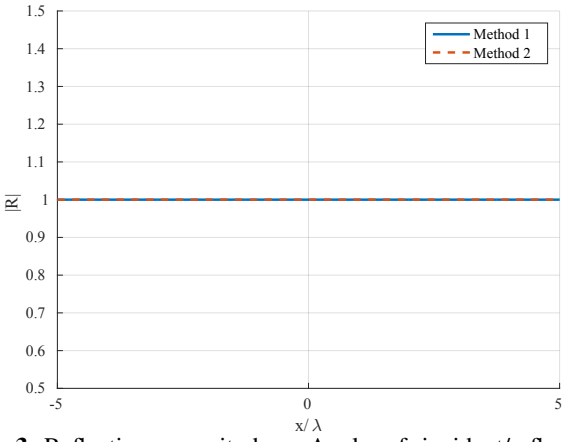

Fig. 3: Reflection magnitude - Angle of incident/reflected wave: 45°/45°

The second scenario considers the angle of incidence 45° and the angle of reflection 60°.

The phase of the reflection coefficient is shown in Fig. 4. Despite the fact that the *Method II* based on holographic technique has linear response of phase of the reflection coefficient and the phase of the *Method I*, based on susceptibility tensors, is more complex, both methods are similar.

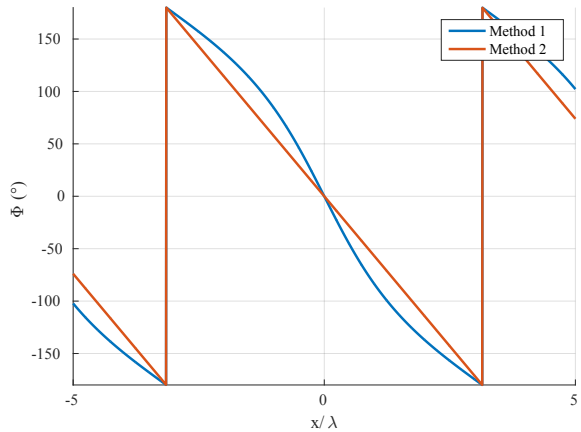

Fig. 4: Reflection phase - Angle of incident/reflected wave: 45°/60°

The holographic method assumes that the magnitude of reflection coefficient $|R|$ equals 1 everywhere on the surface in comparison with the *Method I* where the magnitude is changing on the surface as shown in Fig. 5.

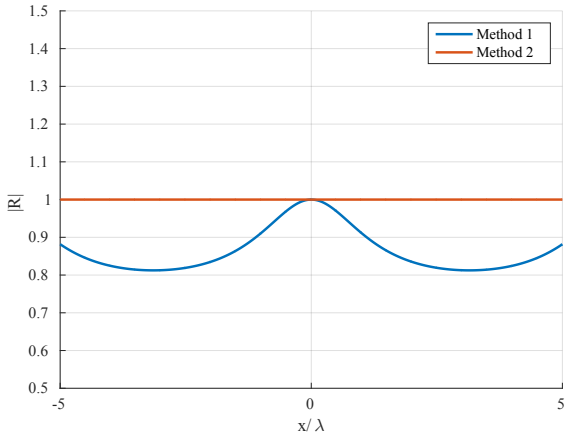

Fig. 5: Reflection magnitude - Angle of incident/reflected wave: 45°/60°

The last scenario is an example in which the incident wave-front is at 45° and the desired reflected wave-front is at 30°. The phase responses from both methods are again very similar as shown in Fig. 6. However, it can be seen in Fig. 7 that *Method I* has $|R|$ greater than 1.

From a practical perspective the phase differences between the two methods do not have a great impact as it is difficult to make a continuous surface in terms of phase. In addition, any practical surface will have to be optimized for a few discrete levels.

Furthermore, it is difficult to manufacture a surface with varying magnitude of reflection coefficient across the surface. It can be seen that for the *Method I* the surface should attenuate (second scenario) or amplify (third scenario) the incoming electromagnetic waves.

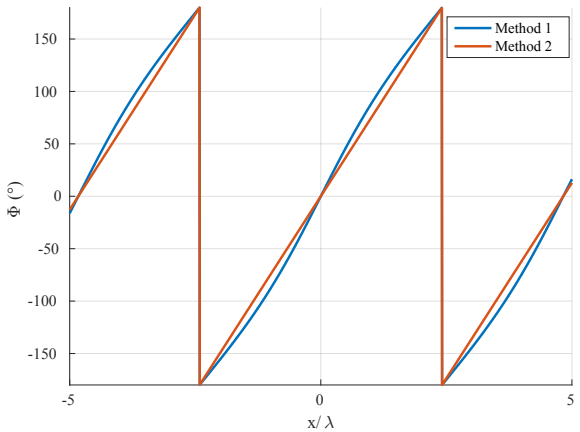

Fig. 6: Reflection phase - Angle of incident/reflected wave: 45°/30°

It is worth noting that when the magnitude of the reflection coefficient is considered to be 1 everywhere on the surface (for *Method I*), it negatively influences the side lobes [2].

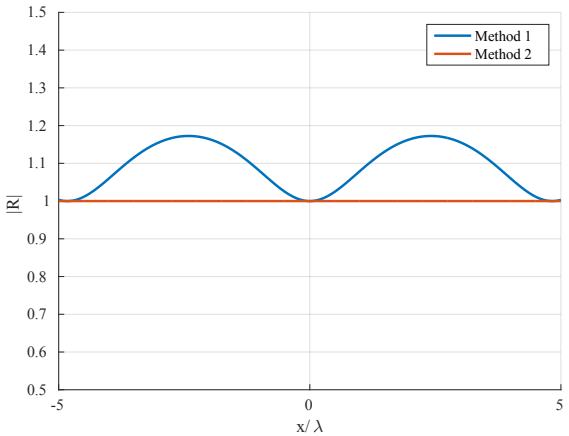

Fig. 7: Reflection magnitude - Angle of incident/reflected wave: 45°/30°

5 Far-field comparison

Far-field pattern of the surface was computed via the calculated reflection coefficients R using aperture antenna theory [6].

As it can be seen from Fig. 8, 9 and 10, all the main lobes are in the expected positions and they are effectively identical for both methods. In the first scenario, where the angles of incident and reflected wave equal 45°, the radiation patterns match completely as in this case both methods provided the same reflection coefficients. On the other hand, in the second and third scenario the near side lobes differ. Overall, it can be inferred that none of these methods is superior to the other.

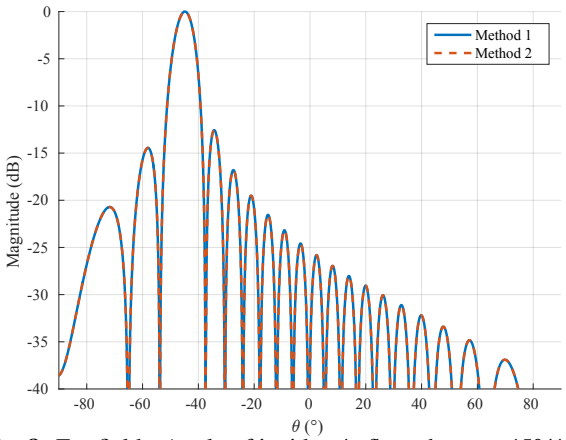

Fig. 8: Far-field - Angle of incident/reflected wave: 45°/45°

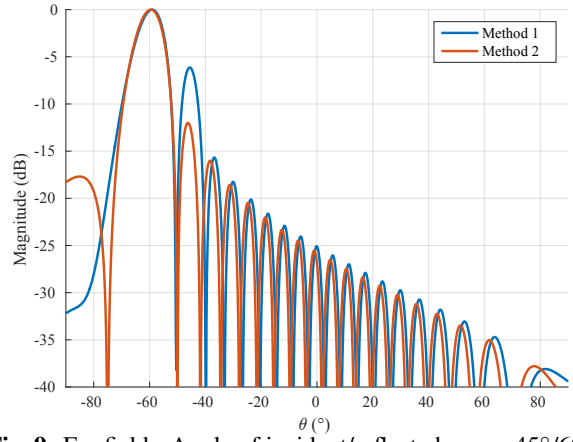

Fig. 9: Far-field - Angle of incident/reflected wave: 45°/60°

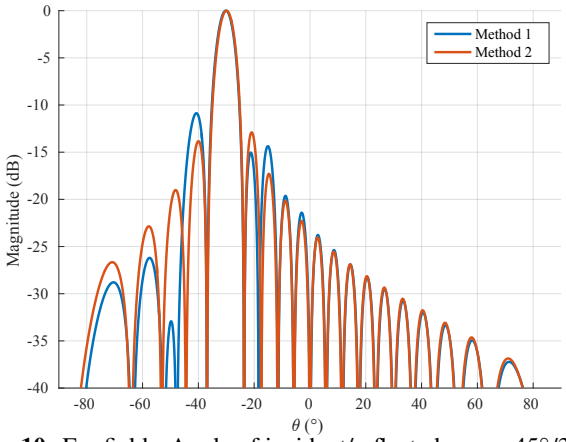

Fig. 10: Far-field - Angle of incident/reflected wave: 45°/30°

6 Conclusion

Two different methods for metasurface synthesis were studied and implemented in Matlab codes. Both methods can be used to design plane metasurfaces that do not conform to Snell's law. The results obtained show that while the holographic method changes only the phase of the surface, the method based on susceptibility tensors changes both phase and magnitude of the reflection coefficient. Furthermore, the scattering patterns were calculated and the results lead to a conclusion that nether method is superior.

Future work will consider the realisation of metasurfaces using periodic and non-periodic metallic elements above a ground plane.

7 Acknowledgements

The project was funded by the Defence science and technology laboratory (DSTL) and supported by BAE SYSTEMS.

References

[1] K. Achouri, M. A. Salem, and C. Caloz, "General metasurface synthesis based on susceptibility tensors," *IEEE Transactions on Antennas and Propagation*, vol. 63, no. 7, pp. 2977–2991, July 2015.

[2] K. L. Ford and K. Shah, "A study on the use of metasurface synthesis using electric and magnetic susceptibility," in *2016 Loughborough Antennas Propagation Conference (LAPC)*, Nov 2016, pp. 1–4.

[3] B. H. Fong, J. S. Colburn, J. J. Ottusch, J. L. Visher, and D. F. Sievenpiper, "Scalar and tensor holographic artificial impedance surfaces," *IEEE Transactions on Antennas and Propagation*, vol. 58, no. 10, pp. 3212–3221, Oct 2010.

[4] D. Sievenpiper, J. Colburn, B. Fong, J. Ottusch, and J. Visher, "Holographic artificial impedance surfaces for conformal antennas," in *2005 IEEE Antennas and Propagation Society International Symposium*, vol. 1B, 2005, pp. 256–259 vol. 1B.

[5] S. Ebadi, T. Driscoll, and D. Smith, "Visual illustrations of microwave holographic beamforming using a modulated surface-impedance metamaterial," in *2013 IEEE Antennas and Propagation Society International Symposium (APSURSI)*, July 2013, pp. 2343–2344.

[6] C. A. Balanis, *Antenna Theory*. Hoboken, New Jersey: John Wiley and Sons, 2005.

[7] E. F. Kuester, M. A. Mohamed, M. Piket-May, and C. L. Holloway, "Averaged transition conditions for electromagnetic fields at a metafilm," *IEEE Transactions on Antennas and Propagation*, vol. 51, no. 10, pp. 2641–2651, Oct 2003.

[8] J. A. Gordon, C. L. Holloway, and A. Dienstfrey, "A physical explanation of angle-independent reflection and transmission properties of metafilms/metasurfaces," *IEEE Antennas and Wireless Propagation Letters*, vol. 8, pp. 1127–1130, 2009.

Wireless Friendly and Energy Efficient Buildings (WiFEEB)

J. M. Rigelsford[1], **K. L. Ford**[1], **T. Yu**[3], **Z. Lai**[3], **R. Shiram**[1], **P. Valtr**[2], **J. Weng**[3], **Y. Wang**[3], **A. Vallecchi**[1], **H. Altan**[1], **H. Song**[3], **J. Zhang**[1], **J. Wu**[3], **M. Cerveny**[2], **W. Zhao**[3], **L. Subrt**[2], **Y. Alharbi**[1], **C. J. Davenport**[1], **P. Pechac**[2], **and R. J. Langley**[1]

[1]Department of Electronic & Electrical Engineering
The University of Sheffield, Mappin Street, Sheffield S1 3JD, United Kingdom
[2]Department of Electromagnetic Field, Czech Technical University
Technická 2, Praha 166 27, Czech Republic
[3]Ranplan Wireless Network Design Ltd., Hart Business Centre
Kimpton Road, Luton LU2 0SX, United Kingdom

Abstract— The design and construction of buildings has historically been driven by structural, functional, and aesthetic considerations. However, the working and home environment is driven increasingly by energy efficiency and electronic communications whether it be the internet, smart energy metering (to be implemented by 2020), telephone, computer data or multimedia exchange and in future by remote patient monitoring (Telecare) and Assisted Living. The wireless performance of building design is not understood and the construction industries do not consider wireless system performance in their designs or specifications despite the rapid employment of metal skins and windows and facades containing metallised layers for energy conservation, both of which are a significant problem for wireless signal propagation. Hence there is a significant need to understand the performance of buildings and construction materials for efficient energy consumption and for the efficient propagation of radio waves.

Security in buildings is also a very important issue. The emergency services require pervasive communications at 400 MHz throughout the built environment. In addition City Managers and built environmental professionals will monitor a range of different aspects of the environment, including factors such as air and water quality, noise and lighting levels as well as human and vehicular movement and behaviour. Most of these services are wireless and they will significantly increase in number and importance in the future. Wireless control is also used in buildings for lighting, heating and energy control systems. The growth of use of these systems into new and demanding applications requires greater efficiency in use of the electromagnetic spectrum and control of wireless interference both within and between adjacent buildings and in the environment itself. Hence, modern buildings must be designed to be wireless radio-friendly and energy efficient whether they are hospitals, schools, offices, prisons or the home.

This paper presents the key findings resulting from the WiFEEB project and addresses how buildings and the built environment can be both energy efficient and wireless friendly. Our objectives have been to develop and verify the new concept of the wireless friendly, energy efficient building. The wireless propagation properties of building and insulation materials have be assessed and are presented. The same properties must be measured for building structures such as walls (internal and external), floors, facades and window systems. These properties have been evaluated from 400 MHz to 20 GHz to include both current and future wireless networks and systems. Results are given resulting from the bespoke optimisation of CAD tools that combine wireless propagation models with energy efficiency models producing a complete model for the built environment. New innovative construction materials such as glass and steel fibre reinforcement are studied and new architectural designs investigated to improve wireless signal propagation while maintaining energy efficiency. Techniques are presented to control wireless propagation within buildings, namely frequency selective surfaces (FSS), smart wall units, adaptive antennas and scattering surfaces. Finally, results of several case studies will be given.

ACKNOWLEDGMENT

This work is a deliverable of WiFEEB — Wireless Friendly and Energy Efficient Buildings, a Marie Curie Industry-Academia Partnerships and Pathways (IAPP) project grant agreement 286333.

A Sparse FSS for Control of Radio Coverage in Buildings

M. Cerveny
Dept. of Electromagnetic Field,
Czech Technical University in Prague,
Technická 2, 166 27 Praha, Czech Republic
cervemi5@fel.cvut.cz

J.M. Rigelsford, R.J.Langley
Department of Electronic & Electrical Engineering,
The University of Sheffield,
Sheffield, S1 3JD, UK
{j.m.rigelsford, r.j.langley} @sheffield.ac.uk,

***Abstract*— Frequency selective surfaces have been widely used to control radio propagation within buildings. In this paper we consider the application of a sparse FSS for improved coverage of radio signals between two isolated adjacent rooms. The scattering lobes which will occur from a sparse FSS design can therefore be exploited to alter the coverage pattern within the second room.**

Keywords— frequency selective surfaces, sparse array.

I. INTRODUCTION

Over the last decade numerous papers have been published considering radio propagation within the built environment for the improvement of performance, capacity, or security [1-8]. Such systems have been envisaged for use within buildings to limit the transmission of unwanted communications systems (e.g. Wi-Fi for SINR improvement), whilst transmitting wanted signals such as cellular, radio, TV, emergency services etc. Several authors have considered transmissive Frequency Selective Surfaces (FSS) for controlling the propagation of radio frequency (RF) signals into and within buildings including those published in [2-8]. FSS are large area filters based on periodic arrays of metallic or dielectric elements capable of operating with low-pass, band-pass, band-stop and high-pass frequency characteristics [9]. Alternative methods for controlling radio propagation within buildings have included intelligent walls [10], passive antenna based systems [11] and comb reflection FSS [12] for deployments in corridors.

In this paper we consider the application of using a sparse FSS for improved coverage of radio signals between two adjacent rooms. Classical FSS design typically uses inter-element spacing d of less than our equal to half the wavelength λ of the operational frequency. Wide incidence angle frequency response performance can be achieved when $d << \lambda$. By using a sparse FSS we exploit the scattering lobes which will naturally occur for an array of elements having an spacing of greater than wavelength. It is proposed that this technique can be used to mitigate the requirement multiple FSS panels within a wall which can be costly to install, or a large aperture which will have no frequency selectivity.

II. DESIGN & SIMULATION

This work considers two adjacent rooms separated by a perfectly isolating metallic wall. All other walls are considered as open boundaries. For analysis purposes a dual polarized inductive pass-band FSS has been considered. The FSS comprises and array of 4x4 inter-woven inductive cross elements as illustrated in Fig. 1. A standard design ($d = \lambda/2$) and sparse design ($d = \lambda$) have been considered. The pass-band region has been designed to operate at 3.695 GHz. The crosses are formed by two orthogonal slots of width $W = 2$mm, cut into a 1mm thick aluminium plate. Due to the effects of mutual coupling the lengths of the slots were optimized to ensure that resonance occurred at the same frequency for both designs. No further attempts to optimize the unit cell performance have been made as such techniques are widely known and are in the available literature, such as [9].

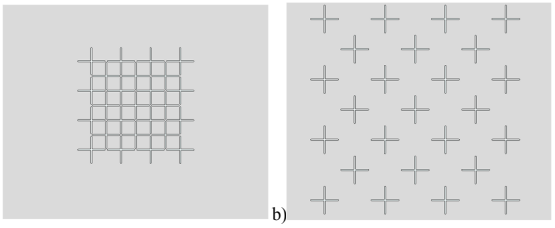

Fig. 1. Fig. 1. Illustrations of a 4x4 inter-woven simple inductive cross FSS for a) standard design $d = \lambda/2$ and b) sparse design $d = \lambda$.

Simulations have been performed using CST Microwave Studio. The unit cell designs were analysed with the Frequency Domain Solver with periodic boundaries and were performed using a tetrahedral mesh over a frequency range from 1 to 6 GHz using 1001 points, with two Floquet modes being considered. Electric field strength simulations were performed using the Time Domain solver over a frequency range of 0 to 4.5 GHz. E-Field monitors were used at the resonant frequency of the FSS at 3.695 GHz.

III. RESULTS

The characteristics of a standard $d = \lambda/2$ and a sparse $d = \lambda$ inductive cross FSS have been considered. A comparison between the transmission |T| and reflection |R| characteristics of the normal and sparse FSS unit cells are given in Fig. 2. It can be seen that the sparse design has a significantly narrower bandwidth performance when compared to the standard design. Fig. 3 shows the Electric field strength coupled between two

This work was financially supported by WiFEEB - Wireless Friendly and Energy Efficient Buildings, a Marie Curie Industry-Academia Partnerships and Pathways (IAPP) project grant agreement 286333.

perfectly isolated rooms using the pass-band FSS for both the standard and sparse designs. An increase in electric field strength of over 10 dB can be clearly seen near to the isolating wall in the sparse FSS design.

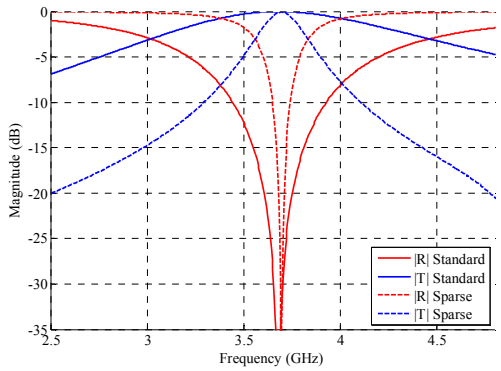

Fig. 2. A comparison of transmission |T| and reflection |R| response of standard ($d = \lambda/2$) and sparse design ($d = \lambda$) inductive cross FSS structures.

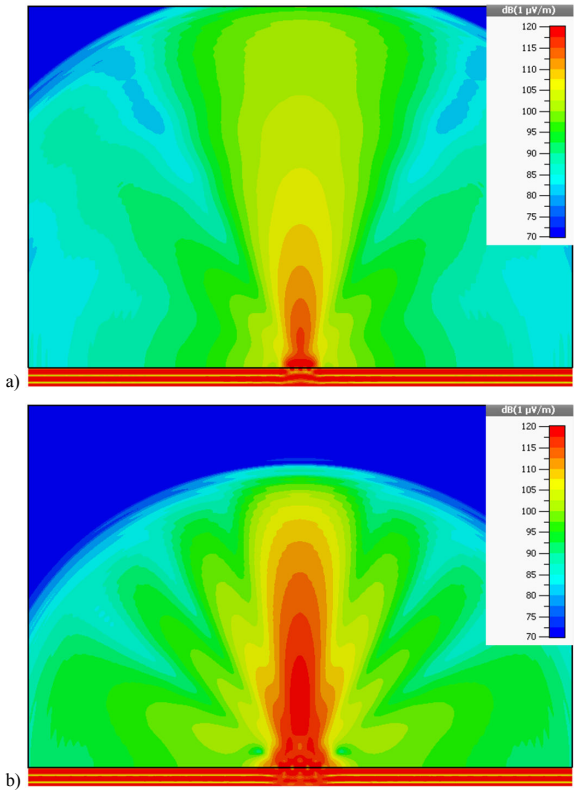

Fig. 3. Electric field strength coupled between two perfectly isolated rooms using a 4x4 inter-woven inductive cross FSS. Inter-element spacing of a) $\lambda/2$ and b) ~λ.

IV. Discussion and Conclusions

This paper has considered the application of using a sparse FSS for improved coverage of radio signals between two adjacent rooms. By using a sparse FSS we exploit changes in the radiated power pattern which will naturally occur for an array of elements having an spacing of greater than wavelength. It is proposed that this technique can be used improve coverage performance close to wall in which the FSS aperture is places. Furthermore, it mitigates the requirement of large aperture that will have no frequency selectivity, or multiple FSS panels within a wall which can be costly to install. Two isolated adjacent rooms connected by a 4x4 interspaced inductive cross FSS have been simulated. Results presented in Fig. 3 show this hypothesis to be true with an increase in electric field strength of over 10 dB being visible near to the isolating wall. Disadvantages of the proposed technique are well documented [9] and include reduced band-pass/band-stop performance for a given FSS element, although this can be mitigated by using broadband unit cell designs. It is with these in mind that the authors believe that this is an area worthy of further investigation and are not claiming that it is suitable or relevant for all practical scenarios.

References

[1] M.J. Neve, A.C.M Austin and G.B. Rowe, "Electromagnetic engineering for communications in the built environment," in *6th European Conference on Antennas and Propagation (EUCAP), 2012*, pp.1-5, 26-30 Mar 2012.

[2] M. Raspopoulos and S. Stavrou, "Frequency selective surfaces on building materials - air gap impact," Electronics Letters, vol. 43, pp. 700-702, Jun 2007.

[3] N. Qasem and R. Seager, "Frequency selective wall for enhancing wireless signal in indoor environments," in Antennas & Propagation Conference, 2009. LAPC 2009. Loughborough, 2009, pp. 573-576.

[4] G. I. Kiani, K. L. Ford, L. G. Olsson, K. P. Esselle, and C. J. Panagamuwa, "Switchable Frequency Selective Surface for Reconfigurable Electromagnetic Architecture of Buildings," IEEE Transactions on Antennas and Propagation, vol. 58, pp. 581-584, Feb 2010.

[5] M. Yang and A. K. Brown, "A Hybrid Model for Radio Wave Propagation Through Frequency Selective Structures (FSS)," IEEE Transactions on Antennas and Propagation, vol. 58, pp. 2961-2968, Sep 2010.

[6] L. Subrt, D. Grace, and P. Pechac, "Controlling the Short-Range Propagation Environment Using Active Frequency Selective Surfaces," Radioengineering, vol. 19, pp. 610-617, Dec 2010.

[7] M. Raspopoulos and S. Stavrou, "Frequency Selective Buildings Through Frequency Selective Surfaces," IEEE Transactions on Antennas and Propagation, vol. 59, pp. 2998-3005, Aug 2011.

[8] L. Subrt, P. Pechac, K.L. Ford, R.J. Langley and J.M. Rigelsford, "Controlling coverage for indoor wireless networks using Metalized Active FSS Walls," in , 19th Asia-Pacific Conference on Communications (APCC), pp.496-500, Aug 2013.

[9] B.A. Munk, "Frequency-selective surfaces: Theory and design," Wiley, New York, 2000.

[10] L. Subrt and P. Pechac, "Intelligent walls as autonomous parts of smart indoor environments," in Communications, IET , vol.6, no.8, pp.1004-1010, May 2012.

[11] J.M. Rigelsford, K.L. Ford and L. Subrt, "A passive system for increasing cellular coverage within energy efficient buildings," in , 8th European Conference on Antennas and Propagation (EuCAP), pp.614-615, Apr 2014.

[12] C.J. Davenport and J.M. Rigelsford, "Design of comb reflection frequency selective surface for interference reduction in corridors of buildings," in Electronics Letters , vol.49, no.23, pp.1478-1479, Nov. 7 2013.

An Inductive Frequency Selective Surface for Use in Secure Facilities

Michal Cerveny[1], Jonathan M. Rigelsford[2]
[1] Dept. of Electromagnetic Field, Czech Technical University, Technická 2, 166 27 Praha, Czech Republic
cervemi5@fel.cvut.cz
[2] Department of Electronic and Electrical Engineering, The University of Sheffield, Sheffield, S1 3JD, UK
j.m.rigelsford@sheffield.ac.uk

***Abstract*—Limiting mobile phone usage while maintaining a viable communication link for the emergency services can be crucial for secure facilities such as prisons. This paper presents the design of an inductive frequency selective surface (FSS) with a pass-band operating from 380 to 420 MHz covering the TETRA frequency band used by emergency services in Europe. The FSS is designed to attenuate signals in the mobile cellular frequency bands aiming to inhibit the operation of contraband mobile phones. The paper considers how the optical impact of the design can be reduced, thereby enabling its usage as a window covering, and the subsequent effect on the surface's band-pass and band-stop performance.**

Index Terms—Frequency selective surface, propagation, measurement.

I. INTRODUCTION

The use of contraband mobile phones within prisons is an increasing global phenomenon, enabling criminals to continue unlawful activity, including organizing drug deals, assassinations and witness harassment [1, 2]. According to official statistics, 7301 mobile phones or SIM cards were found in UK prisons during 2012 [3]. TETRA (Terrestrial Trunked Radio) is the communications protocol used by emergency services in over 100 countries worldwide and operates between 380 MHz and 420 MHz. It is widely used by Police forces, paramedics, fire brigades, and special response units (including riot police), as well as other government agencies. Historically, cellular mobile phone networks have operated on clearly defined frequency bands. For example, AMPS and D-AMPs was used on systems operating between 806-880 MHz; GSM 900 operates between 880-960MHz; GSM1800 operates between 1710-1880 MHz; and UMTS 1900-2170 MHz. With the adoption and roll out of LTE and 4G systems cellular network operators have over 40 designated frequency bands which can be used across the existing spectrum allocation and with the addition of newer bands including Band 38 which covers 2570-2620 MHz [4, 5]. Wi-Fi operates in the 2.4 GHz and 5.8 GHz ISM bands and can be used for peer to peer communication on mobile devices.

There are four major issues to consider when designing a system to limit the usability of mobile cellular networks for secure facilities such as prisons. Firstly, mobile phones are capable of sending and receiving messages even when signal strength is low, due to the high sensitivity of the receivers which is typically in the range -110 to -130 dBm. Secondly, the high number of mobile base stations means coverage is vast, so it is probably that many prisons in the UK have good quality signal [7]. Thirdly, to block signals of varying frequencies, a large band stop filter response must be utilised by the FSS, whilst allowing 400 MHz to transmit through. Finally, if the solution such as an FSS, is to be installed into a window frame, optical transparency is essential.

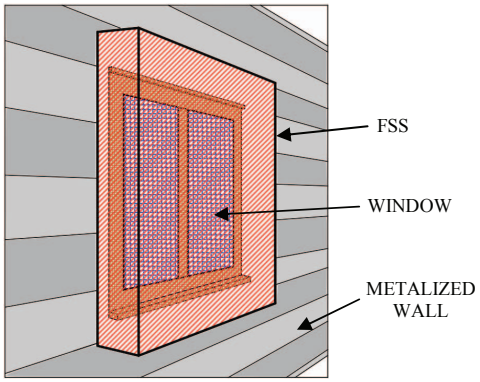

Fig. 1. Illustration of FSS mounted on a frame in front of a prison window

This paper therefore presents an inductive frequency selective surface (FSS) which can be applied externally to prison cell windows to prevent the transmission of unwanted signals from mobile phones but allows TETRA based systems to operate correctly. It is envisaged that the FSS would be mounted on a frame covering the window as illustrated in Fig. 1. In this work it is assumed that the walls of the prison are assumed perfectly isolating and can be achieved using metalized construction materials including Celotex [8] or Kingspan [9].

Energy efficient windows (e.g. K glass) typically has a transmission loss of approximately 25 dB at the frequencies of interest and could potentially be combined with the FSS to increase the level of signal attenuation at the unwanted frequency bands. Beyond the proposed design's potential for optical transparency, advantages of the proposed solution over other technologies such as jamming devices or active

capacitive FSS [6], are that an inductive FSS is cheap to manufacture as it can be self-supporting and manufactured from a single metallic sheet. Furthermore, it requires no external power supply to correctly run, reducing operating and maintenance costs and is in line with current legislative requirements (i.e. restrictions on jamming overspill for public access areas).

II. The Design & Simulation

This work considers an inductive pass-band FSS as illustrated in Fig. 2. The pass-band region has been designed to operate between 380 MHz and 420 MHz. The FSS comprises an interleaved simple cross formed by two orthogonal slots 375 mm long, of width W, cut into a 1 mm thick metal plate. To reduce the optical impact of the design, thereby enabling its usage as a window covering for a prison cell, a second design has been considered as illustrated in Fig. 3. An array of holes of radius R, spaced 25 mm apart, are inserted into the metal plate in the region between the interleaved crosses. Therefore, each unit cell will have 196 holes. The holes will act as band-pass filters and their radius can be chosen to ensure this occurs at a high frequency than that used by current mobile phone systems. For simplicity of modelling, the total number of holes in the surface remains constant and so smaller dimensions will limit the optical transparency of the design. In reality, for smaller diameter holes, a greater number of holes would be used to mitigate this effect.

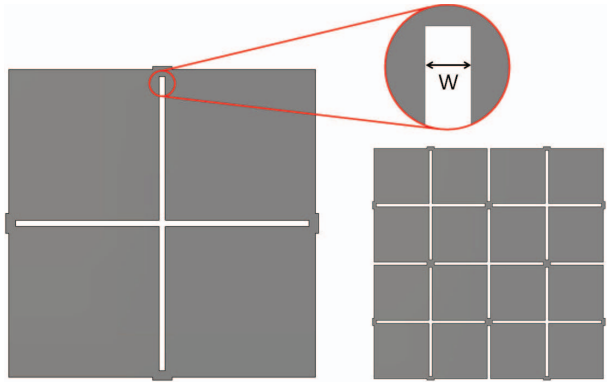

Fig. 2. Illustrations of a) simple inductive cross FSS unit cell and b) an array of 4 unit cells providing 5 interleaved cross elements.

Simulations have been performed using the Frequency Domain Solver in CST Microwave Studio [10] which is ideal for the analysis of high Q-value and periodic structures. Calculations were performed using a tetrahedral mesh over a frequency range from 0 to 3 GHz using 1001 points, with all Floquet modes being considered. For simplification of the model, the metal plate has been considered as a PEC (Perfect Electric Conductor) and periodic boundary conditions have been used. As the design is self-supporting and does not require a substrate, the slots and holes are filled with air ($\varepsilon_r = 1$).

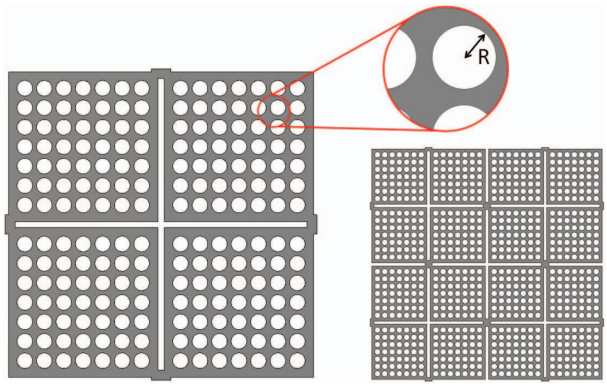

Fig. 3. Illustrations of a) simple inductive cross FSS with better optical transparency by the introduction of an array of holes between the cross arms and b) an array of 4 unit cells providing 5 interleaved cross elements.

III. Results

The characteristics of the basic inductive cross FSS (Fig. 2) and optically transparent inductive FSS (Fig. 3) have been considered. For reference, traditional cellular communication bands are highlighted in each graph, with the different colours corresponding to the following services: TETRA (light green), AMPS (yellow), GSM 900 (light blue), GSM 1800 (pink), UMTS (grey) and Wi-Fi (brown).

A comparison between the transmission |T| and reflection |R| characteristics of the FSS is illustrated in Fig. 4. The structure (Fig. 2) was analyzed with a gap width $W = 2$ mm. Results are given for the first order mode and for the maximum result obtained across all modes.

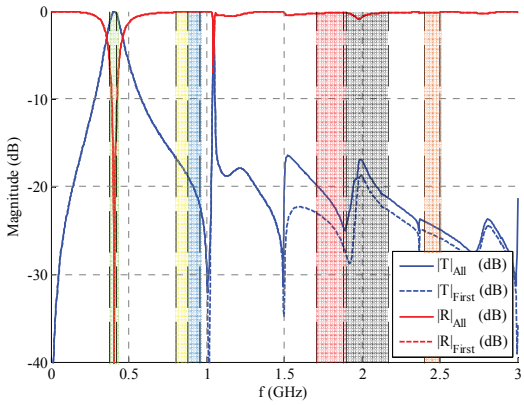

Fig. 4. Compare of transmission |T| and reflection |R| response of first mode and maximum across all modes, of the basic inductive cross FSS structure.

It can be seen that the transmission response of the first mode is dominant up to 1.5 GHz, while above this frequency the transmission response is greater due to other higher modes. The reflection response is influenced especially by the first mode because the reflection curves are overlapping.

Approximately on 1.050 GHz, spike exists in the graph. This peak does not have any detrimental effect on the performance of the FSS because the frequency of this resonance is located between of the spectral bands of interest.

Figure 5 shows a comparison of transmission |T| results of the first order mode, which were achieved by analysis of the simple inductive cross structure (Fig. 2). Results are presented for three cases for slot widths (W) of 2, 5 and 10 mm. It can be seen that the performance of the narrowest slot (2 mm) provides the greatest level of attenuation within the mobile phone bands and has the narrowest pass-band response for the TETRA band. Figure 6 presents a similar comparison for the case where the maximum transmission result obtained across all Floquet modes are considered. Again for frequencies below 1.5 GHz it can be seen that the first order mode is dominant. For both cases (Figs. 5 and 6), increasing the slot width can be seen to reduces the FSS attenuation by approximately 6 dB. For frequencies above 1.5 GHz, attenuation for the maximum |T| across all modes is typically reduced by less than 3dB within the cellular mobile bands when compared to that of the first order mode.

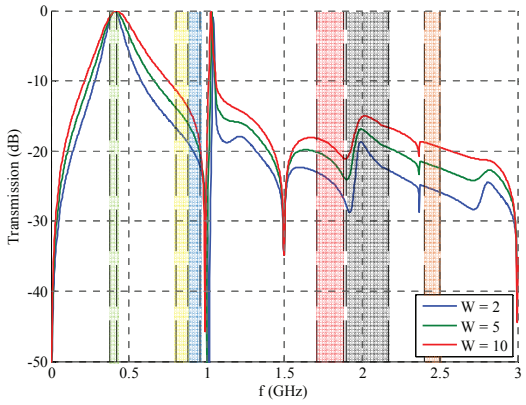

Fig. 5. Simulated $|T|_{First}$ response in dependence on the width of the gap

Figure 7 shows a comparison of transmission |T| results of the first order mode, which were achieved by analysis of the FSS when additional holes are introduced to enhance optical transparency of the surface (Fig. 3). Results are presented for three cases for hole radii (R) of 0, 5 and 10 mm. The $R = 0$ case is presented as a reference for comparison to the results presented in Figs. 5 and 6. For both Figures the slot width $W = 2$ mm. It can be seen (Fig. 7) that there is negligible difference between the cases when $R = 0$ and $R = 5$ for frequencies below 1.5 GHz and where the diameter of the hole is less than λ/20. When the hole size is increase to $R = 10$mm, the attenuation is increased in the AMPS and GSM 900 frequency bands (yellow and light blue). For the GSM 1800 and UMTS frequency bands (pink and grey) it can be seen that in general, increasing the radius of the hole improves the attenuation of the FSS. In the Wi-Fi band (brown), introduction of the holes reduces the attenuation by over 6 dB. This result could be expected for the $R = 10$ mm case as at this frequency, the diameter of the hole becomes significantly large at approximately λ/12.

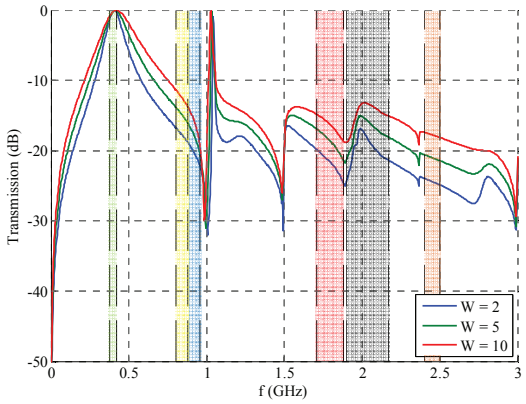

Fig. 6. Simulated frequency transmission response in dependence on the width of the gap $|T|_{All}$

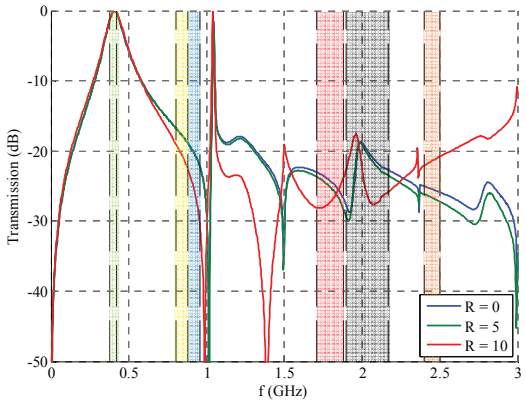

Fig. 7. A comparison of simulated $|T|_{First}$ response for various hole radii, $W = 2$

Figure 8 presents a similar comparison to that shown in Fig. 7, for the case where the maximum transmission result obtained across all Floquet modes are considered. Again for frequencies below 1.5 GHz it can be seen that the first order mode is dominant. Below 1 GHz, both results (Figs. 7 and 8), show that increasing the radius of the hole to $R = 10$ mm can be seen to improve the performance of the FSS in the AMPS and GSM 900 frequency bands (yellow and light blue). In Fig. 8 it can be seen that, for frequencies covering the GSM 1800 and UMTS frequency bands (pink and grey) increasing the radius of the hole to $R = 10$ mm reduces the FSS attenuation by approximately 1.5 dB. In the WiFi band (brown) the reduction in FSS attenuation is less than 3.8 dB.

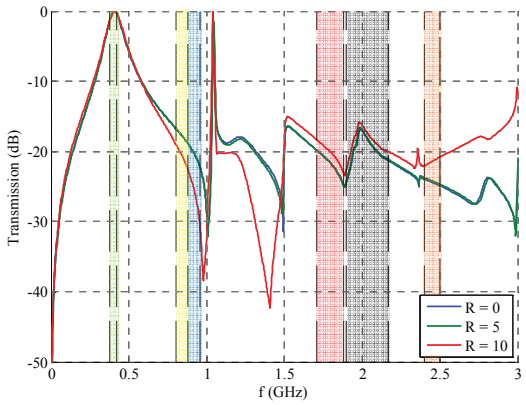

Fig. 8. A comparison of simulated $|T|_{All}$ response for various hole radii, $W = 2$.

IV. Conclusions

Limiting mobile phone usage while maintaining a viable communication link for the emergency services can be crucial for secure facilities such as prisons. In this paper we have presented the design of an inductive frequency selective surface (FSS) with a pass-band operating from 380 to 420 MHz covering the TETRA frequency band used by emergency services in Europe. The FSS is designed to attenuate signals in the mobile cellular frequency bands aiming to inhibit the operation of contraband mobile phones. The paper considers how the optical impact of the design can be reduced by the introduction of small holes between the cross elements. This enables the suitability of the design as a window covering and allowing more light to pass through the structure. The holes introduce higher order modes which can be controlled to have negligible subsequent effect on the surface's band-pass and band-stop performance. When the size of the holes becomes significant in terms of the wavelength, they become high order band-pass elements and therefore reduce the effectiveness of the FSS to attenuate signals within the mobile frequency bands. It has been shown (Fig. 7) that there is minimal difference between the performance of the inductive FSS without holes (i.e. when $R = 0$) to those obtained when $R \leq 5$ mm.

This work focuses on improving optical transparency of a passband FSS. We have considered a simple self-supporting structure which has not been optimized for element density of oblique angle of incidence performance as typical examples of how these can be achieved is well known and explained by Munk [14]. Results have been presented for three cases for slot widths (W) of 2, 5 and 10 mm, and for three cases for hole radii (R) of 0, 5 and 10 mm. Using the extremes of these parameters results in an increase in optical transparency of 46%. For a practical solution, replacing the holes with a wire mesh would further increase optical transparency.

Future work will consider how improvements in the design can be made to further increase the attenuation of unwanted signals within the cellular mobile frequency bands. This will include considering how window glass can be utilized in combination with the FSS to further improve the out-of-band filter performance over a wide range of incidence angles.

V. Acknowledgements

This work has been financially supported by Marie Curie Industry-Academia Partnerships and Pathways (IAPP) Grant Agreement 286333.

References

[1] D. Blakey. (Oct. 6, 2014). Disrupting the supply of illicit drugs into prisons - A report for the Director General of National Offender Management Service. [Online]. Available: http://www.drugscope.org.uk/Resources/Drugscope/Documents/PDF/Good%20Practice/blakeyreport.pdf

[2] (Oct. 6, 2014). Mobile Phones in Prisons – The demand and use of illicit mobile phones. [Online]. Available: http://www.government-online.net/research-brief-use-illicit-mobile-phones-prison/

[3] (Oct. 6, 2014). Recording of incidents related to mobile phones and SIM cards. [Online]. Available: https://www.gov.uk/government/uploads/system/uploads/attachment_data/file/329255/recording-incidents-mobile-phones.doc

[4] C. Geßner, "Long Term Evolution - A concise introduction to LTE and its measurement requirements," Rohde&Schwarz GmbH&Co. KG, 2011

[5] 3GPP TS 36.101, "User Equipment (UE) radio transmission and reception (Release 9)," V9.3.0, march 2010

[6] K.L. Ford, J. Roberts, S. Zhou, G. Fong and J. Rigelsford, "Reconfigurable frequency selective surface for use in secure electromagnetic buildings," *Electronics Letters*, vol.49, no.14, pp.861,863, July 4 2013

[7] J. Roberts, J. M. Rigelsford and Kenneth L. Ford, "Diffraction From Frequency Selective Surfaces for Secure Building Applications," in *Antennas and Propagation (EUCAP), 2012 6th European Conference on*, pp. 2388 - 2391, 2012.

[8] (Oct. 10, 2014). Celotex. [Online]. Available: http://www.celotex.co.uk/

[9] (Oct. 10, 2014). Kingspan. [Online]. Available: http://www.kingspan.cz/

[10] (Oct. 6, 2014). CST Microwave Studio. [Online]. Available: http://www.cst.com

[11] G.H.-H. Sung, K.W. Sowerby, M.J. Neve and A.G. Williamson, "A Frequency-Selective Wall for Interference Reduction in Wireles Indoor Environments," *IEEE Antennas Propag. Mag.*, vol. 48, no. 5, pp. 29-37, 2006

[12] J. Roberts, K.L. Ford and J.M. Rigelsford, "Secure Electromagnetic Buildings," in *Antennas and Propagation (EUCAP), 2014 8th European Conference on*, Hague, pp. 797 - 798, 2014.

[13] E.A. Parker, J.C. Batchelor, R. Chiang, A.G. Williamson, B. Sanz-Izquierdo, M.J. Neve and K.W. Sowerby, "Frequency selectively screened office incorporating convoluted FSS window," *Electronics Letters*, vol. 46, pp. 317-318, 2010.

[14] B.A. Munk, "Frequency-selective surfaces: Theory and design," Wiley, New York, 2000.

Study of Printed Scattering Reflectors based on Discretised Metasurface

Michal Cerveny, Kenneth Lee Ford, Alan Tennant
Department of Electronic and Electrical Engneering, The University of Sheffield, Sheffield, UK, m.cerveny@sheffield.ac.uk

***Abstract*—In this paper, metasurface synthesis for plane wave to plane wave scattering was studied from the practical perspective. The study was focused on the design of discretised surfaces that do not conform to standard specular scattering behaviour as described by Snell's law but allow to reflect wavefronts to prescribed directions. The results of the synthesis were compared with full-wave simulations and measurements. Furthermore, the design was adopted for testing of a textile metasurface manufactured by an electroplating process. The practical design requirements are presented.**

***Index Terms*—metasurface, electromagnetics, reflector, synthesis.**

I. Introduction

Metamaterials, which are constructed by sub-wavelength artificial particles, allow control of electromagnetic waves. They typically consist of small metallic scattering patches which are placed on a dielectric layer as illustrated in Fig. 1.

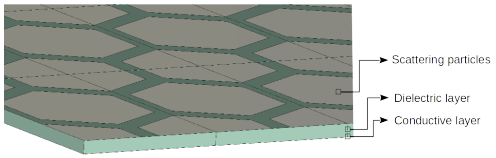

Fig. 1. Metasurface.

Metamaterials where at least one of the parameters such as dimensions, lattice size or geometry varies randomly, can be used to attenuate the specular reflection. As a result, an artificial material with randomly distributed gradients of refractive index can be designed. In contrast with a metallic plate, where the incident wave is totally reflected to the specular direction, this metamaterial provides a diffuse reflection (performing like Lambertian reflectance). As a step further, we use synthesis techniques based on susceptibility tensors further referred to as Method 1 [1], [2] and holographic technique further referred to as Method 2 [3], [4], [5], which allow to deflect an incoming wave into arbitrary directions.

Method 1 describes the surface via susceptibility tensors in the spacial domain and offers closed-form solutions. Method 2, based on the holographic technique, is used to compute an interference pattern, or computer-generated hologram, from a simulated incident wave-front and a back-propagated representation of the desired scattered wave-pattern. Both methods were compared in [6].

This paper extends this comparison and studies these methods in terms of a practical design where the continuous phase distributions obtained by synthesis need to be discretised. Furthermore, it is shown that even a very coarse discretisation can reflect the electromagnetic waves into required directions. Two discretised metasurfaces for two different manufacturing techniques were designed, manufactured, measured and the results are presented further in this paper.

II. Synthesis

Synthesis of a reflector was performed using both Method 1 and Method 2. Dimensions of the reflector in x and y directions were chosen from -5 to 5λ (10λ in total). λ is wavelength calculated for a required frequency f as $f = c/\lambda$, where c is the speed of light ($3*10^8 m/s$). The phase variation is considered only in x direction and the surface was designed for the angle of incidence of 45° and reflectance of 60°.

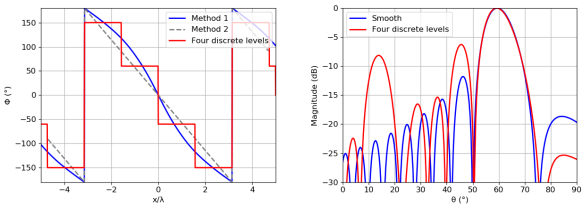

(a) Method 1: discretisation (b) Far-field comparison

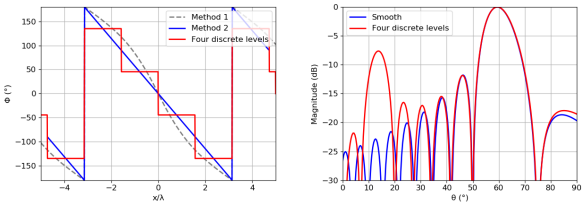

(c) Method 2: discretisation (d) Far-field comparison

Fig. 2. Effect of discretisation - Angle of incident/reflected wave: 45°/60°.

The continuous phase variation across the surface, calculated by Method 1, was further simplified into quantised regions as presented in Fig. 2a. Fig. 2b compares the obtained far-field patterns of the continuous (smooth) and discrete surface. It is shown that the discretisation increased the side lobe levels whereas the main lobe was not affected (there is only a negligible difference). The far-field pattern of the discrete surface contains a high side lobe (-6 dB) adjacent

to the main lobe. The discrete levels were calculated using an algorithm that averaged phase samples within the required region. The same algorithm was used for Method 2. As the phase variation is linear, the original phase curve intersected the discrete levels in the middle of each phase region (Fig. 2c). The far-field pattern is presented in Fig. 2d. Also in this case the main lobe was unaffected and only the side lobes were increased due to the discretisation.

III. Design of a Reflector

A design of a suitable surface such that a comparison between full-wave electromagnetic simulations and theoretical prediction based on synthesis can be carried out is presented in this section. For the electromagnetic simulations CST Microwave Studio was utilised.

For periodic structures the first step is to design a unit cell. Using this technique based on Floquet theorem, the complex reflection coefficient for arbitrary incident angles can be computed for a single cell while assuming an infinite structure illuminated by a plane wave. The phase response can be changed by altering the dimensions of the structure. It implies the limitations of the practical design as the structure and gaps cannot be too small due to manufacturing limits and also it cannot be too large as the surface needs to maintain a periodicity within the regions of constant phase.

A hexagonal structure presented in Introduction (Fig. 1) was chosen. Fig. 3 shows the reflection phase of the hexagonal unit cell providing a high impedance at 10 GHz, as denoted by the red curve. The yellow and blue curves present the maximal phase variations (-130° and 130°) used in the design. In case of 130°, one edge of the hexagon is 2.66 mm long and the gap between the hexagon patches is 0.71 mm wide. The hexagon with reflection phase of -130° has its edge 4.59 mm long and the gap 1.23 mm wide. 0.8 mm thick FR-4 material ($\epsilon_r = 4.3$) was considered.

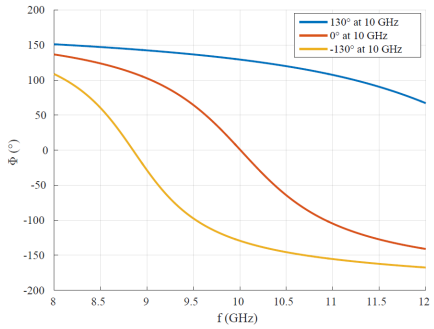

Fig. 3. Phase reflection diagram.

Based on the simulation, the maximum and minimum discrete levels were set to -130° and 130°. The other two discrete levels could then be tuned to alter the levels of the side lobes as appropriate. The final phase distribution was chosen as follows: -130°, -60°, 60° and 130° (Fig. 4a). It can be seen in Fig. 4b that the first two side lobes were set approximately 10 dB below the main lobe.

The remaining two unit cells were designed (-60° and 60°) at frequency of 10 GHz. The complete structure is shown in Fig. 5. Because of the practical reasons, discrete levels located between +/- 4.7 and 5λ were not considered for the final design and the analytic calculations were updated accordingly.

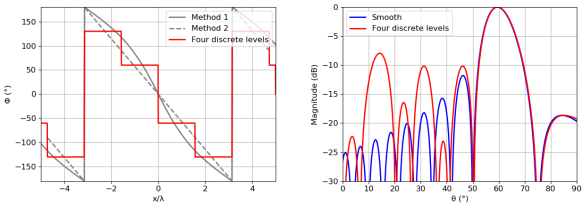

(a) Final phase distribution (b) Far-field

Fig. 4. Phase discretisation - Angle of incident/reflected wave: 45°/60°.

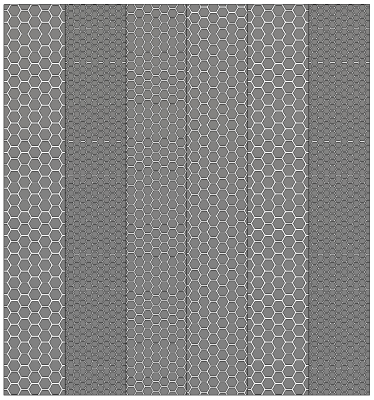

Fig. 5. Metasurface.

Fig. 6 presents the far-field comparison between the full-wave simulation and the updated analytic prediction. The angle of incidence is 45° and the main response of the surface is at 60° as predicted analytically.

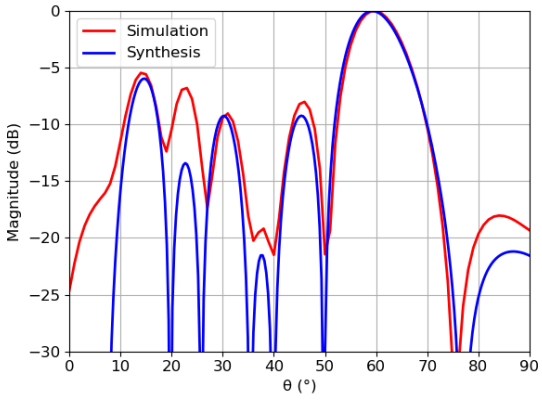

Fig. 6. Far-field - Angle of incident wave: 45°.

Furthermore, the angular stability of the design is presented. Theoretically, the scattered field would be directed at an angle of 15° away from the incident angle which is simply the difference between the designed reflected and incident angles. Due to the discretisation and a different angle of the incidence of the surface there is a deviation from this theoretical expectation, however, the main lobe is still observed. For the incident angle of 65° the surface does not perform as might be expected by the synthesis which may expose a limit in the method. Fig. 7 presents a comparison between the analytical results and full-wave simulations.

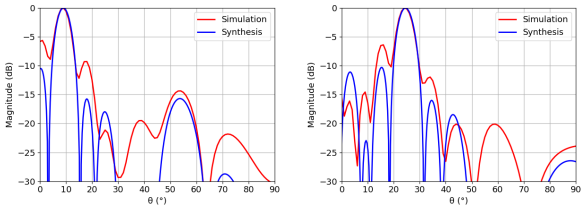

(a) Angle of incidence: 0°

(b) Angle of incidence: 15°

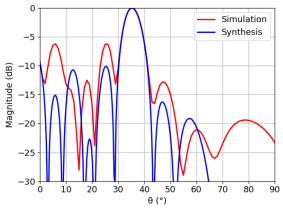

(c) Angle of incidence: 25°

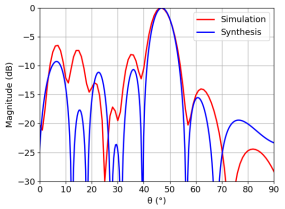

(d) Angle of incidence: 35°

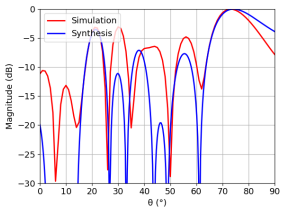

(e) Angle of incidence: 55°

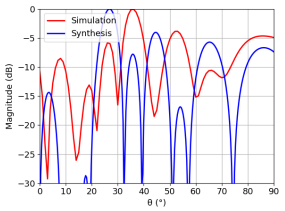

(f) Angle of incidence: 65°

Fig. 7. Far-field - Angular stability.

IV. METASURFACE MEASUREMENT

The designed metasurface was manufactured, measured and compared with full-wave simulations. It was made as a two-layer printed circuit board (PCB). The board was 0.8 mm thick and made of FR-4 material with dimensions of 282.6 mm (x) and 302.8 mm (y) (Fig. 8).

The measurement was performed in an anechoic chamber at The University of Sheffield using two horn antennas (Fig. 9) and a vector network analyser (HP 8720D). The distance between the antennas and the surface was 64.5 cm.

The far-field is the region where the radiation pattern either from an antenna or surface does not change its shape with distance and the vectors of electric and magnetic fields are orthogonal to each other and it can be calculated as:

$$R_{far} = \frac{2D^2}{\lambda}, \tag{1}$$

where D is geometric dimension of an antenna and λ is wavelength [7]. Based on the equation, far-field region of our horn antennas is 1.3 m and far-field region of the metasurface is 11.4 m far away. From this perspective our measurements are presented as indicative measurements as they were performed in the near-field region. From our experience this type of measurement usually provides a good indication of behaviour of a measured structure but it is worth noting that this systematic error exists in our measurements and cannot be easily removed.

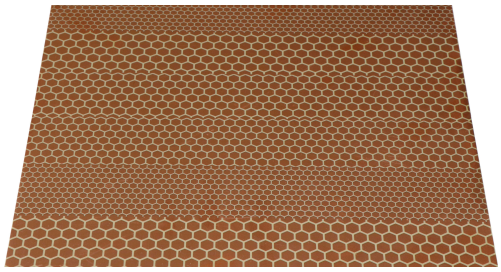

Fig. 8. Manufactured metasurface.

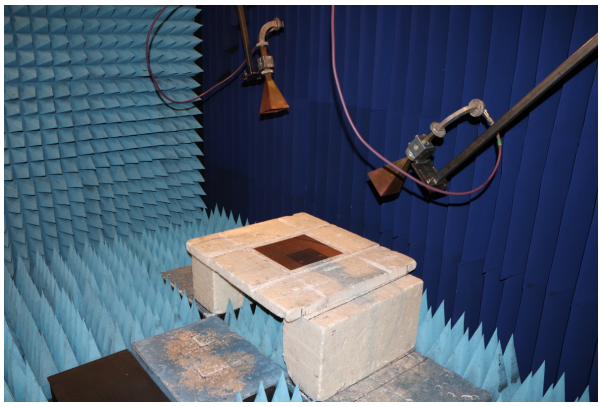

Fig. 9. Measurement.

Fig. 10 presents a comparison between a measurement and simulations. It can be seen that the main lobe is off by only a few degrees while the difference between the side lobes is greater (especially in terms of magnitude). Furthermore, the side lobes are also affected by the permittivity change. Results for the permittivity of 4.1 and 4.3 are presented for comparison as FR-4 is a composite material consisting of woven fibre-class cloth with an epoxy resin binder. Thus, the permittivity of this dielectric varies as every manufacturer makes different resin-to-fibreglass ratios.

As this structure is not symmetrical, the surface was also rotated by 180° and measured. Again, the angle of incidence

was 45°. In this case, the maximum of the reflected wavefront is at 33° as can be seen in the following figure (Fig. 11).

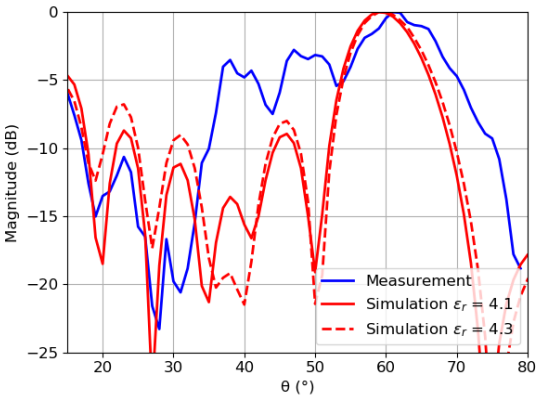

Fig. 10. Measurement versus simulation at 10 GHz.

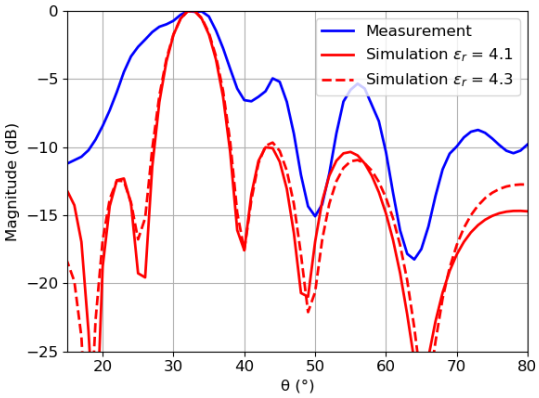

Fig. 11. Measurement versus simulation at 10 GHz (opposite direction).

V. Textile metasurface

As a step further to the metasurface presented above, the same design procedure was adopted for testing of a textile metasurface manufactured by an electroplating process (Fig. 12). The surface was designed for the angle of incidence of 45° and reflectance of 60°.

As the electroplating process requires a current flow, it would be impossible to connect each hexagonal patch to a power source. Therefore, the complexity and periodicity of the surface had to be reduced. The metasurface had to be modified in the way that the conductive patches were electrically connected between each other. In this case, the unit cells were designed as circular patches connected to its neighbours with a 2 mm wide strip placed orthogonally to the polarisation vector of the incident wave. (TM wave was considered.) 0.5 mm thick textile material of permittivity 1.3 and 5.2 mm thick foam of permittivity 1.05 above a perfect electric conductor (PEC) was considered in the simulation. The dimensions of the surface were 235 x 141 mm.

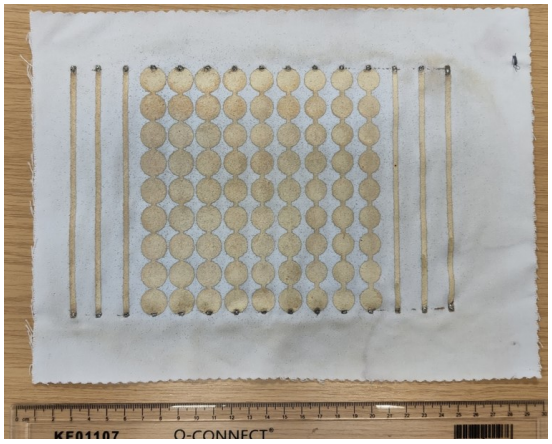

Fig. 12. Manufactured textile metasurface.

Unfortunately, several parameters had to be estimated before the final configuration was known. Therefore, when the simulations were performed with the correct parameters, the phase distribution (73°, -76°, -108° and -131°) of the manufactured metasurface did not follow the smooth phase distribution prescribed by Method 1 and Method 2 (Fig. 13).

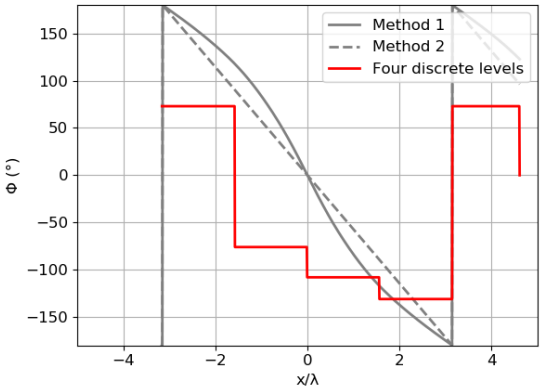

Fig. 13. Final phase distribution.

On the other hand, the results of the analytical approach were also in this case very accurate in comparison with the full-wave electromagnetic simulation and the main beam was close to 60° (56.5°) as can be seen in Fig. 14. This could lead to a conclusion that from the practical point of view, even relatively high phase distortions might not affect the main beam significantly but will affect mainly the side lobes. This behaviour could be advantageous in some cases where the reflector could be slightly detuned for instance due to weather conditions such as snow, rain, temperature changes etc.

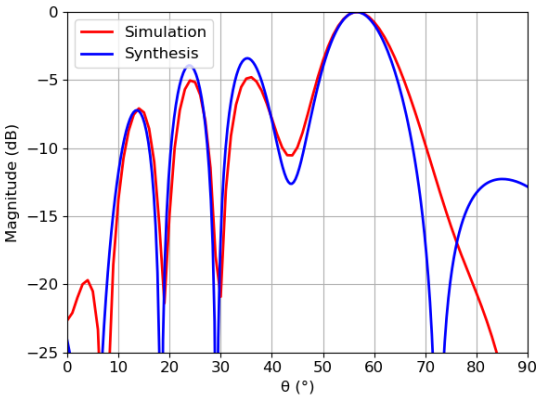

Fig. 14. Far-field - Angle of incident wave: 45°.

Fig. 15 compares the measured and simulated results. For the measurement, 5.2 mm thick foam was covered on one side with an aluminium foil tape. The textile surface was then placed on the top of this slab.

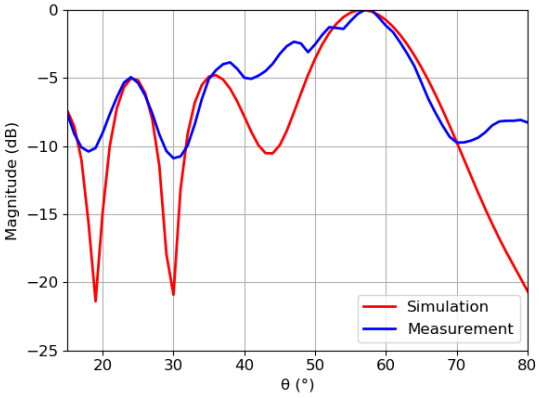

Fig. 15. Measurement versus simulation at 10 GHz.

It is worth noting that the main beam of a solid conductive plate of the same dimensions is about 4 dB higher (at the angle of 45°) in comparison with the main beam of this metasurface.

VI. Conclusion

In this paper, we presented that the analytical approach can be used for designing of the metasurfaces. It was found that small phase adjustments do not affect the main lobe (there are only negligible differences), on the other hand, they have a great impact on the side lobes. It is worth noticing that neither mutual coupling nor the scattering from edges of the surface is considered in the analytical techniques, but they are taken into account in the full-wave simulations.

The design procedure was adopted for testing of a textile metasurface manufactured by an electroplating process. In comparison with the standard printing technique, the copper electroplating has lower accuracy, lower conductivity of the coating conductor and requires an electrical connection of the design at the cathode end, so the design has to be optimised for it. On the other hand, it offers an alternative for applications where the standard printed technique is not practical.

The designed surfaces were used for comparison of the analytical approach with full-wave simulations and measurements. No optimisation was performed, so the performance and efficiency of the reflectors can still be improved. If minimising the side lobes is the goal, based on the presented results, the phase discretisation has to be as fine as possible. The side lobes are determined by Fourier transform of the rectangular window (given by the surface currents). Further improvement can be done by reducing the sharp discontinuity of surface currents at the edges of the surface by implementing the windowing functions (Chebyshev, Hannig, etc.) known from low side-lobe level array antennas. Unfortunately, this will lead to rather complex structures.

Acknowledgment

The textile metasurface was manufactured by Pireta.

References

[1] K. Achouri, M. A. Salem, and C. Caloz, "General metasurface synthesis based on susceptibility tensors," *IEEE Transactions on Antennas and Propagation*, vol. 63, no. 7, pp. 2977–2991, July 2015.

[2] K. L. Ford and K. Shah, "A study on the use of metasurface synthesis using electric and magnetic susceptibility," in *2016 Loughborough Antennas Propagation Conference (LAPC)*, Nov 2016, pp. 1–4.

[3] B. H. Fong, J. S. Colburn, J. J. Ottusch, J. L. Visher, and D. F. Sievenpiper, "Scalar and tensor holographic artificial impedance surfaces," *IEEE Transactions on Antennas and Propagation*, vol. 58, no. 10, pp. 3212–3221, Oct 2010.

[4] D. Sievenpiper, J. Colburn, B. Fong, J. Ottusch, and J. Visher, "Holographic artificial impedance surfaces for conformal antennas," in *2005 IEEE Antennas and Propagation Society International Symposium*, vol. 1B, 2005, pp. 256–259 vol. 1B.

[5] S. Ebadi, T. Driscoll, and D. Smith, "Visual illustrations of microwave holographic beamforming using a modulated surface-impedance metamaterial," in *2013 IEEE Antennas and Propagation Society International Symposium (APSURSI)*, July 2013, pp. 2343–2344.

[6] M. Cerveny, K. L. Ford, and A. Tennant, "Metasurface synthesis using susceptibility tensors and holographic technique," in *Loughborough Antennas Propagation Conference (LAPC 2017)*, Nov 2017, pp. 1–4.

[7] C. A. Balanis, *Antenna Theory*. Hoboken, New Jersey: John Wiley and Sons, 2005.

[8] J. A. Gordon, C. L. Holloway, and A. Dienstfrey, "A physical explanation of angle-independent reflection and transmission properties of metafilms/metasurfaces," *IEEE Antennas and Wireless Propagation Letters*, vol. 8, pp. 1127–1130, 2009.

[9] E. F. Kuester, M. A. Mohamed, M. Piket-May, and C. L. Holloway, "Averaged transition conditions for electromagnetic fields at a metafilm," *IEEE Transactions on Antennas and Propagation*, vol. 51, no. 10, pp. 2641–2651, Oct 2003.

Reflective Switchable Polarisation Rotator Based on Metasurface with PIN Diodes

Michal Cerveny, Kenneth Lee Ford, Alan Tennant

***Abstract*—A planar metasurface that rotates the polarisation of reflected signals by 90° is presented in this article. The surface also permits the relative phase of the rotated, reflected signal to be controlled. The metasurface rotator uses a square printed patch element mounted above a conducting ground plane. The addition of PIN diode controlled VIAs (Vertical Interconnect Access) at the corners of each square patch provide the ability to modify the scattering properties of the surface. In particular, the surface can be programmed to shift the phase of the rotated waveform by +/-90°. The polarisation rotator was manufactured, measured and compared against numerical simulations and the maximum measured bandwidth was 25% (4.8-6.2 GHz) for co-polarised attenuation of 10 dB. The proposed surface can be adopted for practical applications such as circularly polarised antennas.**

***Index Terms*—Polarisation rotator, Metasurface, Polarisation conversion**

I. Introduction

POLARISATION rotators have been investigated intensively for decades and there are many principles and geometries developed for polarisation conversion. One of the most common device based on polarisation rotation and used in daily life are liquid-crystal displays (LCD) [1], [2]. Even though the physical principles are the same for both optical and microwave spectrum [3]–[5], the practical challenges differ. Polarisation rotators can be further divided into two main categories: transmissive [6] and reflective [7]. This paper deals with a reflective switchable polarisation rotator designed for microwave frequencies. One of the most popular reflective polarisation rotator is based on split rings that have several modifications such as double split ring resonator for broadband characteristic [8], [9]. Moreover, triangular split ring resonator [10], L-shaped rotator [11] or substrate integrated waveguide cavity resonator [12] have been studied. Another group of polarisation rotators is based on metasurfaces utilising VIAs that connect a patch with ground plane [13]–[18]. All structures have one common similarity which is the type of symmetry. The structures are usually symmetric at the angle of 45°, so the surface can interact with linearly polarised waves oriented vertically or horizontally.

Also published are several active polarisation rotators based on tunable metasurface with varactor diodes [15] or with PIN diodes that allow switching the polarisation conversion on and off [19], [20].

In this paper, a reflective microwave metasurface that is capable of rotating the polarisation and also changing the reflected phase between two states was designed. In particular the phase difference between those two states of the reflected electromagnetic wave is 180°. Even though the proposed polarisation rotator uses a similar geometry as the one presented in [19], the functionality is different. The mentioned metasurface is capable of switching the polarisation rotation on and off but it does not have any capability to control/modulate the phase of rotated polarisation and the incident field must be oriented at the angle of 45°. Furthermore, the surface is capable to change the phase of co-polar reflection (unrotated polarisation) by 180° for x-polarised incident wave at a single frequency. That feature is useful especially when each unit cell can be addressed independently for adaptive beamstearing.

In contrast, the proposed metasurface is capable of switching the polarisation rotation on and off but at the same time the phase of the rotated polarisation can be controlled. The 180° phase difference is obtained not only at a single frequency but across the usable band. Finally, the incident field can be both vertically and horizontally polarised. The disadvantage of the proposed metasurface is that each unit cell cannot be independently addressed. This issue is discussed further in the article with possible solutions.

The functionality of a polarisation rotator in combination with the switchable phase change of 180° increases the practical usage greatly. For instance, it can be used for switchable circularly/linearly polarised antennas for satellite communication which allow the minimization of Faraday's effect and increase of polarisation diversity at the same time. This leads to higher spectral efficiency and reduced signal leakage due to polarisation mismatch and thus there is higher link reliability [21], [22]. The promoted polarisation rotator can also be used as a polarisation modulator [23], [24]. Also, secure wireless communication systems [25], [26] could benefit from this design. Another application is beamforming [27]. Overall, the proposed metasurface offers an alternative for cases where both polarisation rotation and a phase control are required.

The electromagnetic simulations were performed using full-wave analysis in the frequency domain considering unit cell boundary conditions in CST Microwave Studio. The results were validated by manufacturing and measuring both passive and active polarisation rotators.

The paper is structured as follows. Section II summarises the theory and presents the used notation. Section III studies several geometries of a passive rotator and measured results of the manufactured metasurface are compared with the simulations. Section IV deals with our design of an active polarisation rotator based on the principles presented in Section III. Section V shows a possible use of the metasurface.

M. Cerveny, K. L. Ford and A. Tennant were with the Department of Electronic and Electrical Engineering, The University of Sheffield, Sheffield, UK, e-mail: m.cerveny@sheffield.ac.uk.

II. Theory

In general, the reflection coefficient is defined as a ratio between the scattered field E^s and incident field E^i:

$$r = \frac{E^s}{E^i} \tag{1}$$

For simplicity, the electric field is considered as a plane wave propagating in z direction:

$$E = \hat{u}^{pol} E_0 e^{-j(kz-\omega t)} \tag{2}$$

where $\hat{u}^{pol}$ is the polarisation direction, E_0 is the magnitude of electric field, k is the wave number ($2\pi/\lambda$) and ω is the angular frequency ($2\pi f$). Electric field E can be decomposed into two orthogonal polarisations and the scattering matrix S is defined as:

$$\begin{bmatrix} E_x^s \\ E_y^s \end{bmatrix} = \begin{bmatrix} S_{xx} & S_{xy} \\ S_{yx} & S_{yy} \end{bmatrix} \begin{bmatrix} E_x^i \\ E_y^i \end{bmatrix} \tag{3}$$

In this case the electric field is oriented along the x- and y-axes. The components S_{xx} and S_{yy} are called co-polarised reflection coefficients and similarly, S_{yx} and S_{xy} are cross-polarised reflection coefficients. The co-polarised reflection coefficients are defined as:

$$r_{xx} = \frac{E_x^s}{E_x^i} \qquad r_{yy} = \frac{E_y^s}{E_y^i} \tag{4}$$

and the cross-polarised reflection coefficients are defined as:

$$r_{yx} = \frac{E_y^s}{E_x^i} \qquad r_{xy} = \frac{E_x^s}{E_y^i} \tag{5}$$

where E_x^i, E_y^i is the incident x-polarised, y-polarised electric field, respectively, and E_x^s, E_y^s is the scattered x-polarised, y-polarised electric field [28].

III. Study of passive polarisation rotator

A polarisation rotator based on VIA connecting a top patch with a ground plane [13] was studied and modified (Fig. 1). It was assumed that by changing the position of the VIA from one corner of the patch to the other one, the surface currents induced by the incoming electromagnetic wave would be forced to change their direction and thus the vector of the rotated electromagnetic field should have the same magnitude but the opposite sign (direction). Thus, the change of position of VIA should provide phase difference of 180° of the reflected wave.

State A and B in Fig. 1 define the position of the VIA (right or left) and simulate an ideal switch. The physical dimensions of the rectangular unit cell are as follows, the width w is 9.4 mm, thickness of the dielectric h (FR-4, $\epsilon_r = 4.3$) is 6.4 mm and the length of each side of the patch l is 5.4 mm. The diameter of VIA is 0.8 mm.

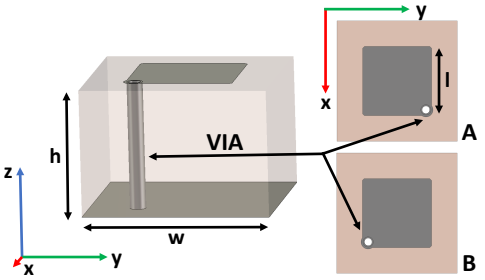

Fig. 1: Unit cell design of a passive rotator, state A: VIA is located on the right, state B: VIA is located on the left.

The diagonal symmetry allows the studied surface to be sufficient for both vertical and horizontal polarisation. As it is shown in Fig. 2, the passive rotator was tuned around the center frequency of 4.5 GHz where the cross-polarised reflection (red curve) and co-polarised reduction (blue curve) can be observed. Furthermore, state A and B does not have any effect on the magnitude of the reflection coefficient.

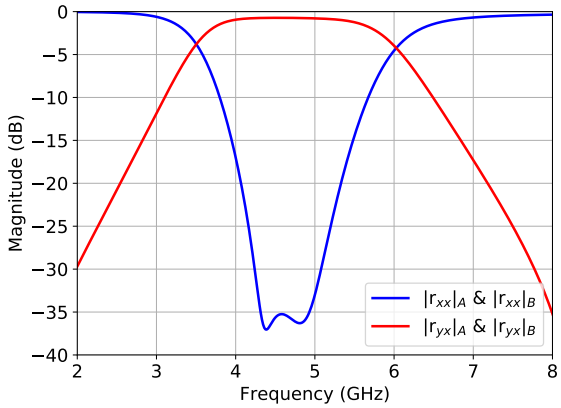

Fig. 2: Magnitude of the reflection coefficient for x-polarised wave at normal incidence (simulation).

A. Measurement

The measurement was performed in an anechoic chamber equipped with an NRL (Naval Research Laboratory) Arch which is a free-space measurement system for testing the reflectivity of materials. As shown in Fig. 3, it is equipped with two single polarised horn antennas oriented towards the metasurface. Furthermore, the antennas can be rotated by 90° which allows both co-polarised and cross-polarised measurements. For normal incidence, this configuration does not allow the pure monostatic measurement due to the width of the antennas. Therefore, the antennas are located close to each other to keep the bistatic angle as low as possible [28]. The physical separation between the horn antennas was approximately 1 cm. The antennas were connected by coaxial cables to Hewlett Packard 8720D network analyzer placed outside the chamber.

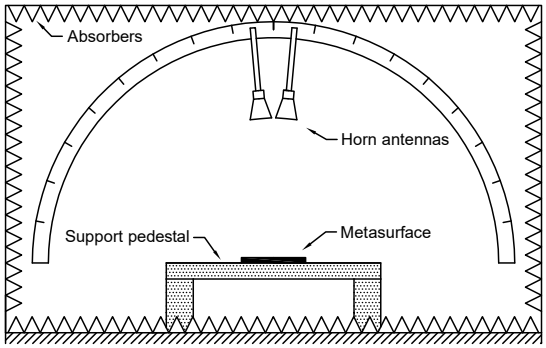

Fig. 3: NRL Arch - measurement setup.

For co-polarised measurement the bottom layer (flat plate) of the metasurface was used for calibration, so the reference plane was established at the front face of the metasurface. A long thin rod rotated by 45° in xy plane was used as a reference for the cross-polarised measurement. In the calibration procedure the empty chamber (isolation) was also taken into account. Furthermore, time gating was used for reduction of antenna coupling and residual reflections in the anechoic chamber.

Fig. 4 shows the manufactured metasurface. Dimensions of the PCB (Printed Circuit Board) were 404 x 404 mm and it consisted of 1849 unit cells, which were periodically placed in 43 columns and 43 rows. Top patches were connected with the bottom ground plane with VIAs. The diameter of VIAs (0.8 mm) was chosen based on our PCB manufacturer and its technical requirements.

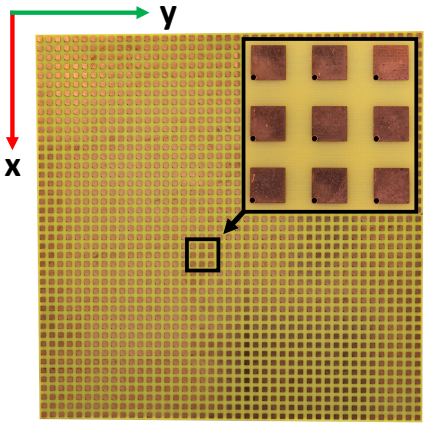

Fig. 4: Manufactured passive polarisation rotator.

The results are shown in Fig. 5. Subscripts A and B indicate the position of VIAs (right or left) for both measurement and simulation. (The surface had to be physically rotated by 90° to get from state A to state B.) It can be seen that the measurements of $|r_{xx}|_A$ and $|r_{xx}|_B$ differ even though the results should ideally be the same (as presented in the simulated results). The differences between the simulations and measurements can be caused by a few factors and most likely by their combination such as slightly curved surface, inhomogeneous substrate (FR-4), different permittivity of the substrate than it was considered in the simulation, non-constant thickness of the manufactured PCB and measurement error caused by physical rotation of the metasurface and due to the small bistatic angle of the horn antennas. On the other hand, this metasurface was made to prove the concept for our new design, so the small differences between our simulations and measurements were not an issue.

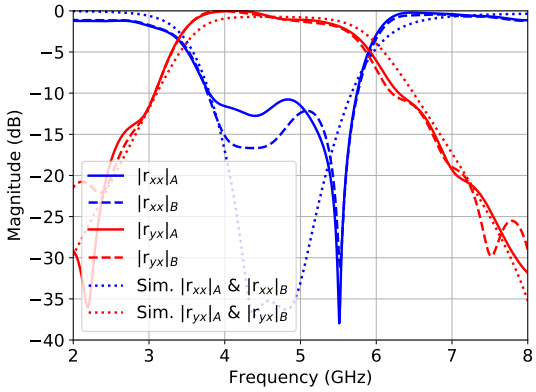

Fig. 5: Measured magnitude of the reflection coefficient for x-polarised wave at normal incidence for both state A and B. The simulated results are presented for comparison.

Fig. 6 shows the simulated and measured relative phase difference $\Delta\varphi$ between $r_{yx,A}$ and $r_{yx,B}$. The phase error of the measured surface was between 4° and 6° in the usable band in comparison to our results from simulation. In most of the practical applications the small phase error has a negligible effect on the performance.

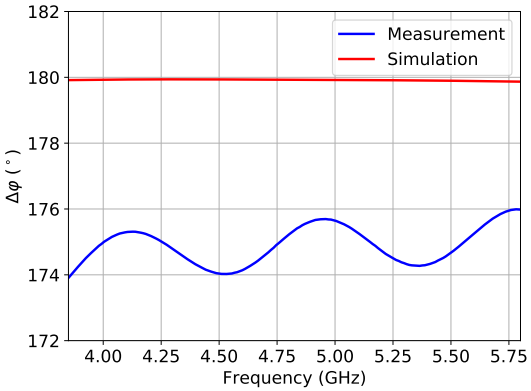

Fig. 6: Measured and simulated phase difference of the reflection coefficient between state A ($r_{yx,A}$) and B ($r_{yx,B}$).

The measured results proved that the rotated electromagnetic field is reflected in anti-phase when the state is changed from A to B and vice versa. This principle is further used for the design of a switchable metasurface.

B. Geometry of the polarisation rotator

This section deals with the shape of the top patch in terms of the overall performance of the rotator. As can be seen in Fig. 7 four different shapes were compared.

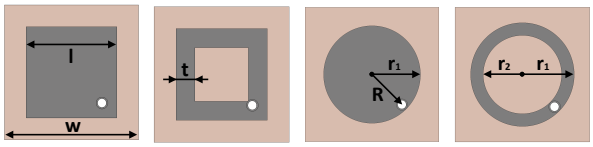

(a) Rotator 1 (b) Rotator 2 (c) Rotator 3 (d) Rotator 4

Fig. 7: Study of four geometries of the top patches and their effect on the performance of polarisation rotation.

The physical dimensions (unit cell) of the studied rotators were as follows, the width (w) was 9.1 mm and thickness of the grounded dielectric was 5.5 mm. The length (l) of each side of the square patch (Fig. 7a) was 6.1 mm and the thickness (t) of the square loop (Fig. 7b) was 1.3 mm. The radius (r_1) of the circular patch (Fig. 7c) was 3.5 mm and the inner radius (r_2) of the circular loop (Fig. 7d) was 2.65 mm. Position of the connection with ground plane can be seen as the white dots which were placed 3 mm away from the centre (R). The diameter of VIA was the same for all four unit cells (0.8 mm).

The polarisation rotator takes advantage of multiple resonances, which can be carefully tuned. Every resonance has limited bandwidth given by the Q-factor of the structure. Therefore, the overall usable bandwidth is determined by the requirements on the conversion ratio. The greater the conversion ratio is required, the narrower bandwidth can be expected. In this case three resonances were tuned close to each other to get one compact band with a high attenuation of the co-polarised reflection rather than having several single frequencies. Tuning can be performed by changing the physical dimensions of the unit cell and the position of VIA. The results from the simulations are presented in Fig. 8.

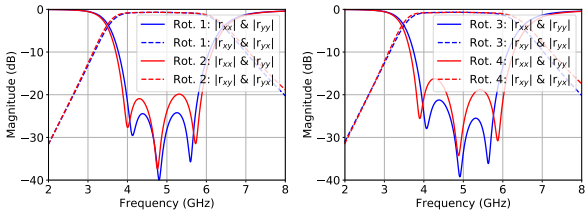

(a) Rotator 1 and 2 (b) Rotator 3 and 4

Fig. 8: Simulation of magnitude of the reflection coefficient at normal incidence for all four geometries of the top patches.

It can be seen that if the patch (rectangular or circular) is modified to a loop, the rotator with loop is slightly more broadband but the co-polarised attenuation is decreased approximately by 5 dB.

Based on these simulations we concluded that the shape of the top patch is not critical in terms of the response of the rotator and that the main functionality is provided by the position of VIA which creates an asymmetry allowing polarisation rotation.

C. Resonant modes of passive polarisation rotator

For better understanding of the converting mechanism, Fig. 9 shows the averaged surface currents for three resonant frequencies of Rotator 1. The rotator worked as a resonation circuit that was energized by $y(x)$-polarised incident field. An electric field oriented in z direction was created between the top patch and ground. Its averaged intensity correlated with the presented time-averaged current distributions. VIA placed in the corner of the patch created different potentials between neighbouring patches in the $x(y)$ direction. This effect can be seen in Fig. 10 where the surface was illuminated by y-polarised plane wave while the x component of the electric field appears between the top patches. This mechanism allowed to re-radiate the incident fields into the opposite polarisation.

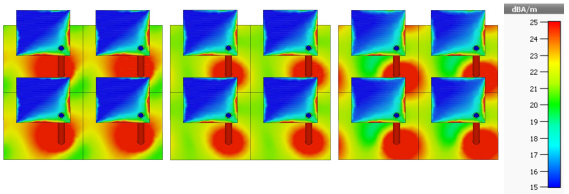

(a) 4.1 GHz (b) 4.8 GHz (c) 5.6 GHz (d) Scale

Fig. 9: Surface currents (averaged) presenting three resonant modes at frequency (a) 4.1 GHz, (b) 4.8 GHz and (c) 5.6 GHz. The scale is presented in (d).

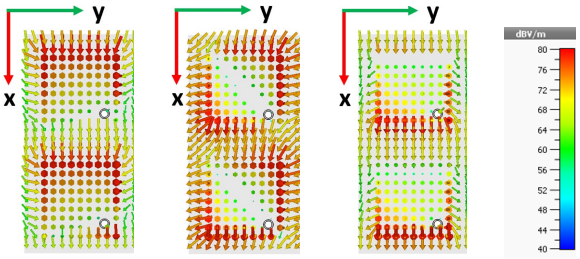

(a) 4.1 GHz (b) 4.8 GHz (c) 5.6 GHz (d) Scale

Fig. 10: E-filed plot presenting three resonant modes at frequency (a) 4.1 GHz, (b) 4.8 GHz and (c) 5.6 GHz. The scale is presented in (d).

D. Angular sensitivity and parametric study

This section presents the co-polarised and cross-polarised reflection coefficients for the angle of incidence Θ from 20° to 60° (Fig. 11) for both transverse electric (TE) and transverse magnetic (TM) polarised plane waves. The plane of incidence corresponds to zy plane. As the angle of incidence Θ increases, a small shift towards the higher frequencies can be observed as well as reduction of the conversion ratio (Fig. 12).

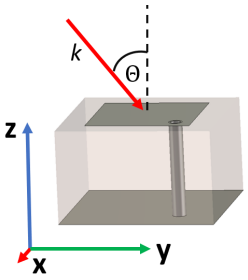

Fig. 11: Illustration of the incident angle Θ, k is the propagation vector and the plane of incidence corresponds to zy plane.

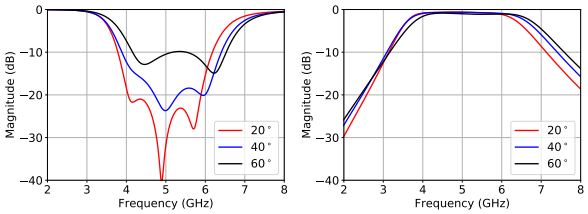

(a) TE co-polarisation (b) TE cross-polarisation

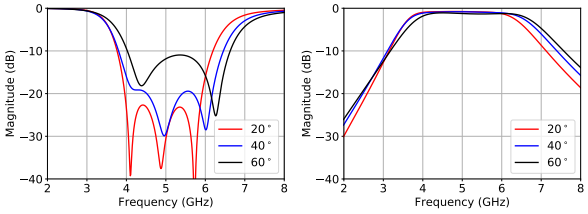

(c) TM co-polarisation (d) TM cross-polarisation

Fig. 12: Magnitude of reflection coefficients of Rotator 1 for the angle of incidence Θ from 20° to 60°.

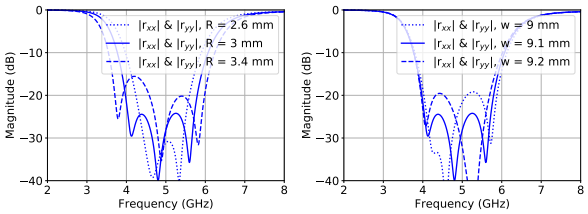

(a) Position of VIA (b) Width of unit cell

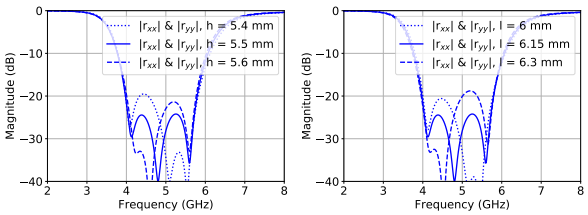

(c) Height of unit cell (d) Length of patch

Fig. 13: Magnitude of co-polarised reflection coefficients of Rotator 1, simulated results for different parameter values.

Furthermore, to see how the geometrical dimensions of the structure affect the resonant frequencies, a parametric study was performed.

Fig. 13a presents a parametric study for three distances (R) of VIA from the centre of the patch. It can be seen that with this parameter the overall bandwidth can be controlled. Moreover, the effect of adjusting the height (h), width of the unit cell (w) or length of the square patch (l) individually is presented in Fig. 13b-13d. In this case only co-polarised reflection coefficients are presented where the differences are more noticeable.

IV. Active Polarisation Rotator

Following the passive rotator, the analysis was extended to the reconfigurable case, which provides a number of practical challenges and is presented in this section.

A. Design and Simulations

Design of the active surface is based on the passive structure presented in the previous section. The aim was to modify the surface in such a way that the surface is capable of electrical rotation by 90° around its z-axis. This leads to the phase difference of the reflected wave of 180°.

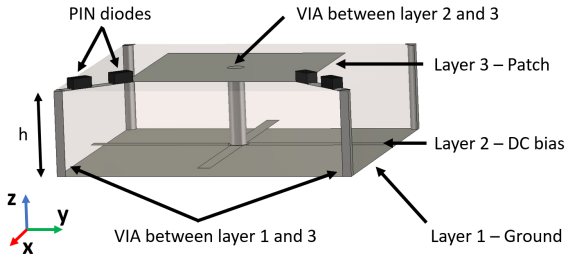

Fig. 14: Unit cell design of the switchable polarisation rotator. PIN diodes were simulated as RLC lumped elements and the black blocks (PIN diodes) were added for illustration purposes.

The metasurface was designed as a 3-layer PCB (Fig. 14) with the overall thickness h of the PCB 4 mm. The thickness between the bottom layer (Layer 1) and the middle one (Layer 2) was 0.4 mm and between the middle layer (Layer 2) and the top layer (Layer 3) was 3.6 mm. The blind VIA in the center of the unit cell worked as a DC bias and connected the top patch with Layer 2. Diameter of all VIAs was 0.8 mm.

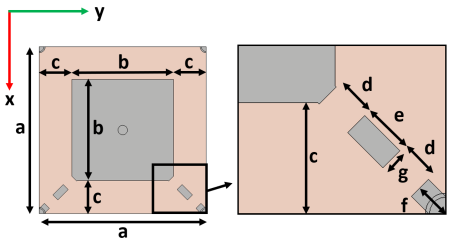

Fig. 15: Dimensions of the switchable polarisation rotator (top view).

Dimensions of the unit cell (Fig. 15) are shown in Tab. I. The top patch was placed to the centre of the unit cell and FR-4 substrate was considered for our design.

TABLE I: Dimensions of the switchable polarisation rotator.

Symbol	Dimension (mm)	Symbol	Dimension (mm)
a	14	b	8.5
c	2.75	d	1
e	1.24	f	0.9
g	0.6	h	4

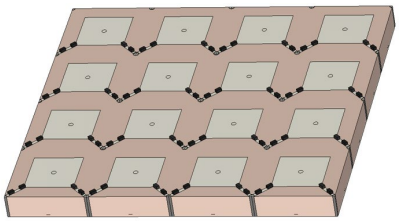

Fig. 16: Illustration of the metasurface containing 16 unit cells.

As can be seen the VIAs connected with ground (Layer 1) were moved into the corners of the unit cell. This allowed to share one VIA between two unit cells (Fig. 16) while only one patch was electrically connected to one VIA at a time. This solution simplified the design rapidly as each connection to the ground plane changed the field distribution on the metasurface.

PIN diodes were chosen for switching the structure as they are capable to provide large impedance changes at the frequencies of interest. Unfortunately, in comparison with an ideal switch they contain parasitic inductances, capacitances and resistances. This leads to finite isolation in OFF state and insertion losses in ON state. The PIN diodes were simulated as RLC lumped elements (Fig. 17). For ON state inductance L 0.6 nH and resistance R 2.1 Ω was considered. For OFF state inductance L 0.6 nH and capacitance C 0.17 pF was considered based on datasheet for PIN diode BAR64-02V.

(a) ON state (b) OFF state

Fig. 17: RLC equivalent circuits of PIN diode used in the simulations for ON and OFF state.

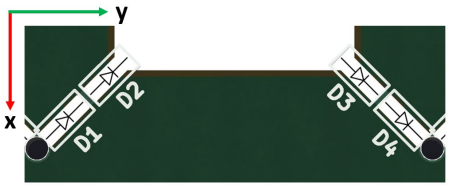

Fig. 18: Polarity of PIN diodes on the metasurface.

The electrical connection can be seen in Fig. 18. The diodes are connected with the central patch and with the ground plane through VIA located either on the right (state A) or on the left (state B). This design ensures that when diodes D1 and D2 are in ON state, diodes D3 and D4 are closed by a reverse voltage. It helps to obtain the correct functionality of the RF (Radio Frequency) switch as there is no floating voltage. Furthermore, because of the limited attenuation of PIN diodes in OFF state, two diodes were used in series, so the parasitic capacitance is halved. Hence the impedance of diodes D3 and D4 increases and so the isolation.

The simulated results are presented in Fig. 19a. It can be seen that the behaviour of the structure is slightly different for x- and y-polarised electromagnetic waves. The reason is that this structure unlike the passive one is not equal along x- and y-axis. It has a negligible effect on the rotated polarisation (cross-polarisation). Furthermore, the phase change of 180° was obtained across the entire usable band as shown in Fig. 19b.

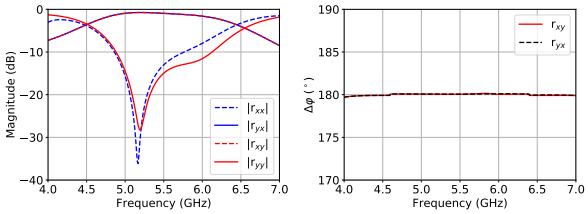

(a) (b)

Fig. 19: Simulated results: (a) Magnitude of the reflection coefficient at normal incidence. (b) Phase difference of the reflection coefficient between state A and B for both x- and y-polarised incident waves.

Fig. 20a shows the co-polarisation reflection coefficients for three values of parasitic capacitance of PIN diode. It can be seen that small difference of capacitance (0.2 pF) can change the resonation frequency of the polarisation rotator significantly. Fig. 20b presents the reflection coefficients when only one diode instead of two was used. When a design with only single diode was required, a single diode with a lower parasitic capacitance would need to be used. Typically, the smaller the parasitic capacitance of a PIN diode, the smaller the diode package, which can be difficult to solder without special tools.

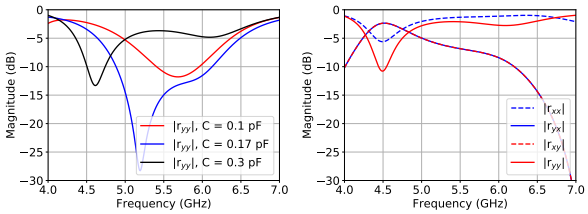

(a) (b)

Fig. 20: Simulated results: (a) Reflection coefficients $|r_{yy}|$ versus capacitance C used in the equivalent circuit. (b) Model with one diode considering capacitance of 0.17 pF.

Furthermore, a parametric study is presented in the following figures (Fig. 21a-21c) for $|r_{yy}|$. Reflection coefficients $|r_{xx}|$ work in the same way and therefore are not included. Practically, the design was limited by the dimensions of diodes. For example, the unit cell of width 13 mm would be preferable in terms of performance (Fig. 21b), but this unit cell would be too small for population of the diodes. For that reason a compromise had to be reached.

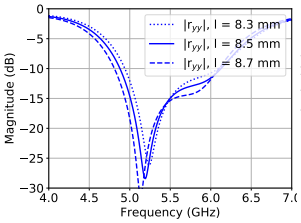

(a) Length of patch

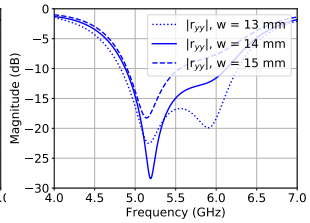

(b) Width of unit cell

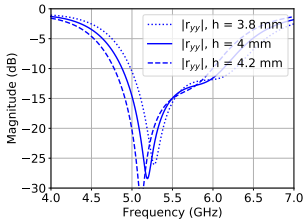

(c) Height of unit cell

Fig. 21: Simulated results for different parameter values of the switchable polarisation rotator.

B. Measurement

The proposed active polarisation rotator was manufactured (Fig. 22). It consisted of 121 unit cells located periodically in 11 rows and columns. The dimensions of the board were 16 x 16 cm.

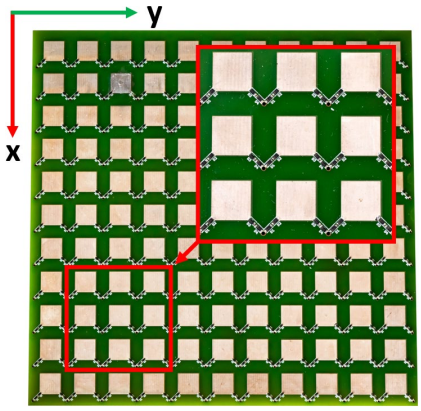

Fig. 22: Manufactured active polarisation rotator using three layer PCB and populated by PIN diodes (four PIN diodes per one unit cell).

It was measured for both x- (Fig. 23) and y-polarised (Fig. 24) incident fields. The magnitude of the reflection coefficients differs when the metasurface is switched from one state to the other. Ideally, the magnitude of the reflection coefficients should be the same for both polarities of the DC voltage. Practically, the difference can be observed especially in the co-polarised reflection. This effect is probably given by different resistance of the circuit as the current paths are different for each state. To compensate this effect, current levels would need to be set individually for state A and B. The metasurface can be switched from one state to the other with a very low current. The presented results are measured with total board current of 50 mA. The differences between the simulations and measurements could be introduced by manufacturing tolerances, measurement error and the simulation error caused especially by the simplified description of PIN diodes using an RLC equivalent circuit.

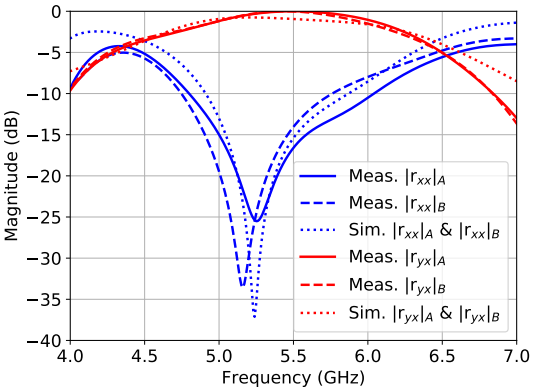

Fig. 23: Measured magnitude of the reflection coefficient for x-polarised wave at normal incidence for both state A and B. The simulated results are presented for comparison.

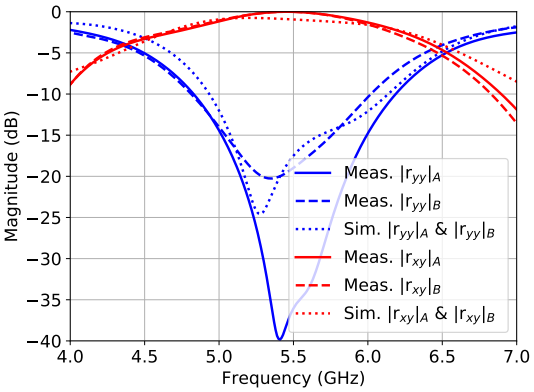

Fig. 24: Measured magnitude of the reflection coefficient for y-polarised wave at normal incidence for both state A and B. The simulated results are presented for comparison.

Fig. 25 shows the phase difference between state A and B for both x and y polarisations. The maximum phase error of the measured results was less than 5° for r_{xy} and 4° for r_{yx} in the frequency range from 4.5 GHz to 6.5 GHz in comparison to our simulation. This validated the simulated results and the

correct functionality of the designed switchable polarisation rotator.

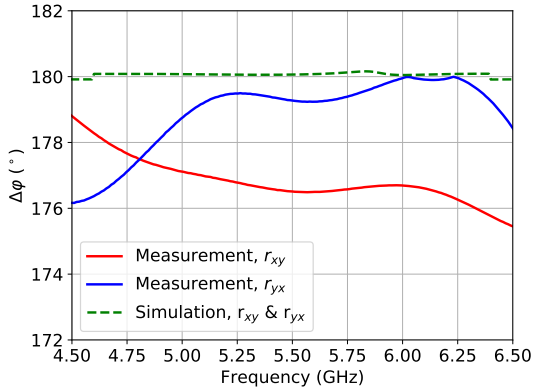

Fig. 25: Measured and simulated phase difference of the reflection coefficient between state A and B for both x- and y-polarised incident waves.

V. Switchable Polarisation Rotator Usage for Practical Applications

The presented metasurface can be further customised. In the previous section all the unit cells were connected together, so the entire metasurface could be changed from state A to state B just by changing the DC polarity and only two wires were needed for controlling the entire metasurface. This design can be easily modified for adaptive beamforming, so each line or row can be controlled independently based on the requirements (Fig. 26).

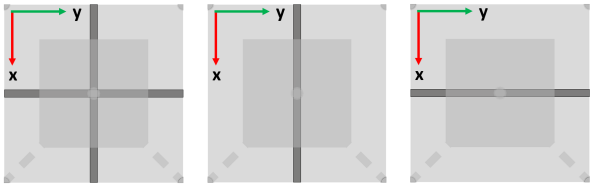

(a) XY (b) X (c) Y

Fig. 26: Possible configurations (XY, X, Y) of DC bias at the second layer.

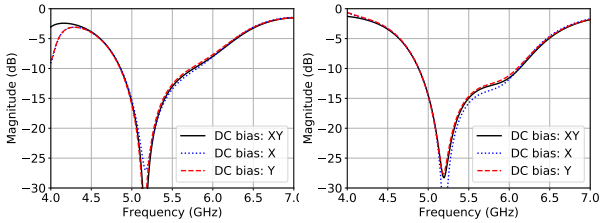

(a) $|r_{xx}|$ (b) $|r_{yy}|$

Fig. 27: Simulated magnitude (co-polarisation) of the reflection coefficient for three possible configurations (XY, X, Y) of the DC bias.

The DC bias placed in the metasurface has a negligible effect on the performance for both horizontally (y-axis) and vertically (x-axis) polarised incident fields (Fig. 27). The unit cells can further be grouped into clusters, so each cluster (super cell containing several unit cells) can be controlled independently.

A practical use of the proposed active metasurface can be an active antenna or modulator that can switch between right-hand/left-hand circular polarisation (RHCP/LHCP) as well as linear polarisation (LP). To obtain a circular polarisation, two components (vertical and horizontal) must exist with the phase difference of 90°. This can be achieved by placing a simple dipole antenna in front of the metasurface. As the rotator was designed for plane-wave interaction, the dipole of length 21 mm was placed 600 mm (12.2 λ at 6.1 GHz) in front of the metasurface to be in the far-field region. The change of RHCP/LHCP and LP radiation pattern can be done only by applying the respective DC voltage to the metasurface.

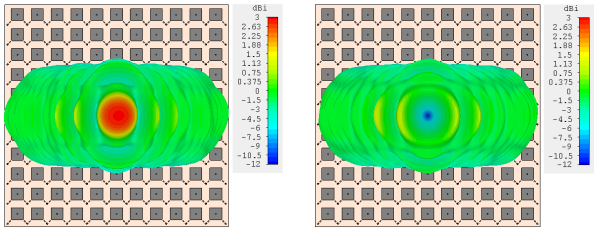

(a) RHCP (b) LHCP

Fig. 28: State A: (a) RHCP and (b) LHCP far-field radiation pattern at 6.1 GHz. The central top patch was connected with the VIA on the right side. RHCP main beam was produced.

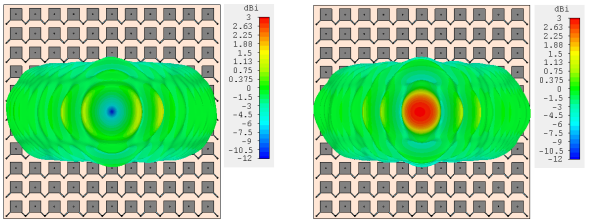

(a) RHCP (b) LHCP

Fig. 29: State B: (a) RHCP and (b) LHCP far-field radiation pattern at 6.1 GHz. The central top patch was connected with the VIA on the left side. LHCP main beam was produced.

Fig. 28 shows the radiation pattern for state A. It can be seen that this state produced RHCP polarisation while LHCP polarisation was highly attenuated. When the state is switched from state A to state B, LHCP polarisation was radiated into the required direction while RHCP is now attenuated (Fig. 29).

The ratio between the circular polarisations for each state is shown in Fig. 30. It can be seen that the highest ratio occurs in the direction of the main beam. This feature may be attractive

for secure wireless communications where the transmitted signal can be correctly decoded only in the direction of the main beam.

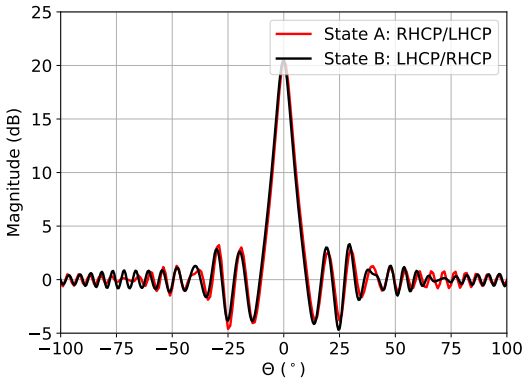

Fig. 30: Ratio RHCP/LHCP for state A and LHCP/RHCP for state B.

Furthermore, when no current is applied, the metasurface behaves as a regular reflector without any rotating functionality. This off state is presented in Fig. 31. As the dipole was vertically polarised in front of the metasurface, the whole antenna system with the metasurface produced only linear polarisation (vertical).

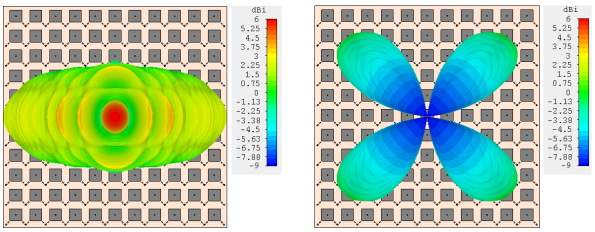

(a) Vertical polarisation (b) Horizontal polarisation

Fig. 31: Metasurface in off state illuminated by vertically-polarised wave (dipole antenna).

VI. Conclusion

In this article, a reflective switchable polarisation rotator based on an artificial magnetic conductor with offset VIA was presented. Following the study of electromagnetic properties and the effect of different topologies of a passive polarisation rotator, the analysis was extended to the reconfigurable case. The final design was capable of rotating the polarisation by 90° and switching the relative phase of the reflected electromagnetic wave by 180°. Furthermore, the surface allowed to behave as a regular conductive reflector in off state. The main advantage of our design is the fact that the phase of the rotated, reflected electromagnetic wave can be controlled. The relative phase difference of 180° was obtained not only at a single frequency but across the entire usable band for both vertically and horizontally polarised incident fields.

Based on our simulations and measurements, the surface worked in the frequency range of 4.8 and 6.2 GHz for co-polarised attenuation of 10 dB and the overall maximum measured phase error of the rotator was better than 4° in the usable bandwidth for both polarisations.

In combination with a simple dipole antenna, a switchable antenna with right hand circular polarisation, left hand circular polarisation and linear polarisation can be achieved. This can be advantageous for polarisation diversity as well as for design of a polarisation modulator.

The metasurface can be further customised for beamforming capability by splitting the metasurface into several independently controlled sections. Also, this surface could provide polarisation scrambling useful for secure wireless communication systems. Overall, the presented metasurface offers an alternative for cases where both polarisation rotation and a phase control are required.

References

[1] Xinyu Zhu, Zhibing Ge, T. X. Wu, and Shin-Tson Wu, "Transflective liquid crystal displays," *Journal of Display Technology*, vol. 1, no. 1, pp. 15–29, 2005.

[2] Hyungki Hong, "Dependency of spectral reflectance on rotating direction of liquid crystal for reflective liquid crystal displays," *Journal of Display Technology*, vol. 2, no. 3, pp. 233–236, 2006.

[3] A. Overvig, S. Shrestha, S. Malek, M. Lu, A. Stein, C. Zheng, and N. yu, "Dielectric metasurfaces for complete and independent control of the optical amplitude and phase," *Light: Science & Applications*, vol. 8, p. 92, 10 2019.

[4] S. Gao, C.-S. Park, S.-S. Lee, and D.-Y. Choi, "All-dielectric metasurfaces for simultaneously realizing polarization rotation and wavefront shaping of visible light," *Nanoscale*, vol. 11, pp. 4083–4090, 2019.

[5] X. Zhang, S. Yang, W. Yue, Q. Xu, C. Tian, X. Zhang, E. Plum, S. Zhang, J. Han, and W. Zhang, "Direct polarization measurement using a multiplexed pancharatnam–berry metahologram," *Optica*, vol. 6, pp. 1190–1198, Sep 2019.

[6] Z. Wu, Y. Ra'di, and A. Grbic, "Tunable metasurfaces: A polarization rotator design," *Phys. Rev. X*, vol. 9, p. 011036, Feb 2019.

[7] S. Yu, L. Li, G. Shi, C. Zhu, X. Zhou, and Y. Shi, "Design, fabrication, and measurement of reflective metasurface for orbital angular momentum vortex wave in radio frequency domain," *Applied Physics Letters*, vol. 108, no. 12, p. 121903, 2016.

[8] S. J. Li, X. Y. Cao, L. M. Xu, L. J. Zhou, H. H. Yang, J. F. Han, Z. Zhang, D. Zhang, X. Liu, C. Zhang, Y. J. Zheng, and Y. Zhao, "Ultra-broadband reflective metamaterial with rcs reduction based on polarization convertor, information entropy theory and genetic optimization algorithm," *Scientific Reports*, 2016.

[9] C. Hong-Ya, W. Jia-Fu, M. Hua, Q. Shao-Bo, Z. Jie-Qiu, X. Zhuo, and Z. An-Xue, "Broadband perfect polarization conversion metasurfaces," *Chinese Physics B*, vol. 24, no. 1, p. 014201, 2015.

[10] Q. Zheng, C. Guo, H. Li, and J. Ding, "Wideband and high efficiency reflective polarization rotator based on metasurface," *Journal of Electromagnetic Waves and Applications*, vol. 32, no. 3, pp. 265–273, 2018.

[11] Y. Jia, Y. Liu, W. Zhang, and S. Gong, "Ultra-wideband and high-efficiency polarization rotator based on metasurface," *Applied Physics Letters*, vol. 109, no. 5, p. 051901, 2016.

[12] X. C. Zhu, W. Hong, K. Wu, H. J. Tang, Z. C. Hao, J. X. Chen, and G. Q. Yang, "A novel reflective surface with polarization rotation characteristic," *IEEE Antennas and Wireless Propagation Letters*, vol. 12, pp. 968–971, 2013.

[13] D. Yan, Q. Gao, C. Wang, C. Zhu, and N. Yuan, "A novel polarization convert surface based on artificial magnetic conductor," in *2005 Asia-Pacific Microwave Conference Proceedings*, vol. 3, pp. 2 pp.–, Dec 2005.

[14] M. H. Ghazizadeh, G. Dadashzadeh, and M. Korshidi, "A novel wideband electromagnetic band gap structure for circular polarization conversion," in *2012 15 International Symposium on Antenna Technology and Applied Electromagnetics*, pp. 1–4, June 2012.

[15] W. Yang, D. Chen, W. Che, and W. Feng, "Multi-functional antennas using polarization-rotation artificial magnetic conductor structures," in *2017 10th Global Symposium on Millimeter-Waves*, pp. 11–14, May 2017.

[16] W. Yang, K. W. Tam, W. W. Choi, W. Che, and H. T. Hui, "Novel polarization rotation technique based on an artificial magnetic conductor and its application in a low-profile circular polarization antenna," *IEEE Transactions on Antennas and Propagation*, vol. 62, pp. 6206–6216, Dec 2014.

[17] W. Yang, K. W. Tam, W. W. Choi, W. Che, and H. T. Hui, "Polarisation rotation reflective surface based on artificial magnetic conductor and its application," *Electronics Letters*, vol. 50, pp. 1500–1502, October 2014.

[18] W. Yang, W. Che, W. W. Choi, and K. W. Tam, "A low-profile circularly polarized dipole antenna using a novel polarization rotation artificial magnetic conductor," in *2014 44th European Microwave Conference*, pp. 374–377, Oct 2014.

[19] H. Yang, X. Cao, F. Yang, J. Gao, S. Xu, M. Li, X. Chen, Y. Zhao, Y. Zheng, and L. Sijia, "A programmable metasurface with dynamic polarization, scattering and focusing control," *Scientific Reports*, vol. 6, 10 2016.

[20] M. Saikia, S. Ghosh, and K. V. Srivastava, "Switchable reflective metamaterial polarisation rotator," *Electronics Letters*, vol. 52, no. 12, pp. 1030–1032, 2016.

[21] I. Gheorghisor, A. Dissanayake, J. Allnutt, and S. Yaghmour, "Prediction of faraday rotation impairments in c-band satellite links," in *IEEE Antennas and Propagation Society International Symposium. Transmitting Waves of Progress to the Next Millennium. 2000 Digest. Held in conjunction with: USNC/URSI National Radio Science Meeting (C*, vol. 2, pp. 554–557 vol.2, 2000.

[22] H. Yang, J. An, H. Jung, J. Kim, and J. T. S. Sumantyo, "Circular polarization implementation on synthetic aperture radar," in *2014 International Conference on Information and Communication Technology Convergence (ICTC)*, pp. 991–994, 2014.

[23] I. Toyoda, *Modulation in Electronics and Telecommunications*, ch. Polarization Modulation. 07 2019.

[24] S. Henthorn, K. L. Ford, and T. O'Farrell, "Frequency selective surface loaded antenna for direct antenna modulation," in *2017 11th European Conference on Antennas and Propagation (EUCAP)*, pp. 731–734, 2017.

[25] Z. Luo, H. Wang, and W. Lv, "Directional polarization modulation for secure transmission in dual-polarized satellite mimo systems," in *2016 8th International Conference on Wireless Communications Signal Processing (WCSP)*, pp. 1–5, 2016.

[26] X. Zhang, B. Zhang, and D. Guo, "Physical layer secure transmission based on fast dual polarization hopping in fixed satellite communication," *IEEE Access*, vol. 5, pp. 11782–11790, 2017.

[27] L. Di Palma, A. Clemente, L. Dussopt, R. Sauleau, P. Potier, and P. Pouliguen, "Radiation pattern synthesis for monopulse radar applications with a reconfigurable transmitarray antenna," *IEEE Transactions on Antennas and Propagation*, vol. 64, no. 9, pp. 4148–4154, 2016.

[28] E. K. . J. S. . M. Tuley, *Radar Cross Section*. SciTech Publishing, 2004.

[29] Z. Zhang, X. Cao, J. Gao, and S. Li, "Broadband metamaterial reflectors for polarization manipulation based on cross/ring resonators," *Radioengineering Journal*, pp. 436–441, 2016.

[30] B. Lin, B. Wang, W. Meng, X. Da, W. Li, Y. Fang, and Z. Zhu, "Dual-band high-efficiency polarization converter using an anisotropic metasurface," *Journal of Applied Physics*, vol. 119, no. 18, p. 183103, 2016.

[31] H. F. Ma, G. Z. Wang, G. S. Kong, and T. J. Cui, "Broadband circular and linear polarization conversions realized by thin birefringent reflective metasurfaces," *Opt. Mater. Express*, vol. 4, pp. 1717–1724, Aug 2014.

[32] H. Chen, J. Wang, H. Ma, S. Qu, Z. Xu, A. Zhang, M. Yan, and Y. Li, "Ultra-wideband polarization conversion metasurfaces based on multiple plasmon resonances," *Journal of Applied Physics*, vol. 115, no. 15, p. 154504, 2014.

[33] Y. Liu, K. Li, Y. Jia, Y. Hao, S. Gong, and Y. J. Guo, "Wideband rcs reduction of a slot array antenna using polarization conversion metasurfaces," *IEEE Transactions on Antennas and Propagation*, vol. 64, pp. 326–331, Jan 2016.

[34] J. Hao, Y. Yuan, L. Ran, T. Jiang, J. A. Kong, C. T. Chan, and L. Zhou, "Manipulating electromagnetic wave polarizations by anisotropic metamaterials," *Phys. Rev. Lett.*, vol. 99, p. 063908, Aug 2007.

[35] L. Zhang, P. Zhou, H. Lu, H. Chen, J. Xie, and L. Deng, "Ultra-thin reflective metamaterial polarization rotator based on multiple plasmon resonances," *IEEE Antennas and Wireless Propagation Letters*, vol. 14, pp. 1157–1160, 2015.

[36] Q. Zheng, C. Guo, H. Li, and J. Ding, "Broadband radar cross-section reduction using polarization conversion metasurface," *International Journal of Microwave and Wireless Technologies*, vol. 10, no. 2, p. 197–206, 2018.

[37] J. J. Yang, Y. Z. Cheng, C. C. Ge, and R. Z. Gong, "Broadband polarization conversion metasurface based on metal cut-wire structure for radar cross section reduction," *Materials*, 2018.

[38] M. Feng, J. Wang, H. Ma, W. Mo, H. Ye, and S. Qu, "Broadband polarization rotator based on multi-order plasmon resonances and high impedance surfaces," *Journal of Applied Physics*, vol. 114, no. 7, p. 074508, 2013.

[39] Y. Jia, Y. Liu, Y. J. Guo, K. Li, and S. X. Gong, "Broadband polarization rotation reflective surfaces and their applications to rcs reduction," *IEEE Transactions on Antennas and Propagation*, vol. 64, pp. 179–188, Jan 2016.

[40] P. J. Ferrer, J. M. Gonzalez-Arbesu, C. Craeye, and J. Romeu, "Transpolarizing surfaces and potential applications," in *2008 38th European Microwave Conference*, pp. 281–284, Oct 2008.

[41] S. Henthorn, K. L. Ford, and T. O'Farrell, "Bit-error-rate performance of quadrature modulation transmission using reconfigurable frequency selective surfaces," *IEEE Antennas and Wireless Propagation Letters*, vol. 16, pp. 2038–2041, 2017.

[42] K. L. Ford, J. Roberts, S. Zhou, G. Fong, and J. Rigelsford, "Reconfigurable frequency selective surface for use in secure electromagnetic buildings," *Electronics Letters*, vol. 49, pp. 861–863, July 2013.

[43] A. Tennant, W. Hurley, and T. Dias, "Knitted, textile, high impedance surface with integrated conducting vias," *Electronics Letters*, vol. 49, pp. 8 –10, January 2013.

[44] W. Xu and S. Sonkusale, "Microwave diode switchable metamaterial reflector/absorber," *Applied Physics Letters*, vol. 103, 07 2013.

Michal Cerveny Received his M.Sc. from the Czech Technical University (CTU) in Prague in 2014 and is currently working towards his Ph.D. focused on controlling the propagation of electromagnetic waves using artificial materials. In 2014, he started to work as a visiting researcher at the University of Sheffield working on wireless friendly energy efficient buildings. In 2015, he worked for The Rolls-Royce University Technology Centre doing RF modelling within marine environments and since 2016 he has been working at The University of Sheffield as a research associate in applied electromagnetics.

Alan Tennant Received the B.Eng. degree in electronic engineering and the Ph.D. degree in medical physics, both from the Univerisity of Sheffield, Sheffield, U.K., in 1985, and 1992, respectively. Between 1985 and 1986, he worked with BAE Systems, Stevenage, U.K. In 1992, he joined Defence and Evaluation Research Agency (DERA), Malvern, U.K., where he worked on phased-array antenna systems, before taking up an academic post at the University of Hull, Hull, U.K. He returned to the Department of Electronic and Electrical Engineering, University of Sheffield, in 2001, as a Senior Lecturer in the Communications and Radar Group where he is involved in research into adaptive materials for radar signature management, novel three-dimensional phased array antenna topologies, and acoustic array systems.

Kenneth Lee Ford (M'07–SM'10) received the B.Eng. and Ph.D. degrees in electronic engineering from the University of Sheffield, Sheffield, U.K. in 1998 and 2003, respectively. In 2001, he joined the Stealth Materials Department, Advanced Technology Centre, BAE Systems, Towcester, U.K. In 2005, he joined the University of Sheffield as a Lecturer of communications, and became a Senior Lecturer in 2012. His current research interests include reconfigurable antennas, miniaturized antennas, metamaterials, propagation in the built environment, and electromagnetic structures for biomedical applications.

GNSS Sector Antenna for Interference Mitigation and Localisation using a High Impedance Reflector

Michal Cerveny, Pavel Hazdra

***Abstract*—There are many applications where the reception of global navigation satellite system signals is crucial. In such cases, the capability to reduce the interference (both unintentional or hostile) is critical. The proposed sector antenna offers a stable radiation pattern with no beam steering across the frequency band and good impedance matching. It also benefits from a high impedance reflector, which allows the antenna to provide broadband operation and low-profile compact geometry. Furthermore, seven of these sector antennas were placed in a heptagonal shape and combined with a broadband crossed dipole. As a result, the designed antenna system can reduce vertically-polarised interference by approximately 45 dB in the required directions.**

***Index Terms*—Antenna, GNSS, Interference, Metasurface.**

I. Introduction

THESE days, requirements on antenna systems are more challenging due to many sources of interference present in the radio spectrum. GNSS (Global Navigation Satellite System) signals processed by receivers on Earth are very weak while interference from terrestrial sources can be much stronger. When this happens, the overloaded receiver is unable to receive weak GNSS signals. In such situations, a clever antenna system can help to keep the reception stable.

One technique used for interference mitigation is interference nulling based on phased antenna arrays. Several antenna systems have already been published [1]–[7] and many antenna designs deal with interference with each having its own pros and cons. For instance, uniform planar antenna arrays can be comfortable from a mathematical point of view, however, creating a null in the main lobe increases the side lobe levels and creates unwanted nulls in the radiation pattern [8], [9]. Furthermore, mutual coupling can be another problem in such configurations and may need to be compensated [10]. When other parameters such as impedance matching, axial ratio, stable radiation pattern along with dimensions of the antenna are considered, the design of such a system can be very complex. For important services relying on GNSS, several antenna systems should cooperate to increase diversity and maximum performance.

The proposed GNSS antenna system is a combination of a circularly-polarised antenna covering the sky and seven vertically-polarised sector antennas that cover the low angles above the Earth's surface where the source of interference is expected.

In the literature, many designs of vertically-polarised antennas can be found [11]–[14]. Unfortunately, there was no design that would fit the proposed configuration well in terms of broadband operation, low profile, radiation pattern and mutual coupling. Therefore, a new sector antenna, as well as the whole system has been designed.

Pavel Hazdra is with the Department of Electromagnetic Field, Faculty of Electrical Engineering, Czech Technical University in Prague, Technicka 2, 166 27, Prague, Czech Republic (e-mail: hazdrap@fel.cvut.cz).

Michal Cerveny is with the Department of Electromagnetic Field, Faculty of Electrical Engineering, Czech Technical University in Prague, Technicka 2, 166 27, Prague, Czech Republic and the Department of Electronic and Electrical Engineering, The University of Sheffield, Sheffield S1 4ET, UK.

This work has been supported by the Czech Science Foundation, project 20-02046S Antenna Arrays with Quantized Controlling.

II. Design of the Sector Antenna

The proposed sector antenna consists of a reflector with a metasurface (high-impedance surface) [15], side walls, and an antenna board as shown in Fig. 1. Due to the metasurface implementation, the antenna provides both low-profile geometry (0.15 - 0.2 λ) and broadband operation [16], [17].

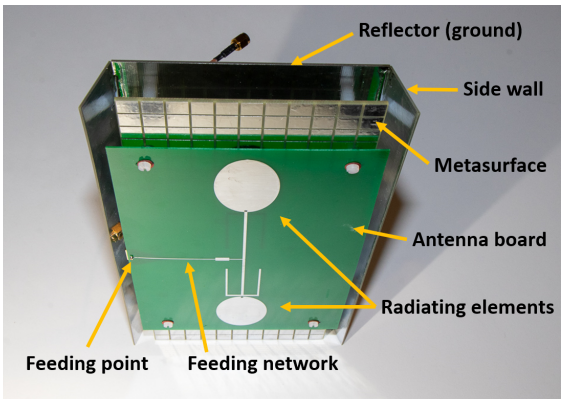

Fig. 1: Sector antenna.

The design of the top antenna board consists of a feeding network and two radiating elements and can be seen in greater detail in Fig. 2. The feeding network contains several impedance transformations, as well as a conversion from an asymmetrical to symmetrical line.

The 50 Ω coaxial cable is connected to a quarter-wavelength microstrip of impedance 70.7 Ω which transforms the 50 Ω input to 100 Ω output [18], [19], and transforms the asymmetrical feeding to a symmetrical line (double-sided parallel strip) via the tapered shape [20] of the ground. All following lines are designed as double-sided parallel strips. The characteristic impedance of the double-sided parallel strip on a substrate of thickness w is twice as high in comparison with the impedance of a mictrostrip of thickness $w/2$ [21].

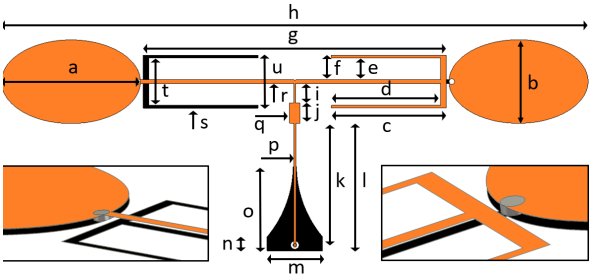

Fig. 2: Dimensions of the sleeve dipoles and feeding network.

Therefore, width p of the strip remains the same but the characteristic impedance is changed from 70.7 Ω to 100 Ω. The 100 Ω line is then followed by another impedance transformer consisting of a wider stub (25 Ω line) of width q and another short piece of 100 Ω line approximately of the same length (series-section transformer [22]). This part transforms the impedance of 100 Ω to 25 Ω. At this point two 50 Ω parallel strips of width r are connected with the feeding line (T-shaped strip).

The symmetric parallel strip then feeds two elliptical sleeve dipoles [23], [24] and the distance g between them is approximately $\lambda/2$ to avoid grating lobes. To keep the surface currents on the dipole antenna in phase, the antennas are mirrored. The top strip (orange) is connected to the elliptical radiator on the left side, while on the right side the top strip is connected to the sleeves. The bottom strip (black) is connected to the sleeves on the left side and to the elliptical radiating element on the right side. Furthermore, the elliptical radiating elements were printed on both sides of the PCB (Printed Circuit Board) and connected with a small VIA (Vertical Interconnect Access) presented as the grey cylinders in the detailed images. A VIA with a 2 mm diameter as used in the simulation was redesigned to have a 1.5 mm (VIA hole) diameter, so the distance between the edge of the elliptical radiator and the hole was 0.25 mm.

The following table shows all the dimensions presented in Fig. 2. It is worth noting that k is the length from the centre of the coaxial cable to the wide stub. Parameters p, q, r, and s present the width of the strips. The overall dimensions of the PCB board were 121.4 x 228 mm. FR-4 material of thickness 0.8 mm (permittivity of 4.3) was used. In the final design, a semi-rigid coaxial cable (RG402) was soldered to both the PCB with dipoles and the reflector so the connection was rigid. A small hole was made into the reflector for the coaxial cable.

TABLE I: Dimensions of The Sector Antenna

Symbol	Dimension (mm)	Symbol	Dimension (mm)
a	50	b	30
c	41.3	d	39.3
e	7.8	f	8.8
g	109	h	221
i	7	j	7.2
k	43.8	l	45.8
m	20	n	5
o	30.4	p	0.73
q	3.8	r	1.4
s	1	t	17
u	19	-	-

The geometry (unit cell) of the metasurface, as shown in Fig. 3, was designed as a two-layer PCB with overlapping patches placed above a ground plane. The overlapping technique allows the miniaturisation of the elements as it increases the inter-element coupling [25]. The lengths of x, y, z are 10 mm, 4.5 mm, and 9 mm respectively. The gaps between the patches are 1 mm thick. FR-4 material of the thickness of 1.6 mm was considered. The space between the ground plane and the periodic structure was 10 mm.

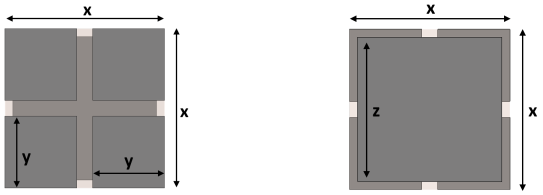

(a) Top view (b) Bottom view

Fig. 3: Metasurface - unit cell (without ground plane).

The calculation was based on Floquet's theorem [26], [27] and the reference plane was placed 5 mm in front of the metasurface where the position of the radiating element was considered.

As can be seen in Fig. 4, the phase of the reflection coefficient is 0° at the resonance frequency of 1.43 GHz. The metasurface covers all the GNSS bands within the range from -90° to 90° where the metasurface reflects the plane waves in-phase, rather than out-of-phase [15]. GNSS bands are marked in the figure by the colour bars. The green is in the frequency range from 1.164 GHz to 1.214 GHz, yellow from 1.26 GHz to 1.3 GHz and pink is from 1.559 GHz to 1.591 GHz.

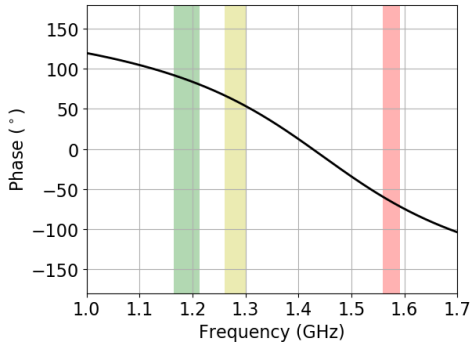

Fig. 4: Phase response of the metasurface, Galileo bands E6 (yellow) and E1 (pink) were prioritised.

In the next step the antenna board was placed above the finite metasurface and the side walls were added. The inner angle between the reflector and the side wall was 115.7°. After an optimisation, the final distance between the reflector and metasurface was 17 mm and the space between the metasurface and the antenna board was 3.2 mm. The overall dimensions of the metasurface were 110 x 290 mm and those of the reflector (ground) were 114 x 290 mm. The side walls

were made of 1 mm-thick double-sided PCB (FR-4) with dimensions of 25 x 290 mm and solid copper layers on both sides. The side walls were soldered to the flat reflector using a 3D-printed form that ensured the correct alignment.

Fig. 5 shows the reflection coefficient of the antenna board, antenna board with the metasurface and the complete sector antenna with both the metasurface and the side walls. The final design is also compared with the measurement.

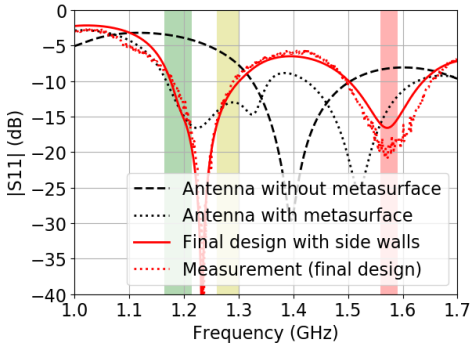

Fig. 5: Different stages of the sector antenna development.

Fig. 6 compares the simulations and measurements of the normalized radiation patterns. Each sector antenna was designed as an antenna array with two radiating elements (sleeve dipoles) causing a narrower beam in the vertical plane (E-plane) in comparison with the horizontal plane (H-plane). The simulated absolute gain of the sector antenna was 8.3 dBi at 1.278 GHz and 10 dBi at 1.575 GHz with the dielectric loss tangent of the FR-4 substrate of 0.025 and loss-free coaxial cable being considered.

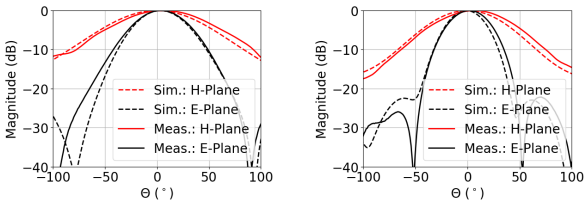

(a) 1.278 GHz (b) 1.575 GHz

Fig. 6: Simulated and measured far-field cuts of the sector antenna.

III. Anti-interference system

The designed sector antenna was further placed into a system allowing interference mitigation and localisation (Fig. 7). The system consists of a top antenna which creates the main RHCP beam for GNSS reception and seven sector antennas placed next to each other to form a regular heptagon. The design of the top antenna was based on a broadband crossed dipole [28]. It was optimised for the FR-4 substrate of thickness 0.8 mm and placed 62.5 mm above the heptagonal ground plane. The dimensions of the crossed dipole are presented in Fig. 8a. The height of the entire antenna system, including the top antenna, was 353.3 mm and the diameter was 315 mm.

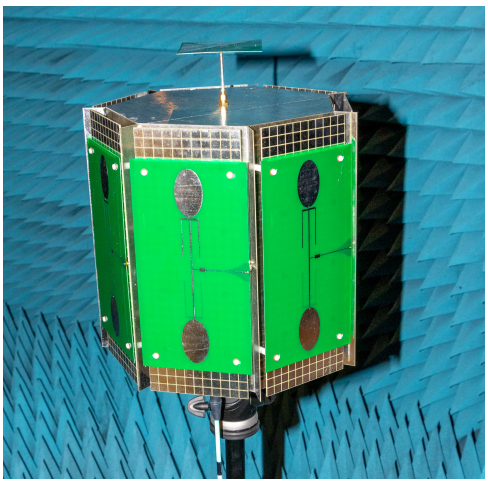

Fig. 7: The whole antenna system during measurement.

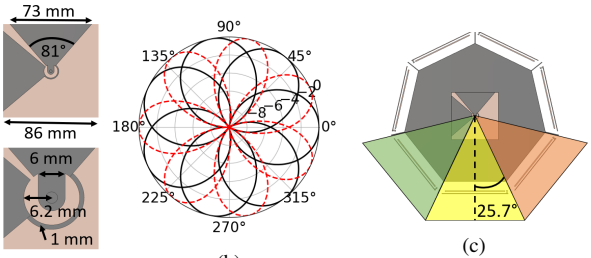

(a) (b) (c)

Fig. 8: (a) Top: tuned RHCP antenna [28] (top layer), bottom: feeding point, (b) Radiation pattern: single sector in black, two in-phase sector antennas in red, (c) Sector antenna look angle.

The radiation pattern of each sector antenna in the horizontal plane is presented by the black curve in Fig. 8b. The red curve shows the sum of two radiation patterns of two neighbouring antennas when they are fed in phase. Furthermore, Fig. 8c shows that the main beam of each sector antenna covers the angle from -25.7° to 25.7°. The 3D radiation patterns of the top and sector antennas are illustrated in Fig. 9.

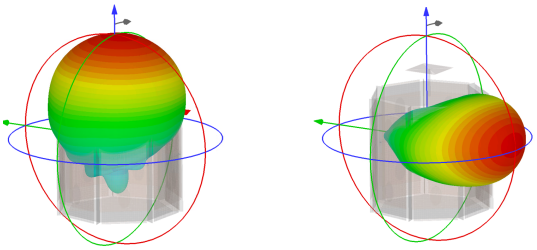

(a) (b)

Fig. 9: Radiation pattern of the (a) top RHCP antenna and (b) sector antenna at 1.278 GHz.

Fig. 10 shows the attenuation of interference when the radiation pattern of the top antenna is combined with one

sector antenna so that a deep null is created in the main beam. Two azimuths are presented: 0° and 25.7°. Also, it is shown that the part of the radiation pattern pointing into the sky is not affected by the nulling technique. To obtain the same gain of the sector antenna and the top antenna in the considered directions, the sector antenna was attenuated by 27.2 dB for azimuth of 0° and by 19.6 dB for azimuth of 25.7°.

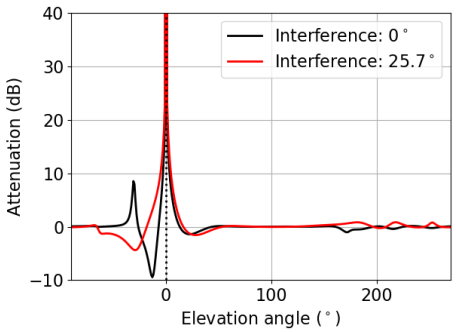

Fig. 10: Computed interference attenuation, 1.278 GHz.

Furthermore, the measurement of interference mitigation was performed using an eight-channel coherent software-defined radio receiver. All seven sector antennas were combined with the main RHCP beam and interference attenuation of 45 dB was achieved across the GNSS band.

Moreover, due to the low coupling between the antennas, when the sector antennas are placed next to each other in the complete system, the radiation patterns match well with the single antenna as presented in Fig. 11.

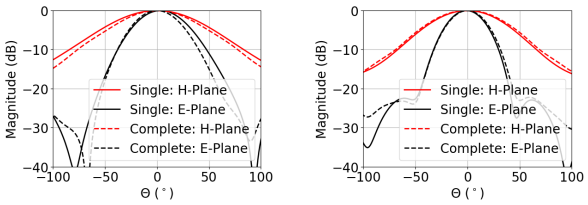

(a) 1.278 GHz (b) 1.575 GHz

Fig. 11: Simulated radiation patterns of a single sector antenna on its own and one sector antenna of the complete system.

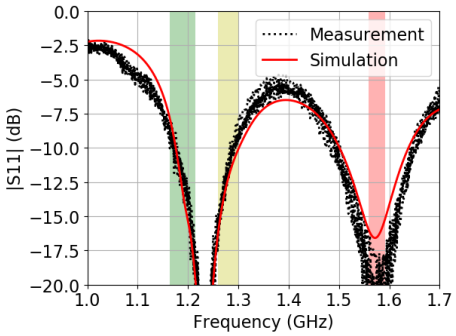

Fig. 12: Sector antenna: S11 simulation and measurement.

The simulated and measured reflection coefficients of all seven antennas can be seen in Fig. 12. The differences are given mainly by the manufacturing tolerances. Furthermore, isolation between the sector antennas was measured. As shown in Fig. 13, the worst isolation between two neighbouring sector antennas was 28 dB in the entire band. The sector antennas were marked clockwise meaning that antennas two and seven were located next to antenna one. The measured isolation between the top antenna and the sector antennas was higher than 38 dB.

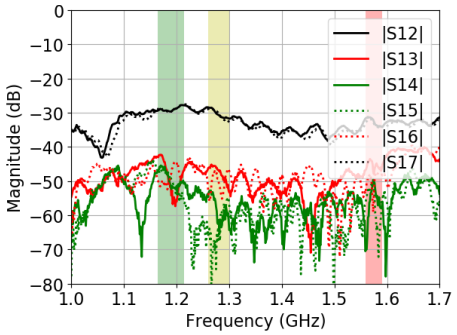

Fig. 13: Isolation between the sector antennas.

IV. Conclusion

A design of a sector antenna with a metasurface reflector for GNSS applications was presented. It offers low-profile compact geometry and good impedance matching for both Galileo and GPS bands where it provides a stable radiation pattern with no beam steering.

Furthermore, the sector antenna design was extended to an antenna system with interference mitigation capability. The system consisted of seven sector antennas and one crossed dipole antenna. Based on simulations and measurements, it was shown that interference was attenuated by approximately 45 dB.

As software defined radios (SDR) are becoming more affordable, classic analogue phasing networks can be replaced by digital processing techniques which allow the radiation patterns of the main antenna and the sector antennas to be combined. Therefore, there is a lot of space for further research to achieve maximum performance from this antenna system. Additionally, this system can be improved by adding antennas with horizontal polarisation and by modifying the top antenna based on the requirements such as better multipath mitigation.

The proposed antenna system could also be useful for interference localisation. If more such antenna systems were used, the location of the interfering transmitter could be found via triangulation. Inside the antenna system there is ample space for other equipment such as preamplifiers, filters, attenuators and possibly a receiver to enable the antenna to be manufactured as a complete receiving system.

V. Acknowledgement

Thanks to Intriple, a.s. for providing measurement results of the antenna system using a multi-port coherent software-defined radio.

REFERENCES

[1] S. Caizzone, W. Elmarissi, G. Buchner, and M. Sgammini, "Compact 6+1 antenna array for robust gnss applications," in *2016 International Conference on Localization and GNSS (ICL-GNSS)*, June 2016, pp. 1–4.

[2] L. T. Ong, "An interference cancellation scheme using a circular antenna array with a central element," in *2011 IEEE International Conference on Signal Processing, Communications and Computing (ICSPCC)*, Sep. 2011, pp. 1–5.

[3] S. H. Sedighy, "Null steering gps array in the presence of mutual coupling," *Iranian Journal of Electrical and Electronic Engineering*, vol. 14, pp. 116–123, 06 2018.

[4] A. K. Brown and B. Mathews, "Gps multipath mitigation using a three dimensional phased array," in *Proceedings of the 18th International Technical Meeting of the Satellite Division of The Institute of Navigation (ION GNSS 2005)*, Long Beach, CA, Sep. 2005, pp. 659 – 666.

[5] J. T. Curran, M. Bavaro, and J. Fortuny, "Analog and digital nulling techniques for multi-element antennas in gnss receivers," 09 2015.

[6] M. Brachvogel, M. Niestroj, S. Zorn, M. Meurer, S. N. Hasnain, R. Stephan, and M. A. Hein, "A new array concept using spatially distributed subarrays for unambiguous gnss interference mitigation in automotive applications," *NAVIGATION*, vol. 67, no. 1, pp. 23–41, 2020. [Online]. Available: https://onlinelibrary.wiley.com/doi/abs/10.1002/navi.353

[7] M. Sgammini, S. Caizzone, A. Hornbostel, and M. Meurer, "Interference mitigation using a dual-polarized antenna array in a real environment," *NAVIGATION*, vol. 66, no. 3, pp. 523–535, 2019. [Online]. Available: https://onlinelibrary.wiley.com/doi/abs/10.1002/navi.309

[8] T. B. Vu, "On null steering in rectangular planar array," *IEEE Transactions on Antennas and Propagation*, vol. 40, no. 8, pp. 995–997, 1992.

[9] M. S. Sharawi and D. N. Aloi, "Null steering approach with minimized pcv and gd for large aperture vertical antenna arrays," *IEEE Transactions on Antennas and Propagation*, vol. 55, no. 7, pp. 2120–2123, 2007.

[10] S. Sadat, C. Ghobadi, and J. Nourinia, "Mutual coupling compensation in small phased array antennas," in *IEEE Antennas and Propagation Society Symposium, 2004.*, vol. 4, 2004, pp. 4128–4131 Vol.4.

[11] Q. W. Pan, "Coplanar waveguide collinear array multiband pcb antenna," in *2012 IEEE Symposium on Wireless Technology and Applications (ISWTA)*, Sep. 2012, pp. 198–201.

[12] K.-L. Wong and J.-H. Chou, "Printed collinear two-antenna element for wlan access points in a mimo system," *Microwave and Optical Technology Letters*, vol. 48, no. 5, pp. 930–933, 2006. [Online]. Available: https://onlinelibrary.wiley.com/doi/abs/10.1002/mop.21522

[13] Y. Li, B.-H. Zeng, C.-W. Chen, D.-C. Chang, Z. Li, J. Liu, and H.-B. Liang, "High performance planar sleeve dipole array antenna with directional radiation," *Progress In Electromagnetics Research C*, vol. 21, pp. 169–177, 01 2011.

[14] H. Errifi, B. Abdennaceur, A. Badri, and S. Aicha, "Design and analysis of directive microstrip patch array antennas with series, corporate and series-corporate feed network," *International Journal of Electronics and Electrical Engineering*, vol. 3, 12 2015.

[15] D. Sievenpiper, Lijun Zhang, R. F. J. Broas, N. G. Alexopolous, and E. Yablonovitch, "High-impedance electromagnetic surfaces with a forbidden frequency band," *IEEE Transactions on Microwave Theory and Techniques*, vol. 47, no. 11, pp. 2059–2074, 1999.

[16] S. X. Ta, Q. Ho, K. Nguyen Khac, and C. Dao-Ngoc, "Single-dipole antenna on a metasurface for broadband circularly polarized radiation," *Journal of Electromagnetic Waves and Applications*, pp. 1–15, 10 2017.

[17] L. Akhoondzadeh-Asl, D. J. Kern, P. S. Hall, and D. H. Werner, "Wideband dipoles on electromagnetic bandgap ground planes," *IEEE Transactions on Antennas and Propagation*, vol. 55, no. 9, pp. 2426–2434, 2007.

[18] G. Kompa, "Design of stepped microstrip components," *Radio and Electronic Engineer*, vol. 48, no. 1.2, pp. 53–63, 1978.

[19] W. A. Imbriale, *Spaceborne Antennas for Planetary Exploration*, J. H. Yuen, Ed. John Wiley & Sons, Ltd, 2006.

[20] G. Engargiola, "Tapered microstrip balun for integrating a low noise amplifier with a nonplanar log periodic antenna," *Review of Scientific Instruments*, vol. 74, no. 12, pp. 5197–5200, 2003. [Online]. Available: https://doi.org/10.1063/1.1622975

[21] S.-G. Kim and K. Chang, "Ultrawide-band transitions and new microwave components using double-sided parallel-strip lines," *Microwave Theory and Techniques, IEEE Transactions on*, vol. 52, pp. 2148 – 2152, 10 2004.

[22] F. A. Regier, "Impedance matching with a series transmission line section," *Proceedings of the IEEE*, vol. 59, no. 7, pp. 1133–1134, 1971.

[23] Seo-Cheol Jung, Yoon-Seon Choi, and Jong-Myung Woo, "Small sleeve dipole antenna using inner short stub," in *2014 20th International Conference on Microwaves, Radar and Wireless Communications (MIKON)*, 2014, pp. 1–3.

[24] D. Chang and Y. Su, "Frequency reconfigurable sleeve dipole array for ieee802.11a/b," in *2016 IEEE International Workshop on Electromagnetics: Applications and Student Innovation Competition (iWEM)*, 2016, pp. 1–2.

[25] F. Capolino, *Theory and Phenomena of Metamaterials*. CRC Press, 2009.

[26] R. E. Collin, *Field Theory of Guided Waves*. Wiley-IEEE Press, 1991.

[27] E. K. . J. S. . M. Tuley, *Radar Cross Section*. SciTech Publishing, 2004.

[28] H. Tran, S. X. Ta, and I. Park, "Single-feed, wideband, circularly polarized, crossed bowtie dipole antenna for global navigation satellite systems," *Journal of electromagnetic engineering and science*, vol. 14, pp. 299–305, 09 2014.

[29] C. A. Balanis, *Antenna Theory*. Hoboken, New Jersey: John Wiley and Sons, 2005.

Compact Uplink RHCP 2.4GHz Short Backfire Antenna for Geostationary Amateur Radio Satellite Es'Hail-2 (QO-100)

Michal Cerveny, Pavel Hazdra

***Abstract*—This paper describes a compact circularly polarized antenna designed for the 2.4GHz band with a gain of 15dBi. The proposed antenna upgraded a standard short backfire antenna (SBA) by utilizing two metasurfaces. The first one acted as a high-impedance surface (HIS) allowing for a reduction of the distance between the sub-reflector and main reflector, while the second metasurface split the polarization and provided a phase shift of 90° needed for circular polarization. In this design, a linearly polarized patch antenna was used as a feeder. The antenna was simulated, measured, optimized and tested on the QO-100 transponder located on the Es'Hail-2 geostationary satellite. The direction of rotation of the circular polarization (right or left) can be easily changed by rotating the second metasurface by 90°. This antenna can be used in situations where compactness, portability and rigid construction are required.**

***Index Terms*—Antenna, Satellite, Metasurface, QO-100, Es'Hail-2, SBA.**

I. Introduction

WITH the launch of the first geostationary amateur radio transponder Qatar Oscar-100 (QO-100) on the Es'Hail-2 satellite on 15 November 2018, the interest in satellite communications increased rapidly inside the amateur radio community. Geostationary satellite allows for easier operation without any significant Doppler shift, the need for tracking antenna system, and provides a continuous communication service covering a third of the globe. QO-100 operates in the S and X bands. Downlink is present at 10.4GHz with linear polarization and uplink at 2400.25MHz ±250kHz with right-hand circular polarization (RHCP).

Typically, the standard antenna configuration of a ground station is based on a parabolic antenna with a dual-band feeder which combines an open waveguide with a dielectric lens and a patch antenna [1], or a helical antenna with a horn antenna [2]. The second common configuration is based on separate uplink and downlink antennas. In addition, circularly polarized helical antennas are used.

Michal Cerveny is with the Department of Electromagnetic Field, Faculty of Electrical Engineering, Czech Technical University in Prague, Technicka 2, 166 27, Prague, Czech Republic and the Department of Electronic and Electrical Engineering, The University of Sheffield, Sheffield S1 4ET, UK.

Pavel Hazdra is with the Department of Electromagnetic Field, Faculty of Electrical Engineering, Czech Technical University in Prague, Technicka 2, 166 27, Prague, Czech Republic (e-mail: hazdrap@fel.cvut.cz).

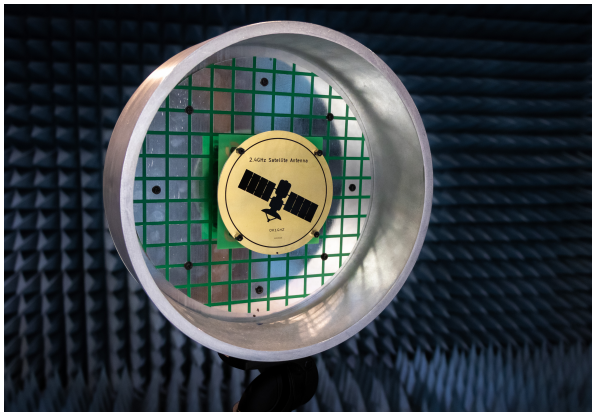

Fig. 1: Proposed 2.4GHz RHCP satellite antenna.

There are many cases where the portability, compactness and robustness of the satellite ground system is an important factor, as well as the low profile of the antenna. Unfortunately, the number of suitable antennas is quite limited and solutions based on large antenna arrays made of high quality substrates to reduce losses can be quite expensive.

An interesting solution is offered by short backfire antennas (SBA). The underlying concept has been known about for a long time, as shown in a paper from 1965 [3]. Since then, various SBA modifications have been published. For example, to achieve a higher bandwidth, the rim [4], [5] or the exciter [6], [7] were studied and modified. Furthermore, phase-modulated metasurface for beam deflection[8], dual-band [9], [10], a circularly polarized SBA excited by a cross aperture [11], [12] or a polarization reconfigurable antenna [13] were reported. It has also been found that the shape of the reflector can improve the antenna gain [14]. Other modifications utilized a metasurface (high impedance walls) for maximum aperture efficiency [15] or corrugated walls to suppress sidelobes [16].

A typical SBA design consists of a reflector and a sub-reflector that are spaced approximately half a wavelength apart. A dipole antenna is then placed between the reflectors. Such a configuration requires symmetrization. Unfortunately, a good mechanical design can be quite complex to implement and it is even more challenging when a circular polarization is required.

Therefore, it was necessary to find a new solution where no crossed dipoles or crossed slots were needed. Only basic

shapes were considered as it simplifies the manufacturing process and reduces costs. For that reason, no corrugated walls or conical rims were used.

Since metasurfaces are an excellent option for polarization manipulation, they can be implemented in antenna systems to enhance their performance. Therefore, the advantages of an SBA and a metasurface were combined and a circularly polarized antenna with a patch antenna as the feeder was designed. To keep the assembly part as simple as possible, all components of the antenna were manufactured as printed circuit boards (PCBs) except for the antenna rim, which was fabricated by computer numerical control (CNC) machining.

II. Design of the Antenna

The proposed antenna consisted of several parts as shown in Fig. 2. Above the patch antenna located at the bottom of the SBA, a high-impedance surface (Metasurface 1) was placed. This metasurface reduced the required distance between the reflector and sub-reflector from $\lambda/2$ to $\lambda/2.57$.

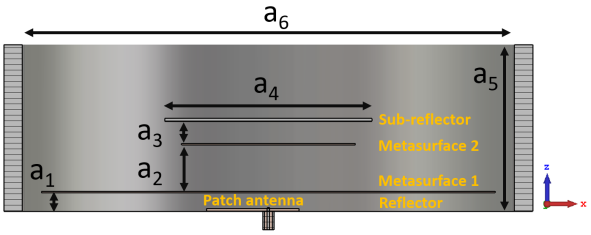

Fig. 2: Cut through the proposed short backfire antenna.

The sub-reflector was made as a second metasurface (Metasuface 2) and was placed $\lambda/5$ above the HIS at the distance of 25mm (a_2). The design was based on split-ring resonators which is a well-known type of metasurface allowing polarization conversion. In this design, however, the metasurface was not designed as a standard polarization rotator [17], [18] where the maximum polarization conversion is required but as a spatial power divider which allowed to change the ratio of the reflected co-polarized and cross-polarized electromagnetic waves. Furthermore, such polarization convertor introduced a phase shift of 90° which was required for generating the circular polarization. Therefore, the feeding point could be designed as a standard linearly polarized patch antenna.

The diameter of the sub-reflector was 112mm (a_4), its thickness was 1.6mm and the air gap was 12mm (a_3). On the manufactured antenna this gap was later increased to 13mm. Furthermore, the height of the rim was 90mm (a_5) and its inner diameter was 266mm (a_6). The thickness of the rim was 10mm.

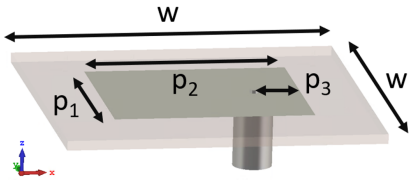

Fig. 3: Patch antenna.

The patch antenna is shown in Fig. 3. Initially, this antenna was designed with FR-4 dielectric to make the antenna relatively inexpensive. Unfortunately, this component was found to significantly affect the overall gain, as the antenna with the FR-4 substrate had a gain 1.3dB lower than with the Rogers 4350B substrate.

In addition, it was expected that higher RF power would be required to achieve the optimum signal strength received by the satellite. Therefore, heating of the lossy substrate was a second consideration. For these reasons, the final patch antenna design was based on the Rogers 4350B substrate. The dimension w was 50mm, p_1 was 27mm, p_2 was 31.25mm and p_3 was 7.17mm. The thickness of the substrate was considered to be 1.524mm.

The high-impedance surface consisted of periodic structure of squares printed on the FR-4 dielectric of thickness of 0.8mm. The top view of the unit cell can be found in Fig. 4a. Dimension a was 16.85mm and b was 20mm. The top view of the entire HIS is shown in Fig. 4b. The diameter of the metasurface was 245.3mm and the air gap between the substrate and the reflector (a_1, Fig. 2) was 10mm.

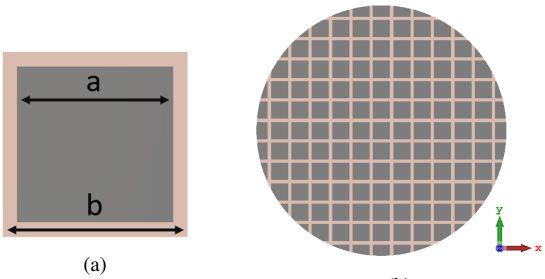

(a) (b)

Fig. 4: High-impedance surface: (a) unit cell, top view, (b) entire Metasuface 1.

The second metasurface was also designed on the FR-4 substrate of the considered thickness of 0.8mm. The metasurface was designed as a double split-ring resonator (Fig. 5).

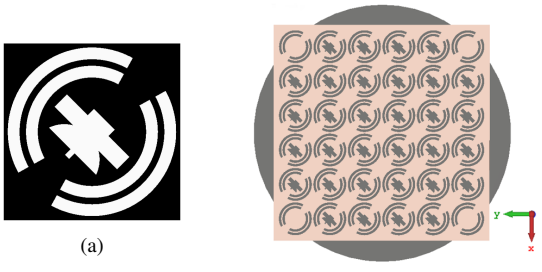

(a) (b)

Fig. 5: (a) Metasurface 2 - unit cell, (b) entire Metasuface 2 in front of the sub-reflector.

The unit cell of the resonator was a square with dimensions of 15x15mm (Fig. 5a). It was intentionally printed in black and

white colors because current software tools allow such images to be converted into printed circuit board (PCB) layouts. The white color presents the conductive layer. For reference, the thickness of the rings was 1mm and the gap between the smaller ring and the larger one was 0.55mm. The satellite icon in the center of the unit cell did not have a significant effect in the required frequency range. The dimensions of the entire PCB were 94x94mm (Fig. 5b).

The following figures present the phase (Fig. 6) and magnitude (Fig. 7) of the co-polarized reflection coefficients (r_{xx}) and cross-polarized reflection coefficients (r_{yx}). The simulation was performed by using a single unit cell with periodic boundary conditions. The different colors represent the effect of various heights of the metasurface above a ground. It can be seen that the resulting phase difference between the two orthogonal polarizations stays the same across the required frequency range. On the other hand, the ratio of the magnitudes can be adjusted by this parameter. The frequency range of the QO-100 narrow band transponder is represented by the vertical green line.

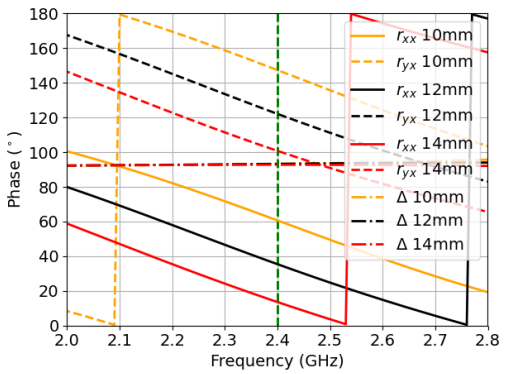

Fig. 6: Simulation: phase (Metasurface 2).

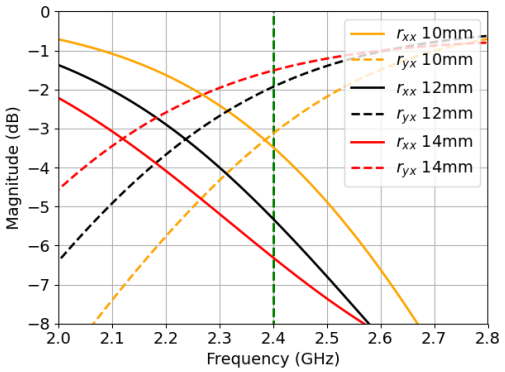

Fig. 7: Simulation: magnitude (Metasurface 2).

The entire antenna was then simulated using a frequency domain solver based on the finite element method in CST Microwave Studio and the antenna was optimized. Fig. 8 shows the simulated 3D RHCP radiation pattern of the antenna. The obtained gain was 15dBi. Furthermore, two cuts (Φ = 0° and Φ = 90°) of the radiation pattern including the cross-polarization (LHCP) are presented in Fig. 9.

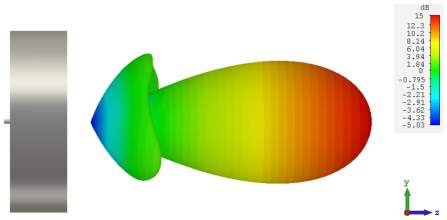

Fig. 8: Simulation: 3D radiation pattern, RHCP, 15dBi.

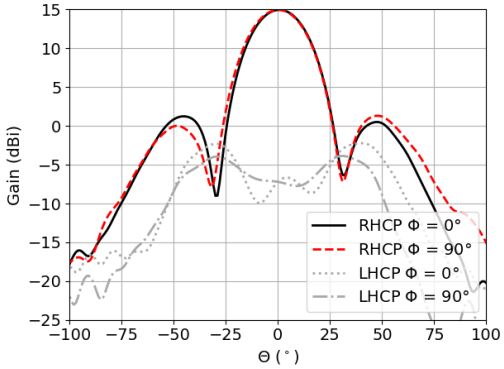

Fig. 9: RHCP, LHCP radiation patterns.

The obtained axial ratio of the antenna can be seen in Fig. 10.

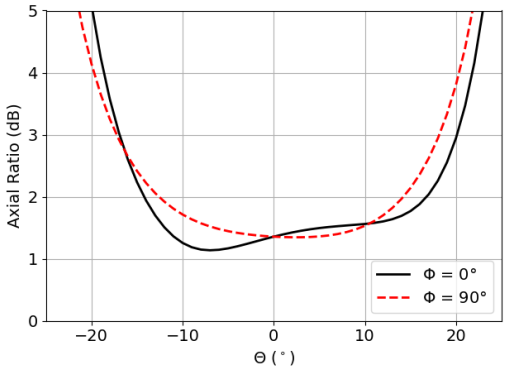

Fig. 10: Axial ratio.

It should be noted that the proposed design allows an easy change of the resulting direction of the circular polarization (right-hand circular polarization (RHCP) and left-hand circular polarization (LHCP)) simply by rotating the Metasurface 2 by 90°.

III. Measurement

The antenna was manufactured, assembled and measured. It was found that due to a manufacturing imperfection, the antenna was very sensitive to the placement of the patch antenna on the reflector, which was made of 2mm thick FR-4 substrate. Since neither the reflector nor the patch was completely flat, there was a small gap between the patch and the reflector which affected the resonant frequency. Therefore, the patch antenna had to be pressed and glued to the reflector and then soldered to an SMA connector to eliminate any air gap.

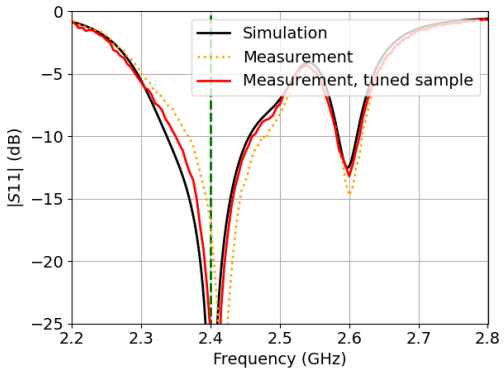

Fig. 11: Measured and simulated $|S11|$ parameters.

It was found that the resonant frequency was slightly above the desired frequency. To tune the antenna to the required frequency range, a small piece of aluminum EMI shielding tape was used and the length of the patch antenna was increased based on the measurement. Fig. 11 shows both the tuned and the original measurement without the tape. For a future design, a double-sided PCB with the bottom side covered with a copper layer would probably be a better choice, as the large capacitance between the bottom layer of the patch antenna and the reflector could mitigate the high sensitivity to small air gaps.

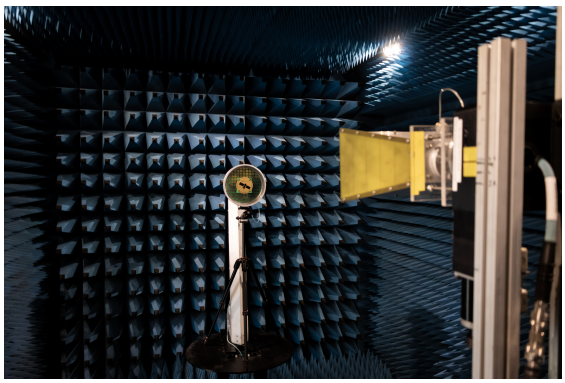

Fig. 12: Radiation pattern measurement.

The radiation patterns were measured with a linearly polarized horn antenna in an anechoic chamber (Fig. 12). Firstly, the radiation pattern was measured when the horn antenna was vertically polarized (φ = 0°). The horn antenna was then rotated by 90° (φ = -90°) around its axis and measured again. Both components, vertical and horizontal, are shown in Fig. 13 and Fig. 14 and compared with the simulations.

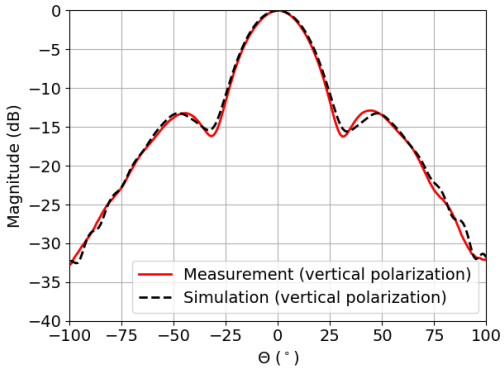

Fig. 13: Far-field pattern: vertical component, Φ = 90°.

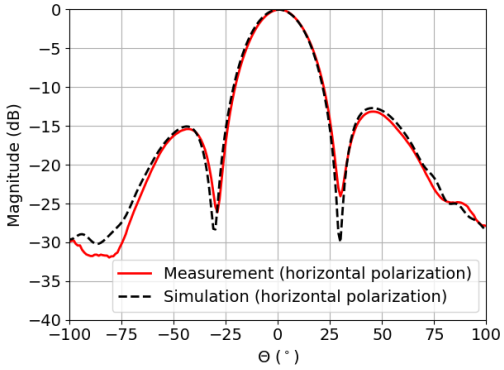

Fig. 14: Far-field pattern: horizontal component, Φ = 90°.

Then the polarization envelope (Fig. 15) was measured at the center frequency by axial rotation of the horn antenna with the step of 5°. The obtained axial ratio was 1.34.

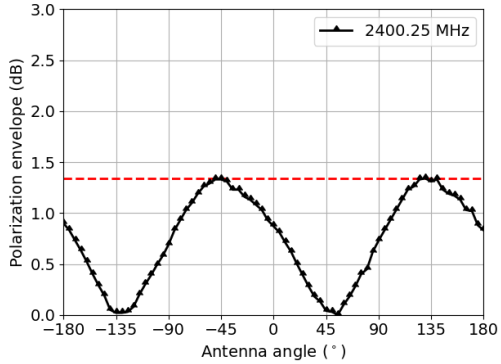

Fig. 15: Polarization envelope measurement.

Unfortunately, our laboratory was not equipped with any RHCP and LHCP antenna in the required frequency region. Therefore, a measurement method based only on linear-component amplitudes [19] was used. For this method a second set of orthogonal linearly polarized radiation patterns (magnitudes) had to be measured. Together with the previous radiation pattern measurements, two sets of orthogonal linearly polarized magnitudes E_1, E_2, E_3, E_4 were obtained at φ = 0°, -90°, -45° and 45°.

The axial ratio was calculated using the following equation (1) and the results can be seen in Fig. 16.

$$AR = \sqrt{\frac{E_1^2\cos^2(\tau) + \frac{1}{2}(E_3^2 - E_4^2)\sin(2\tau) + E_2^2\sin^2(\tau)}{E_1^2\sin^2(\tau) - \frac{1}{2}(E_3^2 - E_4^2)\sin(2\tau) + E_2^2\cos^2(\tau)}} \quad (1)$$

where

$$\tau = \frac{1}{2}\arctan\frac{E_3^2 - E_4^2}{E_1^2 - E_2^2}. \quad (2)$$

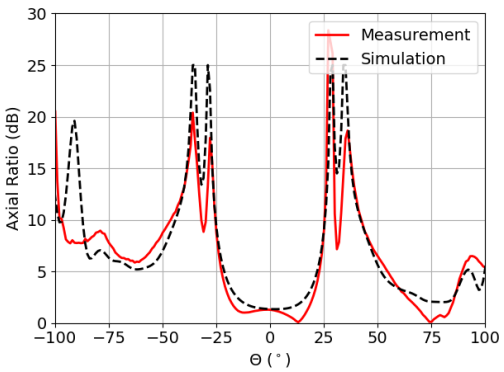

Fig. 16: Axial ratio at the center frequency 2400.25MHz.

The RHCP and LHCP radiation patterns were computed using equations (3) and (4).

$$E_{RHCP} = \sqrt{\frac{(E_1^2 + E_2^2)}{1 + \Gamma^2}} \quad (3)$$

$$E_{LHCP} = \sqrt{\frac{\Gamma^2(E_1^2 + E_2^2)}{1 + \Gamma^2}} \quad (4)$$

where

$$\Gamma = \frac{AR - 1}{AR + 1}. \quad (5)$$

The obtained far-field patterns were compared with simulations in Fig. 17. It can be seen that the antenna had a cross-polarization of -22dB at its peak directivity.

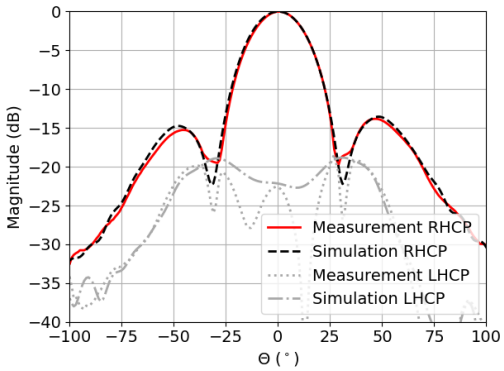

Fig. 17: RHCP and LHCP radiation patterns, Φ = 90°.

It should be noted that manufacturing tolerances can be quite high. It is known that the permittivity of an FR-4 substrate can range from approximately 3.3 to 4.8 [20]. To work around this problem, more expensive substrates with a better defined dielectric constant can be used. Unfortunately, the problem is not only the dielectric constant, but also the thickness of the PCB. For example, the declared thickness accuracy of the Rogers 4350B 1.524 mm thick substrate is ±0.004" (±0.1mm). In addition, the boards must be cut to the desired shape. For standard circuit boards, the accuracy of the cut is usually not a critical parameter; however, it is important for antenna applications. In addition, PCBs are sometimes slightly bent. As can be seen, there are many variables that can affect the antenna and reduce its performance. This means that this antenna (consisting of three circuit boards) will need to be tuned before use.

IV. Practical tests with the QO-100 narrow band transponder

This section presents a practical test performed with the proposed antenna. A transceiver Yaesu FT-818 was used as an intermediate frequency (IF) transmitter operating at 144MHz. Furthermore, an up-convertor to the S band was used followed by an amplifier providing a power of 42dBm (approximately 16W).

Firstly, the CW modulation was tested and compared with the signal level of the CW beacon. It should be noted that the uplink signal must not be stronger than this beacon, which is an operational requirement. Compared to the CW beacon, the tested system with the proposed antenna produced a 3.3dB lower signal level. Fig. 18 shows the CW signal of the tested system at 10.48950747GHz (downlink frequency) which can be seen in the waterfall on the right-hand side. The beacon was present on the left-hand side.

Fig. 19 shows an SSB test. The produced signal could be clearly seen on the waterfall. Both figures (screenshots) were taken from an online WebSDR [21], hosted at Goonhilly Earth Station in Cornwall, UK. This WebSDR receives the downlink frequency (X-band) of QO-100, provides real-time reception and can be controlled remotely via a web browser.

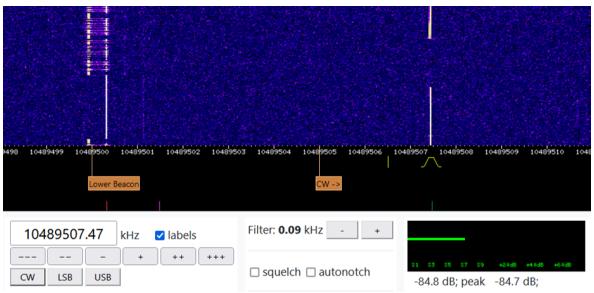

Fig. 18: CW modulation: on the left hand-side the CW beacon was present, the carrier on the right-hand side was produced by the tested system.

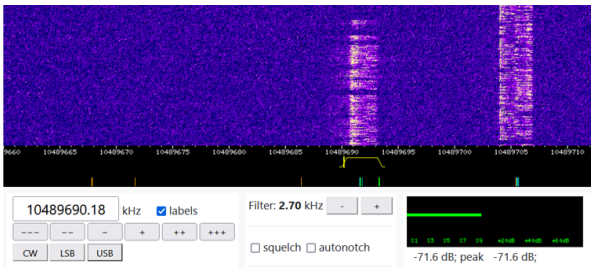

Fig. 19: SSB modulation: the signal on the left-hand side was produced by the tested system.

Both CW and SSB modulations were tested and both of them could be used for making radio contact via the satellite.

V. Conclusion

This work presented a short backfire antenna (SBA) using a novel technique for generating a circular polarization. This was achieved by using a metasurface inside the SBA's open cavity. The gain of the antenna was 15dBi and the overall dimensions were 286mm x 92mm (excluding the tripod holder and the SMA connector on the back side). Due to its compactness and the absence of protruding parts present in the dish-type antennas, this antenna can be easily transported and used in situations where antenna space limitations or restrictions are in place. The antenna was designed with ease of assembly in mind, so no special mechanical tools should be necessary. The antenna provided a very good impedance match (return loss was better than 20dB) and axial ratio (1.34) at the desired frequencies.

The antenna was tested with QO-100 narrow band transponder. With an output power of 16W (ERP = 308.5W), the system was capable of providing enough radiated power to make contact using both CW (telegraph) and SSB modulation. The downlink was secured by WebSDR, hosted at Goonhilly Earth Station in Cornwall, UK providing the evidence of the signal levels. Based on the WebSDR's signal meter, this system produced 3.3dB lower signal level than the CW beacon.

The RHCP and LHCP polarization can be changed by rotating the top metasurface (Metasurface 2) by 90°. This makes the antenna very universal as the same design can be used for both polarizations. Future modifications may include the implementation of a rotating mechanism that would be able to switch between the RHCP and LHCP polarization electromechanically.

VI. Acknowledgment

The authors would like to thank Dr. Rastislav Galuscak for providing valuable feedback.

References

[1] M. Bopp, "Comparison of dualband feeds poty and from dj7gp for qo-100,"
[2] K. Haber, "Conversion of an octagon twin lnb for qo-100 reception,"
[3] H. Ehrenspeck, "The short-backfire antenna," *Proceedings of the IEEE*, vol. 53, no. 8, pp. 1138–1140, 1965.
[4] G. S. Kirov, "Design of short backfire antennas [antenna designer's notebook]," *IEEE Antennas and Propagation Magazine*, vol. 51, no. 6, pp. 110–120, 2009.
[5] P. Hazdra and M. Mazánek, "Wideband shorted backfire antenna with l-probe fed microstrip patch," in *Proceedings of the Fourth European Conference on Antennas and Propagation*, pp. 1–3, 2010.
[6] S.-W. Qu, "Broadband millimeter-wave short backfire antenna with bowtie exciter," *IEEE Antennas and Wireless Propagation Letters*, vol. 11, pp. 850–853, 2012.
[7] R. Li, D. Thompson, M. Tentzeris, J. Laskar, and J. Papapolymerou, "Development of a wide-band short backfire antenna excited by an unbalance-fed h-shaped slot," *IEEE Transactions on Antennas and Propagation*, vol. 53, no. 2, pp. 662–671, 2005.
[8] G.-N. Zhou, B.-H. Sun, Q.-Y. Liang, Y.-H. Yang, and J.-H. Lan, "Beam-deflection short backfire antenna using phase-modulated metasurface," *IEEE Transactions on Antennas and Propagation*, vol. 68, no. 1, pp. 546–551, 2020.
[9] K. L. Lau and K. M. Luk, "A wideband circularly polarized l-probe coupled patch antenna for dual-band operation," in *TENCON 2005 - 2005 IEEE Region 10 Conference*, pp. 1–5, 2005.
[10] S. Srikanth and G. Behrens, "A new broadband short-backfire antenna as a prime focus feed single and dual band," in *2007 IEEE Antennas and Propagation Society International Symposium*, pp. 3684–3687, 2007.
[11] R. Li, D. Thompson, J. Papapolymerou, J. Laskar, and M. Tentzeris, "A circularly polarized short backfire antenna excited by an unbalance-fed cross aperture," *IEEE Transactions on Antennas and Propagation*, vol. 54, no. 3, pp. 852–859, 2006.
[12] D. Thompson, R. Li, J. Papapolymerou, J. Laskar, and M. Tentzeris, "New short backfire antennas for wireless applications," in *2005 IEEE Antennas and Propagation Society International Symposium*, vol. 2A, pp. 371–374 vol. 2A, 2005.
[13] G. Lin, Y. Cui, and R. Li, "High-gain polarization reconfigurable antennas," in *2018 International Symposium on Antennas and Propagation (ISAP)*, pp. 1–2, 2018.
[14] C. Cui, J. Lei, H. Xu, L. Yang, and M. Ling, "The design of a high-gain short backfire antenna," in *2012 International Conference on Microwave and Millimeter Wave Technology (ICMMT)*, vol. 3, pp. 1–4, 2012.
[15] E. Lier, T. H. Hand, E. A. Pierson, D. Binion, and D. H. Werner, "Demonstration of 3d printed hexagonal high gain short backfire antenna with hard em walls," in *2018 IEEE International Symposium on Antennas and Propagation USNC/URSI National Radio Science Meeting*, pp. 1711–1712, 2018.
[16] Y.-J. Hwang, C.-C. Lin, S. Srikanth, C. Anderson, C.-T. Ho, S. White, and P. Timbie, "Short-backfire antenna with corrugated reflector for radio astronomical array receivers," in *2019 URSI Asia-Pacific Radio Science Conference (AP-RASC)*, pp. 1–4, 2019.
[17] Z. Xu, H. Sheng, Q. Wang, L. Zhou, and Y. Shen, "Terahertz broadband polarization converter based on the double-split ring resonator metasurface," *SN Applied Sciences*, vol. 3, no. 9, pp. 1–7, 2021.
[18] K.-k. Xu, Z.-y. Xiao, and J.-y. Tang, "Linearly polarized converters for reflected and transmitted waves based on double-split ring resonator," *Plasmonics (Norwell, Mass.)*, vol. 12, no. 6, pp. 1869–1874, 2016.
[19] D. Wang, M. Wang, N. Xu, and W. Wu, "Improved measurement method of circularly-polarized antennas based on linear-component amplitudes," *Open Journal of Antennas and Propagation*, vol. 05, pp. 36–45, 01 2017.
[20] Z. Peterson, "Fr4 dielectric constant and material properties," Feb.
[21] "Qatar-oscar 100 narrowband websdr," Feb. 2022.

[22] C. A. Balanis, *Antenna Theory*. Hoboken, New Jersey: John Wiley and Sons, 2005.

[23] D. Sievenpiper, Lijun Zhang, R. F. J. Broas, N. G. Alexopolous, and E. Yablonovitch, "High-impedance electromagnetic surfaces with a forbidden frequency band," *IEEE Transactions on Microwave Theory and Techniques*, vol. 47, no. 11, pp. 2059–2074, 1999.

Michal Cerveny received a M.Sc. degree from Czech Technical University (CTU), Prague, Czechia, in 2014, where he is currently working towards a Ph.D. degree, with a focus on controlling the propagation of electromagnetic waves using artificial materials. In 2014, he started working as a Visiting Researcher with The University of Sheffield, Sheffield, U.K., working on wireless friendly energy-efficient buildings. In 2015, he worked with the Rolls-Royce University Technology Centre, Sheffield, U.K., doing RF modeling within marine environments. Since 2016, he has been working with The University of Sheffield, as a Research Associate in applied electromagnetics.

Pavel Hazdra was born in Prague, Czech Republic in 1977. He received his M.Sc. and Ph.D. degree in Electrical Engineering from the Czech Technical University in Prague, in 2003 and 2009, respectively. Since 2012 he has been Associate professor with the Department of Electromagnetic Field at the CTU in Prague. He has authored or co-authored more than 120 journal and conference papers. His research interests are in the area of EM/antenna theory, electrically small antennas, reflector antennas and their feeds and antennas for amateur radio purposes.

5 Conclusion

This thesis addressed several problems in the field of electromagnetic simulations, electromagnetic propagation inside buildings and antenna design all based on frequency selective surfaces and metasurfaces. The following paragraphs summarise the results achieved.

The aim of the first topic was to compare two methods (the induced EMF method and the spectral domain method) in calculating the input impedance and impedance quality factor of a dipole. The induced EMF method was found to be more convenient than the spectral domain method as it was in a closed-form solution and the required calculation time was significantly shorter. From a practical point of view, the EMF method can be used for a quick dipole impedance determination. When the feeding point or the surrounding environment needs to be considered, numerical methods based on full-wave electromagnetic analysis e.g., the method of moments, the finite element method or the finite-difference time-domain method will provide more accurate results. The research was supported by the Complex Artificial Electromagnetic Structures and Nanostructures project.

The following work was part of the Wireless Friendly and Energy Efficient Buildings (WiFEEB) project where the main focus of the author's research was on the control of wireless propagation within buildings. This included the study of the effect of a conductive carpet placed on the floor of a room in a Victorian house, the design of a transparent frequency selective surface that could be placed in the window of secure buildings and a concept of sparse FSSs placed between two adjacent rooms for the modification of the electromagnetic field distribution. Based on both simulation and measurement, it was found that by using frequency selective surfaces the propagation of electromagnetic waves can be efficiently controlled.

To take it a step further, two techniques for metasurface synthesis were compared. With these techniques the scattering waves can be reflected to prescribed directions. This is the key functionality for reflecting surfaces where the basic idea is to focus the electromagnetic field towards users and improve the signal-to-noise ratio. It was found that both techniques based on a holographic technique and on susceptibility tensors provided similar results even though the holographic method was easier to implement and did not change the magnitude of the reflection coefficient which is difficult to implement in practice. On the other hand, even if the magnitude part was ignored and only the phase response was considered, the predicted scattering patterns were nearly identical for both methods.

Based on the synthesis techniques presented, two metasurfaces were designed, manufactured and measured. One of them was made of a standard FR-4 substrate, the other was made of textile and was manufactured by an electroplating process. Both were designed for an angle of incidence of 45° and an angle of reflectance of 60°. It was found that by changing the discrete phase-steps the side lobes can be altered but the main lobe stays stable. This means that techniques which do not allow high precision manufacturing (such as electroplating process) can be still useful for some applications as the the main lobe is dominantly determined by the

periodicity of the entire structure. As the electroplating process requires current flow, the metasurface design has to be adopted for this technique which can be a limiting factor for more complex structures.

Furthermore, a novel active metasurface capable of rotating the polarisation by 90° and switching the relative phase of the reflected electromagnetic wave by 180° was presented. The metasurface was manufactured and the results measured were in alignment with the numerical simulations. It provided a stable phase difference of 180° across the entire usable bandwidth (4.8-6.2GHz). It was presented that in combination with a simple dipole antenna placed in front of the metasurface, a switchable antenna with right-hand/left-hand circular polarisation (RHCP, LHCP) as well as linear polarisation (LP) can be made. Such a system can also be attractive for secure wireless systems as it can provide polarisation scrambling and polarisation diversity.

The following project dealt with a practical requirement for a GNSS anti-interference system to make it capable of interference localisation and mitigation. Dual-band operation was required and it was assumed that the source of interference is located on the ground. Therefore, an antenna system that covered the low angles above the Earth's surface while having the main RHCP beam for GNSS reception covering the sky had to be designed. To reduce the overall dimensions of the antenna system, the designed sector antennas had to be low-profile. As a result, a novel GNSS sector antenna using a high impedance reflector was designed. The system as a whole was able to attenuate the interference by 45dB.

The final project presented a short backfire antenna using a novel technique for generating circular polarisation. The antenna leveraged a metasurface inside the SBA's open cavity. The metasurface was designed as a spatial power divider which allowed the ratio of the reflected co-polarised and cross-polarised electromagnetic waves to be changed while providing a phase shift of 90° needed for circular polarisation. Therefore, the feeding point could be designed as a standard linearly polarised patch antenna.

It was presented that frequency selective surfaces and metasurfaces can provide many opportunities for both research and practical applications. On the other hand, no technology is perfect and has to be used with its limitations in mind. For instance, a combination of high-power transmitters with antennas based on active metasurfaces controlled by diodes might cause unwanted spectral products as diodes are non-linear elements.

The future of this field is very likely to result in the integration of several techniques and technologies together to reduce the size resulting in multi-band multi-purpose antennas and scattering surfaces.

Currently, the research community is starting to take a particular interest in large reflective intelligent surfaces (RIS) that should enhance the performance of wireless systems. Unfortunately, there are several factors that can make implementation difficult in practice. For instance, if we consider a large RIS placed on an exterior layer of a building, it is likely that users will be in the near-field region where the field strength varies with distance. The unit cells of such a metasurface

will have different effective areas and angle-dependent responses. These effects will need to be dynamically compensated based on the location of the user. Furthermore, the surrounding environment can also change dynamically for instance due to traffic or moving users. Considering that such surfaces can be highly directive and produce a large number of beams, many variables have to be taken into account to produce the optimal setting of the reflective surface. Moreover, an accurate description of the fields in such an environment might not be available and due to the fact that every environment is different, in the author's opinion, some kind of self-learning algorithm will be needed to adapt to the area where the RIS is placed. Such a system would require feedback which might make such a solution relatively complex and it will be very interesting to see future developments in this field.

The topic of mmWaves is starting to be very attractive as they provide high-bandwidth capabilities, lower interference levels, and small antenna footprints. Unfortunately, many concepts of antennas and active metasurfaces that work well on L, S, C and X bands might be very expensive and impractical at higher frequencies. Furthermore, the requirements for the active components increase the cost of the final solutions. For that reason, new techniques for metasurface reconfigurability should be investigated.

Last but not least, from an RF perspective, a combination of surface waves and planar antennas based on a holographic technique is a very interesting subject. There are already several publications on the topic but there is still room for further research. Such a solution has the advantage of a reflectarray antenna (low profile and easy manufacturing) in comparison to standard parabolic antennas. What's more, instead of a classical horn antenna used as a feeder placed in front of the antenna, a small probe exciting surface waves across the metasurface is used which leads to a very compact antenna system. Such an antenna, in combination with a reconfigurable surface, could offer a very good solution for services where a simultaneous connection between multiple satellites is required.

References

[1] D. Pujara, S. Chakrabarty, and S. B. Sharma, "Analysis of focal region field of the offset-parabolic reflector for space-borne radiometers," in *2007 IEEE Applied Electromagnetics Conference (AEMC)*, 2007, pp. 1–4.

[2] A. McGovern, "Novel lightweight antenna arrays can reduce satellite launch costs," Online, MIT Lincoln Laboratory, resreport, Jan. 2020. [Online]. Available: https://www.ll.mit.edu/news/novel-lightweight-antenna-arrays-can-reduce-satellite-launch-costs

[3] V. Manohar and Y. Rahmat-Samii, "Design and measurement of low-profile, metal-only, offset parabolic stepped reflector antenna for emerging cubesats," in *2020 IEEE International Symposium on Antennas and Propagation and North American Radio Science Meeting*, 2020, pp. 205–206.

[4] Ansys, "Investigating placement of antennas inside an aircraft fuselage," Jan. 2018. [Online]. Available: https://www.ansys.com/blog/antenna-design-placement-inside-aircraft

[5] A. H. Abdelrahman, P. Nayeri, A. Z. Elsherbeni, and F. Yang, "Design of single-feed multi-beam transmitarray antennas," in *2014 IEEE Antennas and Propagation Society International Symposium (APSURSI)*, 2014, pp. 1264–1265.

[6] I. Kaplan, I. Marinov, A. Gal, V. Peshlov, M. Gachev, V. Boyanov, and B. Marinov, "Electronically beam steerable antennas for broadband satellite communications," in *The 8th European Conference on Antennas and Propagation (EuCAP 2014)*, 2014, pp. 2450–2454.

[7] Z. Yang and K. F. Warnick, "Multiband dual-polarization high-efficiency array feed for ku/reverse-band satellite communications," *IEEE Antennas and Wireless Propagation Letters*, vol. 13, pp. 1325–1328, 2014.

[8] A. A. Bezgin and A. A. Savochkin, "Multiband circular polarization antenna for satellite system argos-3 and gps," in *2019 Antennas Design and Measurement International Conference (ADMInC)*, 2019, pp. 30–32.

[9] L. Catarinucci, S. Guglielmi, R. Colella, and L. Tarricone, "Pattern-reconfigurable antennas and smart wake-up circuits to decrease power consumption in wsn nodes," *IEEE Sensors Journal*, vol. 14, no. 12, pp. 4323–4324, 2014.

[10] T. Chi, S. Li, J. S. Park, and H. Wang, "A multifeed antenna for high-efficiency on-antenna power combining," *IEEE Transactions on Antennas and Propagation*, vol. 65, no. 12, pp. 6937–6951, 2017.

[11] X. Yang, W. Geyi, and H. Sun, "Optimum design of wireless power transmission system using microstrip patch antenna arrays," *IEEE Antennas and Wireless Propagation Letters*, vol. 16, pp. 1824–1827, 2017.

[12] J. Massman, G. Simpson, and T. Steffen, "Low cost additively manufactured antenna array modules," in *2019 IEEE International Symposium on Phased Array System Technology (PAST)*, 2019, pp. 1–4.

[13] H. Xia, J. Hu, L. Li, F.-C. Zheng, and T. Zhang, "Low-cost dual-polarized 60 ghz patch antenna array in pcb process," in *2019 IEEE International Symposium on Antennas and Propagation and USNC-URSI Radio Science Meeting*, 2019, pp. 1873–1874.

[14] B. A. MUNK, *Frequency Selective Surfaces*. John Wiley and Sons, Ltd, 2000.

[15] F. Capolino, Ed., *Theory and Phenomena of Metamaterials*. CRC Press, 2009.

[16] "Voyager 1," NASA Science, Solar System Exploration, Aug. 2021. [Online]. Available: https://solarsystem.nasa.gov/missions/voyager-1/in-depth/

[17] "Voyager 2," NASA Science, Solar System Exploration, Aug. 2021. [Online]. Available: https://solarsystem.nasa.gov/missions/voyager-2/in-depth/

[18] R. Ludwig and J. Taylor, *Voyager Telecommunications*. NASA/JPL, 2002. [Online]. Available: https://descanso.jpl.nasa.gov/DPSummary/Descanso4--Voyager_new.pdf

[19] G. Hickey and T.-K. Wu, "Four-frequency selective surface spacecraft subreflector antenna," *Microwave Journal*, vol. 39, pp. 240–252, 05 1996.

[20] H. Wang, Y. Zhao, K. Huang, T. Liu, and P. Gao, "Design of a high-performance radome for satellite communication phased array antennas," in *2018 International Applied Computational Electromagnetics Society Symposium - China (ACES)*, 2018, pp. 1–2.

[21] R. U. Nair and R. M. Jha, "Electromagnetic design and performance analysis of airborne radomes: Trends and perspectives [antenna applications corner]," *IEEE Antennas and Propagation Magazine*, vol. 56, no. 4, pp. 276–298, 2014.

[22] M. A. Sufian, N. Hussain, H. Askari, S. G. Park, K. S. Shin, and N. Kim, "Isolation enhancement of a metasurface-based mimo antenna using slots and shorting pins," *IEEE Access*, vol. 9, pp. 73 533–73 543, 2021.

[23] T. A. Derzhavskaya, S. B. Glybovski, I. V. Melchakova, A. J. E. Raaijmakers, and C. A. T. van den Berg, "Electromagnetic bandgap metasurfaces for decoupling of elements of mri body coil array at 7 tesla," in *2015 Days on Diffraction (DD)*, 2015, pp. 1–6.

[24] B. Ratni, A. de Lustrac, G.-P. Piau, and S. N. Burokur, "Active metasurface for a reconfigurable reflectarray antenna," in *2017 IEEE International Symposium on Antennas and Propagation USNC/URSI National Radio Science Meeting*, 2017, pp. 2071–2072.

[25] F.-C. Tsai and M. Bialkowski, "Designing a 161-element ku-band microstrip reflectarray of variable size patches using an equivalent unit cell waveguide approach," *IEEE Transactions on Antennas and Propagation*, vol. 51, no. 10, pp. 2953–2962, 2003.

[26] T. Niu, W. Withayachumnankul, B. S.-Y. Ung, H. Menekse, M. Bhaskaran, S. Sriram, and C. Fumeaux, "Experimental demonstration of reflectarray antennas at terahertz frequencies," *Opt. Express*, vol. 21, no. 3, pp. 2875–2889, Feb 2013. [Online]. Available: http://www.opticsexpress.org/abstract.cfm?URI=oe-21-3-2875

[27] X. Zhang, F. Yang, S. Xu, A. Aziz, and M. Li, "Hybrid polarization-phase tuning methodology for reflectarray antennas," *IEEE Transactions on Antennas and Propagation*, vol. 69, no. 9, pp. 5534–5545, 2021.

[28] "Smart design of flat 'reflectarray' satellite antennas," The European Space Agency, Tech. Rep., 2020. [Online]. Available: https://www.esa.int/Enabling_Support/Space_Engineering_Technology/Smart_design_of_flat_reflectarray_satellite_antennas

[29] J. C. Batchelor, E. Parker, B. Sanz-Izquierdo, J.-B. Robertson, I. Ekpo, and A. Williamson, "Designing fss for wireless propagation control within buildings," in *2009 Loughborough Antennas Propagation Conference*, 2009, pp. 14–17.

[30] G. I. Kiani, K. L. Ford, L. G. Olsson, K. P. Esselle, and C. J. Panagamuwa, "Switchable frequency selective surface for reconfigurable electromagnetic architecture of buildings," *IEEE Transactions on Antennas and Propagation*, vol. 58, no. 2, pp. 581–584, 2010.

[31] S. Habib, G. I. Kiani, and M. F. U. Butt, "Interference mitigation and wlan efficiency in modern buildings using energy saving techniques and fss," in *2016 IEEE International Symposium on Antennas and Propagation (APSURSI)*, 2016, pp. 965–966.

[32] E. Ekudden, "Exponential capability growth. exponential potential," Ericsson, Tech. Rep., Oct. 2021. [Online]. Available: https://www.ericsson.com/en/blog/2021/10/exponential-capability-growth-exponential-potential

[33] M. Agiwal, A. Roy, and N. Saxena, "Next generation 5g wireless networks: A comprehensive survey," *IEEE Communications Surveys Tutorials*, vol. 18, no. 3, pp. 1617–1655, 2016.

[34] T. S. Andjamba, G.-A. L. Zodi, and D. S. Jat, "Interference analysis of ieee 802.11 wireless networks: A case study of namibia university of science and technology," in *2016 International Conference on ICT in Business Industry Government (ICTBIG)*, 2016, pp. 1–5.

[35] P. C. Shahare and N. A. Chavhan, "An approach to secure sink node's location privacy in wireless sensor networks," in *2014 Fourth International Conference on Communication Systems and Network Technologies*, 2014, pp. 748–751.

[36] D. Zhao, Z. Yan, M. Wang, P. Zhang, and B. Song, "Is 5g handover secure and private? a survey," *IEEE Internet of Things Journal*, vol. 8, no. 16, pp. 12 855–12 879, 2021.

[37] G. Kiani, A. Weily, and K. Esselle, "A novel absorb/transmit fss for secure indoor wireless networks with reduced multipath fading," *IEEE Microwave and Wireless Components Letters*, vol. 16, no. 6, pp. 378–380, 2006.

[38] M. Khan and B. R. Dutta, "A square loop frequency selective surface for designing secure electromagnetic buildings," in *2016 International Conference on Micro-Electronics and Telecommunication Engineering (ICMETE)*, 2016, pp. 23–27.

[39] J. Roberts, K. L. Ford, and J. M. Rigelsford, "Secure electromagnetic buildings," in *The 8th European Conference on Antennas and Propagation (EuCAP 2014)*, 2014, pp. 797–798.

[40] H. Chen, H. Chen, X. Xiu, Q. Xue, and W. Che, "Transparent fss on glass window for signal selection of 5g millimeter wave communication," *IEEE Antennas and Wireless Propagation Letters*, pp. 1–1, 2021.

[41] M. Gustafsson, A. Karlsson, A. Rebelo, and B. Widenberg, "Design of frequency selective windows for improved indoor outdoor communication," *IEEE Transactions on Antennas and Propagation*, vol. 54, no. 6, pp. 1897–1900, 2006.

[42] A. Kazemzadeh and A. Karlsson, "Multilayered wideband absorbers for oblique angle of incidence," *Antennas and Propagation, IEEE Transactions on*, vol. 58, pp. 3637 – 3646, 12 2010.

[43] L. Sun, H. Cheng, Y. Zhou, and J. Wang, "Broadband metamaterial absorber based on coupling resistive frequency selective surface," *Opt. Express*, vol. 20, no. 4, pp. 4675–4680, Feb 2012. [Online]. Available: http://www.osapublishing.org/oe/abstract.cfm?URI=oe-20-4-4675

[44] F. E. Salem, A. Tall, Z. Altman, and A. Gati, "Energy consumption optimization in 5g networks using multilevel beamforming and large scale antenna systems," in *2016 IEEE Wireless Communications and Networking Conference*, 2016, pp. 1–6.

[45] R. Scharstein, "Visualization and interpretation for the electromagnetic derivation of snell's laws," *IEEE Transactions on Education*, vol. 41, no. 4, pp. 286–292, 1998.

[46] R. Haupt and M. Cote, "Snell's law applied to finite surfaces," *IEEE Transactions on Antennas and Propagation*, vol. 41, no. 2, pp. 227–230, 1993.

[47] M. Pehlıvan, K. Yeğın, and Y. Aşci, "Design of 1–18 ghz parabolic reflector antenna with lpda feed," in *2016 24th Telecommunications Forum (TELFOR)*, 2016, pp. 1–3.

[48] T. İsenlik, E. Başaran, and B. Türetken, "A novel ultra wideband horn feed for parabolic reflector antennas," in *2012 IEEE International Conference on Ultra-Wideband*, 2012, pp. 513–517.

[49] Y. Asci, E. Curuk, K. Yegin, and C. Ozdemir, "Improved splash-plate feed parabolic reflector antenna for ka-band vsat applications," in *2016 46th European Microwave Conference (EuMC)*, 2016, pp. 1283–1286.

[50] S. K. Mustafa and S. Yasir, "Design, development and testing of dielectric tapered rod feed for parabolic reflector antenna as an alternate to feed horns," in *Proceedings of 2013 10th International Bhurban Conference on Applied Sciences Technology (IBCAST)*, 2013, pp. 369–371.

[51] C. M. Muvianto, Pahrurrozi, S. Ariessaputra, and S. Malekpour, "Optimization of grid antenna 2.4 ghz using grid reflector and yagi antenna's feed modification," in *2018 2nd International Conference on Applied Electromagnetic Technology (AEMT)*, 2018, pp. 24–28.

[52] K. Medrar, L. Marnat, L. Dussopt, C. Belem-Goncalves, G. Ducournau, C. Luxey, and F. Gianesello, "H-band substrate-integrated discrete-lens antenna for high data rate communication systems," *IEEE Transactions on Antennas and Propagation*, vol. 69, no. 7, pp. 3677–3688, 2021.

[53] V. Gruev, R. Perkins, and T. York, "Ccd polarization imaging sensor with aluminum nanowire optical filters," *Opt. Express*, vol. 18, no. 18, pp. 19 087–19 094, Aug 2010. [Online]. Available: http://www.osapublishing.org/oe/abstract.cfm?URI=oe-18-18-19087

[54] K. Ito and M.-S. Win, "Various characteristics of a dipole antenna with parallel-wire reflector," in *Antennas and Propagation Society Symposium 1991 Digest*, 1991, pp. 1844–1847 vol.3.

[55] L. Li, J. Wang, M. Feng, H. Du, H. Ma, J. Wang, J. Zhang, and S. Qu, "All-dielectric frequency selective surface based on 3d printing materials," *Physica status solidi (a)*, vol. 215, no. 14, p. 1700840, 2018. [Online]. Available: https://onlinelibrary.wiley.com/doi/abs/10.1002/pssa.201700840

[56] M. Bozzi, M. Montagna, and L. Perregrini, "Modeling of capacitive fss with thick metal patches by the mom/bi-rme method," in *The 40th European Microwave Conference*, 2010, pp. 589–592.

[57] M. Pasian, M. Bozzi, and L. Perregrini, "Design of a large bandwidth planar antenna using inductive frequency selective surfaces," in *The Second European Conference on Antennas and Propagation, EuCAP 2007*, 2007, pp. 1–5.

[58] M. Bozzi, G. Manara, A. Monorchio, and L. Perregrini, "Automatic design of inductive fsss using the genetic algorithm and the mom/bi-rme analysis," *IEEE Antennas and Wireless Propagation Letters*, vol. 1, pp. 91–93, 2002.

[59] M. Z. A. A. Aziz, M. M. Shukor, B. H. Ahmad, M. K. Suaidi, M. F. Johar, M. A. Othman, S. Salleh, F. A. Azmin, and M. F. A. Malek, "Investigation of a square loop frequency selective surface (fss) on hybrid material at 2.4 ghz," in *2013 IEEE International Conference on Control System, Computing and Engineering*, 2013, pp. 275–278.

[60] P. Mahima, B. Sangeetha, S. Narayan, and R. U. Nair, "Em design of hybrid-element fss structure for radome application," in *2016 IEEE Annual India Conference (INDICON)*, 2016, pp. 1–4.

[61] J. Sreeja, P. Mahima, and S. Narayan, "Em design of miniaturized fss based low observable antenna for aerospace application," in *2019 TEQIP III Sponsored International Conference on Microwave Integrated Circuits, Photonics and Wireless Networks (IMICPW)*, 2019, pp. 163–166.

[62] R. Nair, A. Neelam, and R. Jha, "A novel jerusalem cross fss embedded a-sandwich radome for aerospace applications," in *2009 Applied Electromagnetics Conference (AEMC)*, 2009, pp. 1–4.

[63] A. Ramezani Varkani, Z. Hossein Firouzeh, and A. Zeidaabadi Nezhad, "Equivalent circuit model for array of circular loop fss structures at oblique angles of incidence," *IET Microwaves, Antennas & Propagation*, vol. 12, no. 5, pp. 749–755, 2018. [Online]. Available: https://ietresearch.onlinelibrary.wiley.com/doi/abs/10.1049/iet-map.2017.1004

[64] W. Mohyuddin, D. H. Kim, H. C. Choi, and K. W. Kim, "Comparative study of square and circular loop frequency selective surfaces for millimeter-wave imaging diagnostics systems," *Sensors*, vol. 18, no. 9, 2018. [Online]. Available: https://www.mdpi.com/1424-8220/18/9/3079

[65] R.-Q. Sun, J. Xie, and Y.-W. Zhang, "Simulation research of band-pass frequency selective surfaces (fss) radome," in *2016 Progress in Electromagnetic Research Symposium (PIERS)*, 2016, pp. 1186–1193.

[66] M. Ying, R. Kuse, T. Hori, M. Fujimoto, T. Seki, K. Sato, and I. Oshima, "Unit cell structure of amc with multi-layer patch type fss for miniaturization," *2013 Proceedings of the International Symposium on Antennas & Propagation*, vol. 02, pp. 957–960, 2013.

[67] D. Lockyer, J. Vardaxoglou, and R. Simpkin, "Complementary frequency selective surfaces," *Microwaves, Antennas and Propagation, IEE Proceedings* -, vol. 147, pp. 501 – 507, 01 2001.

[68] V. Krushna Kanth and S. Raghavan, "Equivalent circuit analysis of complementary fss for selective em shielding," in *2018 15th International Conference on ElectroMagnetic Interference Compatibility (INCEMIC)*, 2018, pp. 1–4.

[69] B. S. da Silva, A. L. P. S. Campos, and A. Gomes Neto, "Narrowband shielding against electromagnetic interference in lte 4g systems using complementary frequency selective surfaces," *Microwave and Optical Technology Letters*, vol. 60, no. 9, pp. 2293–2298, 2018. [Online]. Available: https://onlinelibrary.wiley.com/doi/abs/10.1002/mop.31341

[70] G. Sung, K. Sowerby, and A. Williamson, "The impact of frequency selective surfaces applied to standard wall construction materials," in *IEEE Antennas and Propagation Society Symposium, 2004.*, vol. 2, 2004, pp. 2187–2190 Vol.2.

[71] M. Raspopoulos and S. Stavrou, "Frequency selective surfaces on building materials – air gap impact," *Electronics Letters*, vol. 43, pp. 700–702(2), June 2007. [Online]. Available: https://digital-library.theiet.org/content/journals/10.1049/el_20071126

[72] ——, "Frequency selective buildings through frequency selective surfaces," *IEEE Transactions on Antennas and Propagation*, vol. 59, no. 8, pp. 2998–3005, 2011.

[73] M. Raspopoulos, F. A. Chaudhry, and S. Stavrou, "Radio propagation in frequency selective buildings," *European Transactions on Telecommunications*, vol. 17, no. 3, pp. 407–413, 2006. [Online]. Available: https://onlinelibrary.wiley.com/doi/abs/10.1002/ett.1127

[74] T.-K. Wu, *Frequency Selective Surfaces*, 04 2005.

[75] M. Philippakis, C. Martel, and D. Kemp, "Application of fss structures to selectively control the propagation of signals into and out of buildings

annex 4: In-building propagation enhancement," Mar. 2004. [Online]. Available: https://www.ofcom.org.uk/__data/assets/pdf_file/0021/32079/in_building.pdf

[76] N. Ishak, M. H. Dahri, M. R. Kamarudin, F. C. Seman, N. A. Awang, C. Soon, and N. Zainal, "Performance comparison between different structures of fss in terms of angular stability," in *2020 IEEE International RF and Microwave Conference (RFM)*, 2020, pp. 1–4.

[77] D. Sánchez-Escuderos, M. Ferrando-Rocher, J. I. Herranz-Herruzo, and A. Valero-Nogueira, "Grating lobes reduction using a multilayer frequency selective surface on a dual-polarized aperture array antenna in ka-band," *IEEE Access*, vol. 8, pp. 104 977–104 984, 2020.

[78] S. M. A. Momeni Hasan Abadi and N. Behdad, "Design of wideband, fss-based multibeam antennas using the effective medium approach," *IEEE Transactions on Antennas and Propagation*, vol. 62, pp. 5557–5564, 11 2014.

[79] A. Cucini, M. Caiazzo, P. Bennati, and S. Maci, "Quasi-tem waveguides realized by fss-walls," in *IEEE Antennas and Propagation Society Symposium, 2004.*, vol. 1, 2004, pp. 807–810 Vol.1.

[80] R. Pierre, G. Tayeb, B. Gralak, and S. Enoch, "Quasi-tem modes in rectangular waveguides: a study based on the properties of pmc and hard surfaces," *Journal of Modern Optics*, vol. 56, no. 4, pp. 530–538, 2009. [Online]. Available: https://doi.org/10.1080/09500340802604146

[81] P. A. Soares, P. Pinho, and C. Wuensche, "High performance corrugated horn antennas for cosmogal satellite," *Procedia Technology*, vol. 17, pp. 667–673, 2014, conference on Electronics, Telecommunications and Computers – CETC 2013. [Online]. Available: https://www.sciencedirect.com/science/article/pii/S2212017314004344

[82] M. K. Emara, J. Hautcoeur, G. Panther, J. S. Wight, and S. Gupta, "Surface impedance engineered low-profile dual-band grooved-dielectric choke ring for gnss applications," *IEEE Transactions on Antennas and Propagation*, vol. 67, no. 3, pp. 2008–2011, 2019.

[83] E. Taghdisi, S. Ghaffarian, R. Mirzavand, and P. Mousavi, "Compact substrate integrated choke ring ground structure for high-precision gnss applications," in *2020 IEEE International Symposium on Antennas and Propagation and North American Radio Science Meeting*, 2020, pp. 1705–1706.

[84] M. K. Emara, K. Madhoun, R. Madhoun, and S. Gupta, "A low-cost lightweight 3d-printed choke ring for multipath mitigation for gnss antennas," in *2019 IEEE International Symposium on Antennas and Propagation and USNC-URSI Radio Science Meeting*, 2019, pp. 721–722.

[85] O. Luukkonen, M. G. Silveirinha, A. B. Yakovlev, C. R. Simovski, I. S. Nefedov, and S. A. Tretyakov, "Effects of spatial dispersion on reflection from mushroom-type artificial impedance surfaces," *IEEE Transactions on Microwave Theory and Techniques*, vol. 57, no. 11, pp. 2692–2699, 2009.

[86] D. Sievenpiper, L. Zhang, R. Broas, N. Alexopolous, and E. Yablonovitch, "High-impedance electromagnetic surfaces with a forbidden frequency band," *IEEE Transactions on Microwave Theory and Techniques*, vol. 47, no. 11, pp. 2059–2074, 1999.

[87] E. R. Gafarov and Y. P. Salomatov, "Hexagonal fss for glonass/gps antenna with improved axial ratio," in *2011 International Siberian Conference on Control and Communications (SIBCON)*, 2011, pp. 159–161.

[88] B. H. Fong, J. S. Colburn, J. J. Ottusch, J. L. Visher, and D. F. Sievenpiper, "Scalar and tensor holographic artificial impedance surfaces," *IEEE Transactions on Antennas and Propagation*, vol. 58, no. 10, pp. 3212–3221, 2010.

[89] D. Sievenpiper, J. Colburn, B. Fong, J. Ottusch, and J. Visher, "Holographic artificial impedance surfaces for conformal antennas," in *2005 IEEE Antennas and Propagation Society International Symposium*, vol. 1B, 2005, pp. 256–259 vol. 1B.

[90] A. Bellion and M. Cable, "A new wideband and compact high impedance surface," in *2012 15 International Symposium on Antenna Technology and Applied Electromagnetics*, 2012, pp. 1–5.

[91] Z. N. Chen, W. Liu, and X. Qing, "Low-profile broadband mushroom and metasurface antennas," in *2017 International Workshop on Antenna Technology: Small Antennas, Innovative Structures, and Applications (iWAT)*, 2017, pp. 13–16.

[92] F. Costa, O. Luukkonen, C. R. Simovski, A. Monorchio, S. A. Tretyakov, and P. M. de Maagt, "Te surface wave resonances on high-impedance surface based antennas: Analysis and modeling," *IEEE Transactions on Antennas and Propagation*, vol. 59, no. 10, pp. 3588–3596, 2011.

[93] H. Ayad, M. Fadlallah, H. Youssef, H. Elmokdad, F. Ndagijimana, and J. Jomaah, "Performances of low profile dipole antenna amc-based surface using metamaterials structures," in *2012 19th International Conference on Telecommunications (ICT)*, 2012, pp. 1–5.

[94] X. Dang, M. Li, F. Yang, and S. Xu, "Quasi-periodic array modeling using reduced basis from elemental array," in *2017 IEEE International Conference on Computational Electromagnetics (ICCEM)*, 2017, pp. 49–51.

[95] K. Achouri, M. A. Salem, and C. Caloz, "General metasurface synthesis based on susceptibility tensors," *IEEE Transactions on Antennas and Propagation*, vol. 63, no. 7, pp. 2977–2991, 2015.

[96] K. L. Ford and K. Shah, "A study on the use of metasurface synthesis using electric and magnetic susceptibility," in *2016 Loughborough Antennas Propagation Conference (LAPC)*, 2016, pp. 1–4.

[97] S. Ebadi, T. Driscoll, and D. Smith, "Visual illustrations of microwave holographic beamforming using a modulated surface-impedance metamaterial," in *2013 IEEE Antennas and Propagation Society International Symposium (APSURSI)*, 2013, pp. 2343–2344.

[98] M. Li, X. Dang, T. Liu, F. Yang, S. Xu, and A. Boag, "Modeling and analysis of quasi-periodic arrays," in *2017 International Conference on Electromagnetics in Advanced Applications (ICEAA)*, 2017, pp. 998–1000.

[99] O. Yurduseven, S. D. Assimonis, and M. Matthaiou, "Intelligent reflecting surfaces with spatial modulation: An electromagnetic perspective," *IEEE Open Journal of the Communications Society*, vol. 1, pp. 1256–1266, 2020.

[100] B. Xu, Z. Wei, C. Wu, Y. Fan, Z. Wang, and H. Li, "Near-diffraction-limited focusing with gradient high-impedance metasurface," *Opt. Mater. Express*, vol. 7, no. 4, pp. 1141–1146, Apr 2017. [Online]. Available: http://opg.optica.org/ome/abstract.cfm?URI=ome-7-4-1141

[101] S. Choudhary and K. R. Hiremath, "Random phase gradient metasurface for broadband rcs reduction," in *TENCON 2019 - 2019 IEEE Region 10 Conference (TENCON)*, 2019, pp. 1452–1454.

[102] S. Li, Z. N. Chen, T. Li, F. H. Lin, and X. Yin, "Characterization of metasurface lens antenna for sub-6 ghz dual-polarization full-dimension massive mimo and multibeam systems," *IEEE Transactions on Antennas and Propagation*, vol. 68, no. 3, pp. 1366–1377, 2020.

[103] K. Liu and Y. Ge, "A wideband high-gain conical short horn based on a metasurface-corrected lens," in *2019 IEEE International Symposium on Antennas and Propagation and USNC-URSI Radio Science Meeting*, 2019, pp. 619–620.

[104] D. Sievenpiper, J. Schaffner, H. Song, R. Loo, and G. Tangonan, "Two-dimensional beam steering using an electrically tunable impedance surface," *IEEE Transactions on Antennas and Propagation*, vol. 51, no. 10, pp. 2713–2722, 2003.

[105] S. Cho, A. Salim, and H.-J. Song, "Two-dimensional beam steering active lens with simple grid bias lines at 19 ghz," *IEEE Transactions on Vehicular Technology*, vol. 70, no. 10, pp. 9716–9724, 2021.

[106] T.-T. Chia, "Prediction of electromagnetic scattering from metasurfaces," in *2016 10th European Conference on Antennas and Propagation (EuCAP)*, 2016, pp. 1–5.

[107] Y. Liu, X. Liu, X. Mu, T. Hou, J. Xu, M. Di Renzo, and N. Al-Dhahir, "Reconfigurable intelligent surfaces: Principles and opportunities," *IEEE Communications Surveys Tutorials*, vol. 23, no. 3, pp. 1546–1577, 2021.

[108] M. Di Renzo, A. Zappone, M. Debbah, M.-S. Alouini, C. Yuen, J. de Rosny, and S. Tretyakov, "Smart radio environments empowered by reconfigurable intelligent surfaces: How it works, state of research, and the road ahead," *IEEE Journal on Selected Areas in Communications*, vol. 38, no. 11, pp. 2450–2525, 2020.

[109] M. M. W. Z. J. L. Wenxuan Long, Rui Chen, "A promising technology for 6g wireless networks: Intelligent refl ecting surface," *Journal of Communications and Information Networks*, vol. 6, no. 1, p. 1, 2021. [Online]. Available: http://www.infocomm-journal.com/jcin/EN/abstract/article_171197.shtml

[110] X. Wang and G.-M. Yang, "Time-coding spread-spectrum reconfigurable intelligent surface for secure wireless communication: theory and experiment," *Opt. Express*, vol. 29, no. 20, pp. 32 031–32 041, Sep 2021. [Online]. Available: http://www.osapublishing.org/oe/abstract.cfm?URI=oe-29-20-32031

[111] M. Saikia, S. Ghosh, S. Bhattacharyya, and K. V. Srivastava, "Broadband polarization rotator using multilayered metasurfaces," in *2015 IEEE Applied Electromagnetics Conference (AEMC)*, 2015, pp. 1–2.

[112] M. Saikia, S. Ghosh, S. K. Sharma, and K. V. Srivastava, "A broadband transmission polarization rotator using multi layer split rings," in *2016 IEEE Uttar Pradesh Section International Conference on Electrical, Computer and Electronics Engineering (UPCON)*, 2016, pp. 179–182.

[113] Y. Li, Q. Cao, and Y. Wang, "A wideband multifunctional multilayer switchable linear polarization metasurface," *IEEE Antennas and Wireless Propagation Letters*, vol. 17, no. 7, pp. 1314–1318, 2018.

[114] F. Zhang, G.-M. Yang, and Y.-Q. Jin, "Microwave polarization converter with multilayer metasurface," in *2020 14th European Conference on Antennas and Propagation (EuCAP)*, 2020, pp. 1–4.

[115] Z. Wu, Y. Ra'di, and A. Grbic, "A tunable polarization rotator based on metasurfaces," in *2017 11th European Conference on Antennas and Propagation (EUCAP)*, 2017, pp. 728–730.

[116] ——, "Tunable metasurfaces: A polarization rotator design," *Phys. Rev. X*, vol. 9, p. 011036, Feb 2019. [Online]. Available: https://link.aps.org/doi/10.1103/PhysRevX.9.011036

[117] X. Yang, T. Qi, Y. Zeng, X. Liu, G. Lu, and Q. Cai, "Broadband reflective polarization rotator built on single substrate," *Electronics*, vol. 10, no. 8, 2021. [Online]. Available: https://www.mdpi.com/2079-9292/10/8/916

[118] K.-k. Xu, Z.-y. Xiao, and J.-y. Tang, "Linearly polarized converters for reflected and transmitted waves based on double-split ring resonator," *Plasmonics (Norwell, Mass.)*, vol. 12, no. 6, pp. 1869–1874, 2016.

[119] Meraj-E-Mustafa and F. A. Tahir, "A broadband metasurface for cross polarization conversion applications," in *2019 IEEE International Conference on Computational Electromagnetics (ICCEM)*, 2019, pp. 1–2.

[120] Meraj-E-Mustafa, R. Izhar, M. S. Wahidi, F. A. Tahir, and Q. H. Abbasi, "A broadband 90° polarization rotator metasurface," in *2019 IEEE International Conference on Computational Electromagnetics (ICCEM)*, 2019, pp. 1–2.

[121] M. I. Khan, Y. Chen, B. Hu, N. Ullah, S. H. R. Bukhari, and S. Iqbal, "Multiband linear and circular polarization rotating metasurface based on multiple plasmonic resonances for c, x and k band applications," *Scientific reports*, vol. 10, no. 1, pp. 17 981–17 981, 2020.

[122] M. S. Salman, M. I. Khan, F. A. Tahir, and H. Rmili, "Multifunctional single layer metasurface based on hexagonal split ring resonator," *IEEE access*, vol. 8, pp. 28 054–28 063, 2020.

[123] J. Xu, R. Li, J. Qin, S. Wang, and T. Han, "Ultra-broadband wide-angle linear polarization converter based on h-shaped metasurface," *Opt. Express*, vol. 26, no. 16, pp. 20 913–20 919, Aug 2018. [Online]. Available: http://opg.optica.org/oe/abstract.cfm?URI=oe-26-16-20913

[124] Y. Jia, Y. Liu, W. Zhang, and S. Gong, "Ultra-wideband and high-efficiency polarization rotator based on metasurface," *Applied Physics Letters*, vol. 109, no. 5, p. 051901, 2016. [Online]. Available: https://doi.org/10.1063/1.4960355

[125] M. Saikia, S. Ghosh, and K. V. Srivastava, "Switchable reflective metamaterial polarisation rotator," *Electronics Letters*, vol. 52, pp. 1030–1032, 06 2016.

[126] W. Yang, D. Chen, W. Che, and W. Feng, "Multi-functional antennas using polarization-rotation artificial magnetic conductor structures," in *2017 10th Global Symposium on Millimeter-Waves*, 2017, pp. 11–14.

[127] M. Ghebrebrhan, F. Aranda, G. Walsh, D. Ziegler, S. Giardini, J. Carlson, B. Kimball, D. Steeves, Z. Xia, S. Yu, E. Kingsley, R. Nagarajan, J. Torcedo, R. Williams, and A. Gatesman, "Textile frequency selective surface," *IEEE Microwave and Wireless Components Letters*, vol. 27, no. 11, pp. 989–991, 2017.

[128] R. Seager, A. Chauraya, J. Bowman, M. Broughton, R. Philpott, and N. Nimkulrat, "Fabric based frequency selective surfaces using weaving and screen printing," *Electronics Letters*, vol. 49, no. 24, pp. 1507–1509, 2013. [Online]. Available: https://ietresearch.onlinelibrary.wiley.com/doi/abs/10.1049/el.2013.2314

[129] A. Tennant, W. Hurley, and T. Dias, "Experimental knitted, textile frequency selective surfaces," *Electronics Letters*, vol. 48, pp. 1386–1388(2), October 2012. [Online]. Available: https://digital-library.theiet.org/content/journals/10.1049/el.2012.3005

[130] P. Gurrala, S. Oren, P. Liu, J. Song, and L. Dong, "Fully conformal square-patch frequency-selective surface toward wearable electromagnetic shielding," *IEEE Antennas and Wireless Propagation Letters*, vol. 16, pp. 2602–2605, 2017.

[131] D. He, Q. Yu, Y. Chen, and S. Yang, "Dual-band shared-aperture base station antenna array with electromagnetic transparent antenna elements," *IEEE Transactions on Antennas and Propagation*, vol. 69, no. 9, pp. 5596–5606, 2021.

[132] S. Baek, M. Balk, K. Kim, H. Kim, and J. Choi, "Unique multi-physics approach of self phase locked magnetron (splm) system with cst studio suite™," in *2013 IEEE 14th International Vacuum Electronics Conference (IVEC)*, 2013, pp. 1–3.

[133] A. H. Abdelgwad and T. M. Said, "Measured dielectric permittivity of chlorinated drinking water in the microwave frequency range," in *2015 IEEE 15th Mediterranean Microwave Symposium (MMS)*, 2015, pp. 1–4.

[134] J. M. Rigelsford and M. Cerveny, "A simplification technique for s-parameter calculations within partially loaded resonant cavities," in *2016 Progress in Electromagnetic Research Symposium (PIERS)*, 2016, pp. 4673–4674.

[135] M. Cerveny and P. Hazdra, "Evaluation of the input impedance and impedance quality factor of a dipole in spatial and spectral domains," *Radioengineering*, vol. 26, no. 4, pp. 968–971, 2017.

[136] MATLAB. Natick, Massachusetts: The MathWorks Inc.

[137] M. Cerveny, K. L. Ford, and A. Tennant, "Metasurface synthesis using susceptibility tensors and holographic technique," in *Loughborough Antennas Propagation Conference (LAPC 2017)*, 2017, pp. 1–4.

[138] J. M. Rigelsford, K. Ford., M. Cerveny, and sixteen more authors., "Wireless friendly and energy efficient buildings (wifeeb)," 07 2015, p. 1674.

[139] M. Cerveny, J. M. Rigelsford, and R. J. Langley, "A sparse fss for control of radio coverage in buildings," in *2016 IEEE International Symposium on Antennas and Propagation (APSURSI)*, 2016, pp. 1449–1450.

[140] M. Cerveny and J. M. Rigelsford, "An inductive frequency selective surface for use in secure facilities," in *2015 Loughborough Antennas Propagation Conference (LAPC)*, 2015, pp. 1–4.

[141] M. Cerveny, K. L. Ford, and A. Tennant, "Study of printed scattering reflectors based on discretised metasurface," in *2020 14th European Conference on Antennas and Propagation (EuCAP)*, 2020, pp. 1–5.

[142] ——, "Reflective switchable polarization rotator based on metasurface with pin diodes," *IEEE Transactions on Antennas and Propagation*, vol. 69, no. 3, pp. 1483–1492, 2021.

[143] M. Cerveny and P. Hazdra, "Gnss sector antenna for interference mitigation and localization using a high-impedance reflector," *IEEE Antennas and Wireless Propagation Letters*, vol. 19, no. 10, pp. 1674–1678, 2020.

[144] W. L. Stutzman and G. A. Thiele, *Antenna Theory and Design third edition.* Jon Wiley and Sons, Inc., 2013, page 198.

[145] S. Srikanth and G. Behrens, "A new broadband short-backfire antenna as a prime focus feed single and dual band," in *2007 IEEE Antennas and Propagation Society International Symposium*, 2007, pp. 3684–3687.

6 Appendices

6.1 A Simplification Technique For S-parameter Calculations within Partially Loaded Resonant Cavities

This section builds on the information presented in the abstract provided (page 17). This work was presented at the Photonics and Electromagnetism Research Symposium (PIERS) 2016 in Shanghai.

Fig. 1 presents the measured cavity of internal dimensions of 1m x 0.2m and the four port antenna configuration placed inside the cavity.

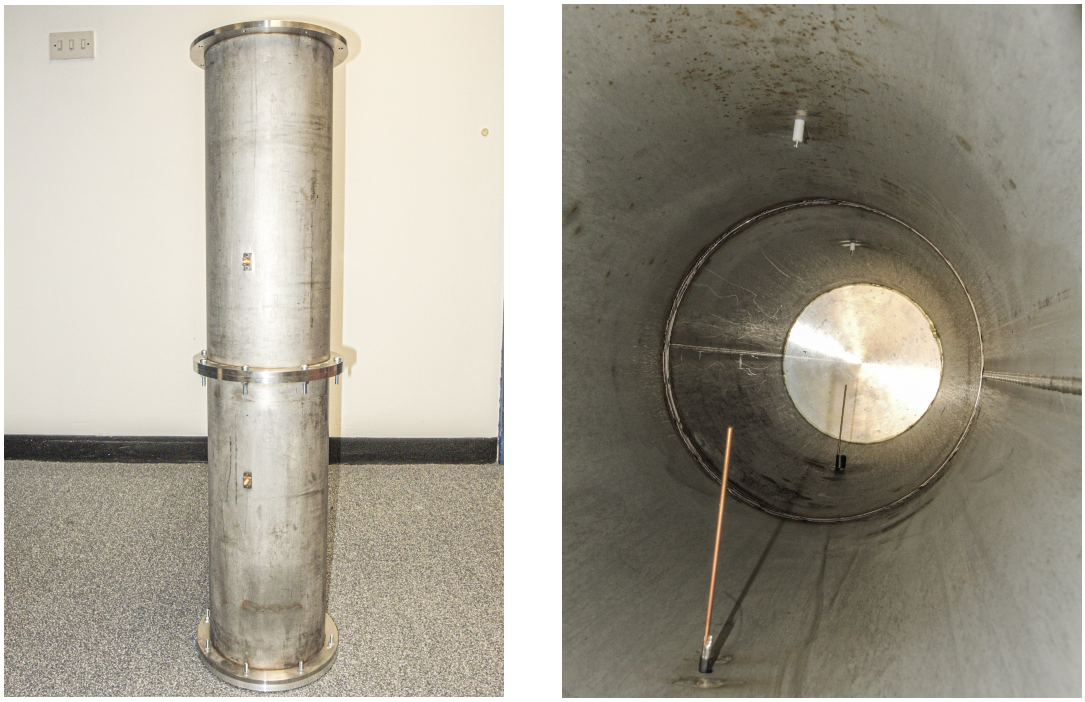

(a) Measured cavity (b) Antenna ports

Figure 1: Measured cavity containing four antenna ports.

Firstly, the cavity was measured when empty, without any water. The measured results of the empty cavity were then compared with electromagnetic simulations using a frequency domain solver (finite element method) implemented in CST Microwave Studio (Fig. 2).

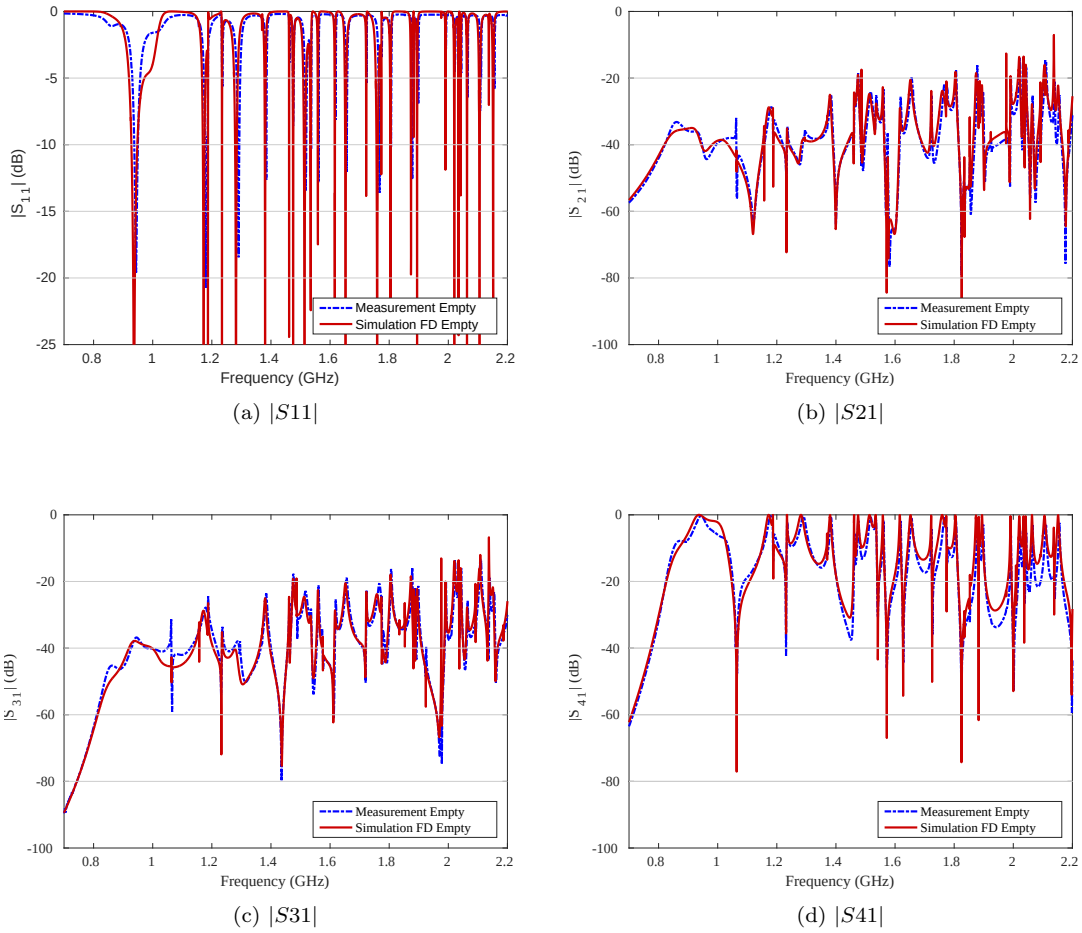

(a) $|S11|$ (b) $|S21|$

(c) $|S31|$ (d) $|S41|$

Figure 2: Simulation and measurement comparison - empty cavity.

After validating the results, the cavity was filled with 100mm and 200mm of water. The corresponding electromagnetic model created in CST Microwave Studio can be seen in Fig. 3.

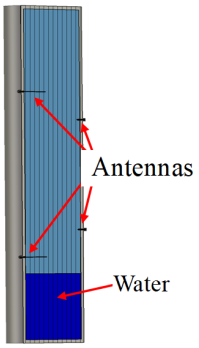

Figure 3: A CST model showing the antennas within the cavity and the water level.

The aim was to reduce the required computing resources of this task. Therefore, the 100 mm and 200mm thick slab of water was replaced by a 55 mm thick

slab of water with an open boundary below the cavity, allowing us to ignore the cavity below this point. To further extend this method, only a thin layer of water (0.1 mm thick) representing the surface of the water above an open boundary was considered (Fig. 4). As already mentioned in the published abstract, this method significantly reduced the resource requirements while the effect on the obtained results is negligible (Fig. 5, Fig. 6).

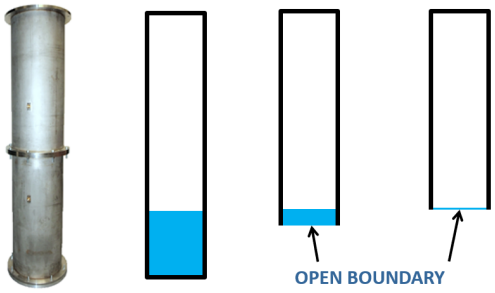

Figure 4: Cavity - method explanation.

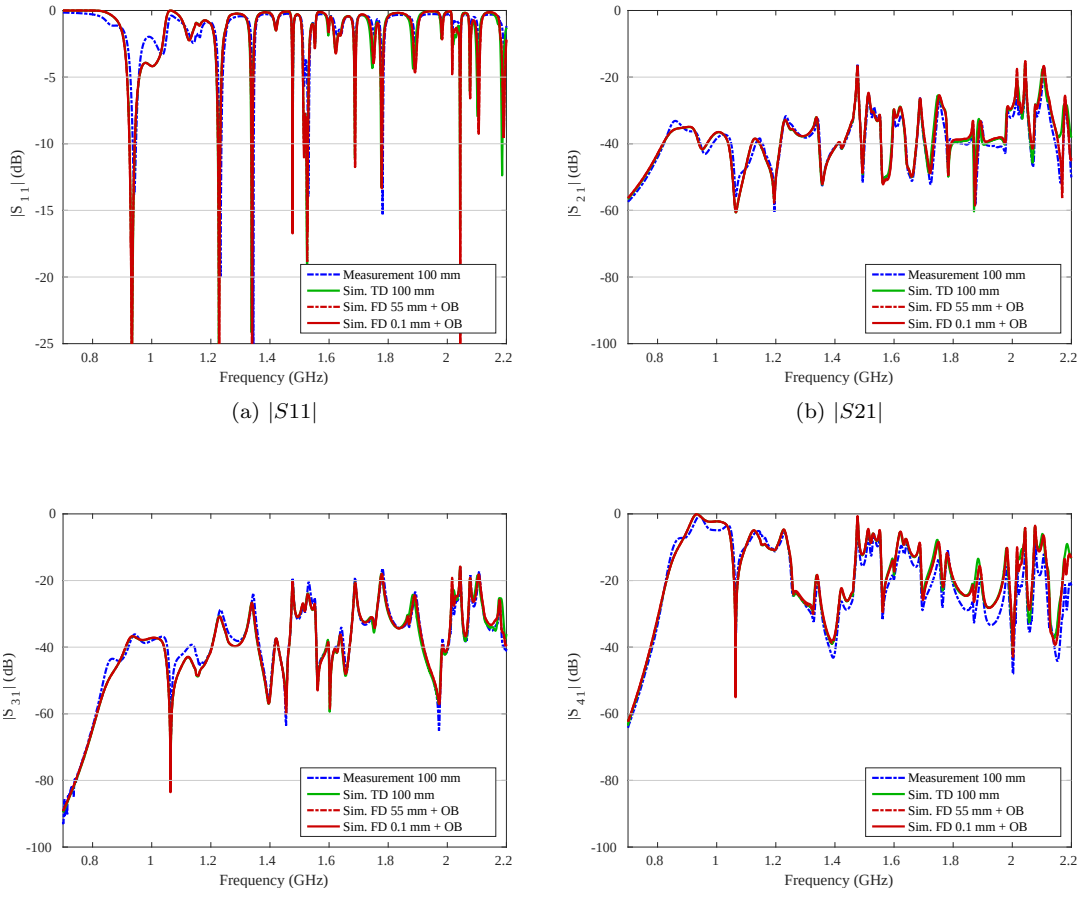

(a) $|S11|$ (b) $|S21|$

(c) $|S31|$ (d) $|S41|$

Figure 5: Simulation and measurement comparison - cavity filled with 100mm of water.

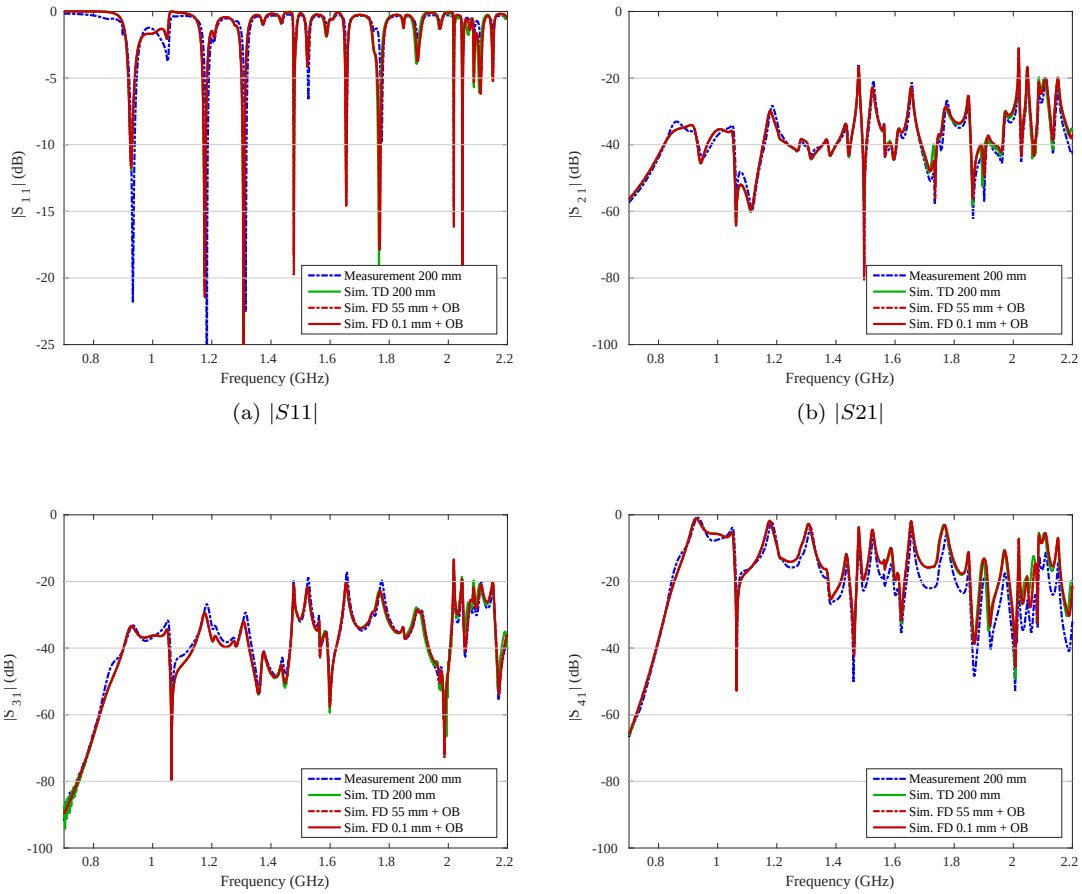

(a) $|S11|$ (b) $|S21|$

(c) $|S31|$ (d) $|S41|$

Figure 6: Simulation and measurement comparison - cavity filled with 200mm of water.

6.2 Wireless Friendly and Energy Efficient Buildings (WiFEEB) project - WiFi propagation in a Victorian House at 2.4GHz

The following work was presented in the WiFEEB report and was financially supported by Marie Curie Industry-Academia Partnerships and Pathways (IAPP) Grant Agreement 286333.

The aim of this measurement was to present the effect of a conductive carpet placed on a floor of a Victorian house on the received signal strength indication (RSSI) of a 2.4GHz WiFi network. Such carpets could be made with a certain frequency response or made active for an active switching of electromagnetic propagation inside buildings. When such material is used for thermal insulation, the effect on the wireless networks inside the building might be significant.

Firstly, the Victorian house studied had to be measured and floor plans had to be created as shown in Fig. 7.

Figure 7: Floor plans - ground floor (on the left), first floor (in the middle), second floor (on the right).

Furthermore, a Matlab code importing the floor plans, recording RSSI values and corresponding positions was written (Fig. 8).

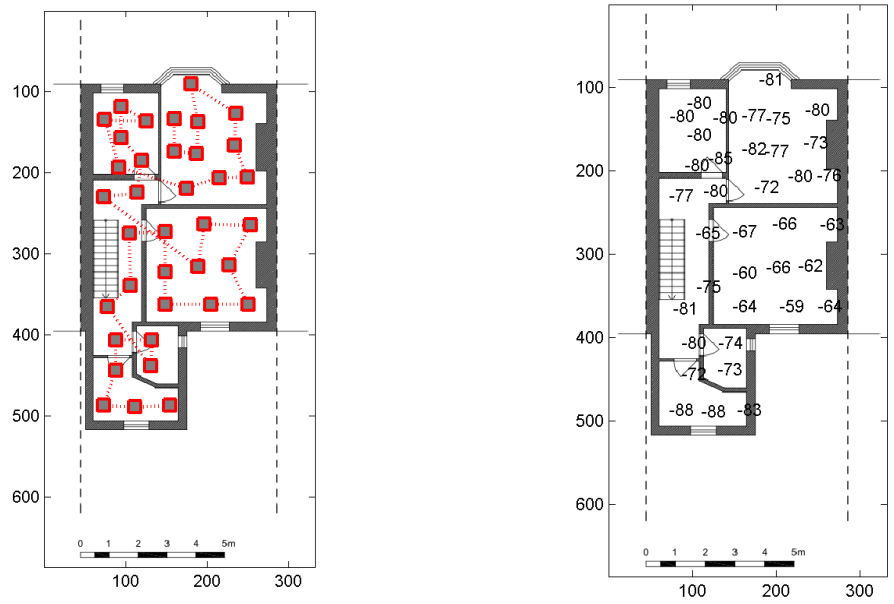

(a) Locations of the measurement

(b) Corresponding RSII values

Figure 8: First floor - RSSI measurement.

Then one room on the first floor was covered with a conductive insulation foil (Fig. 9) and the measurements were performed again (Fig. 10).

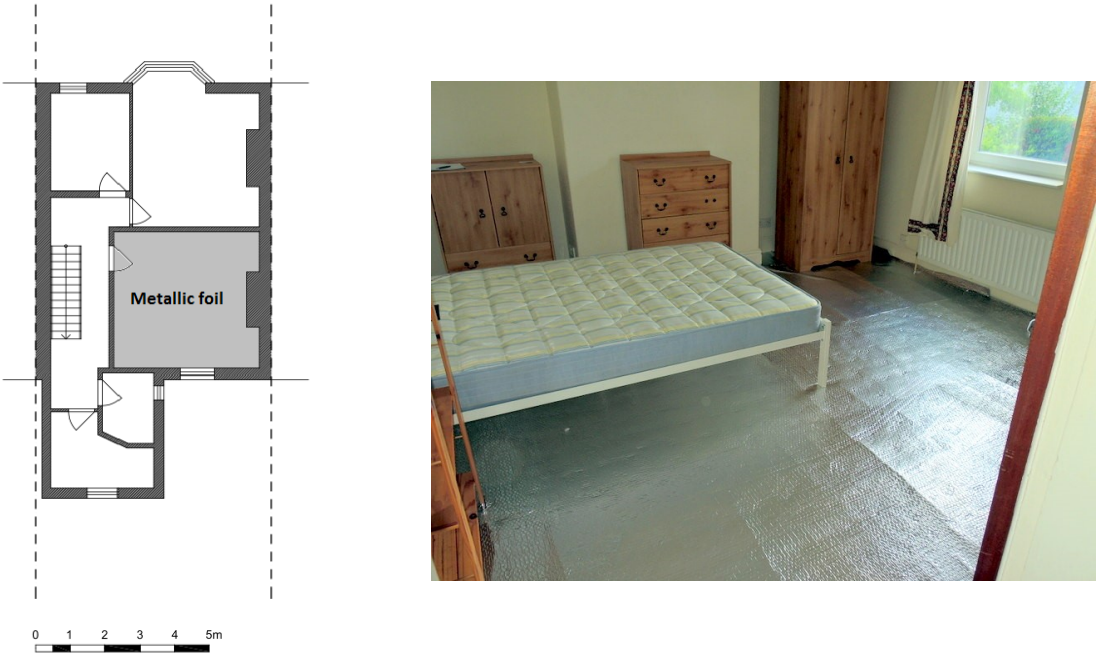

Figure 9: A metallic foil covers floor of a room on the first floor.

(a) Location of the measurement

(b) Corresponding RSII values

Figure 10: First floor - RSSI measurement, one room covered with a metallic foil.

The effect of the metallic foil can be seen in the following heat-maps. The results without the metallic foil are presented on the left hand side, with the foil on the right hand side (Fig. 11, Fig. 12 and Fig. 13).

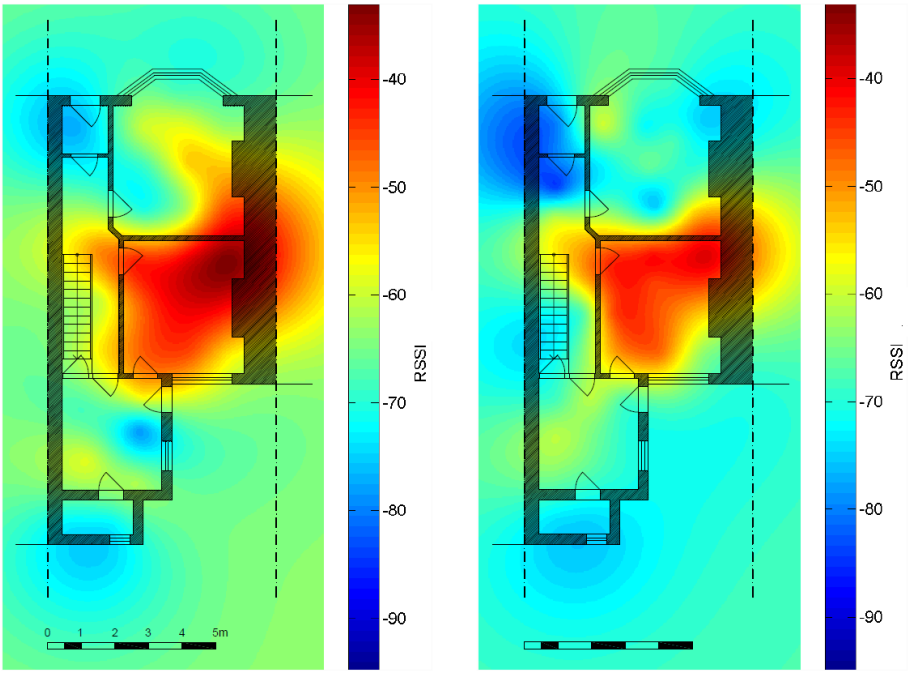

Figure 11: Ground floor.

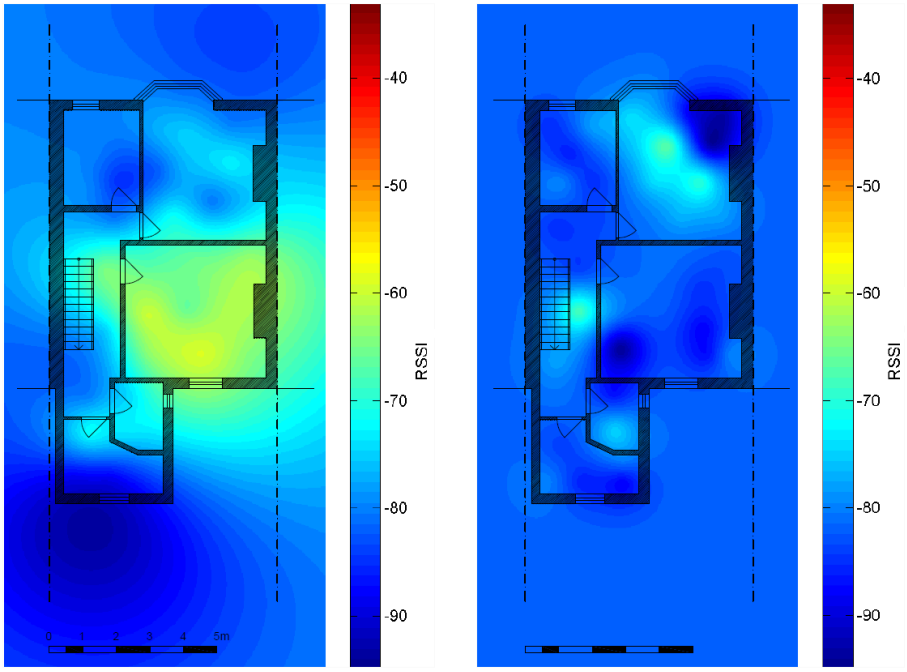

Figure 12: First floor.

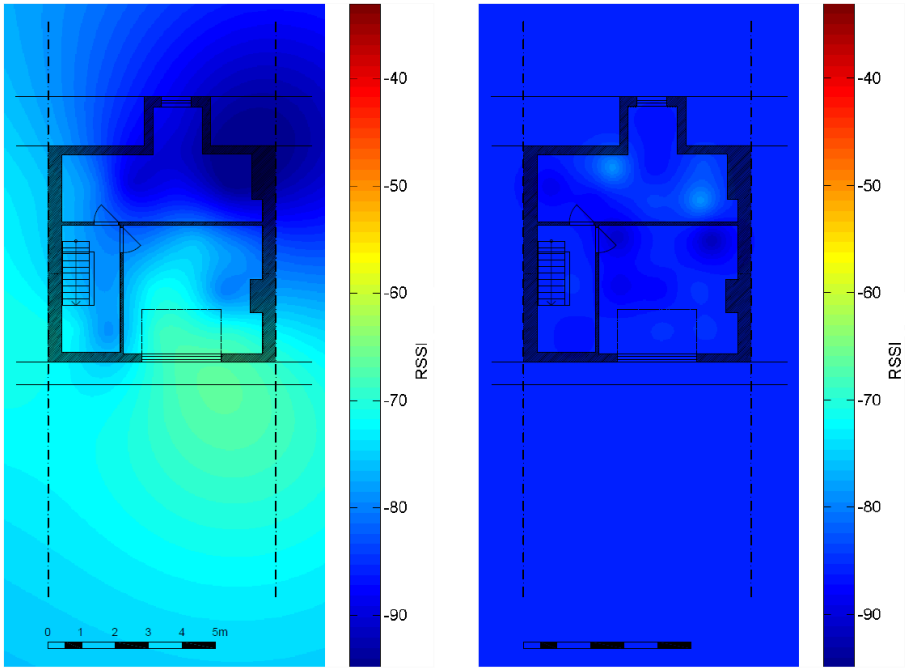

Figure 13: Second floor.

6.3 Wireless Friendly and Energy Efficient Buildings (WiFEEB) project - An Inductive Frequency Selective Surface for Use in Secure Facilities

This section builds on the published paper [140] (page 30) with practical measurements. These measurements were presented at the Photonics and Electromagnetics Research Symposium (PIERS) 2015 in Prague and were financially supported by Marie Curie Industry-Academia Partnerships and Pathways (IAPP) Grant Agreement 286333.

The measurement was performed in a University of Sheffield laboratory at its Buxton site. A vector network analyzer HP8720D, two antennas Schwarzbeck UHALP 9108A1 and metallised room with a frame for FSS were used (Fig. 14).

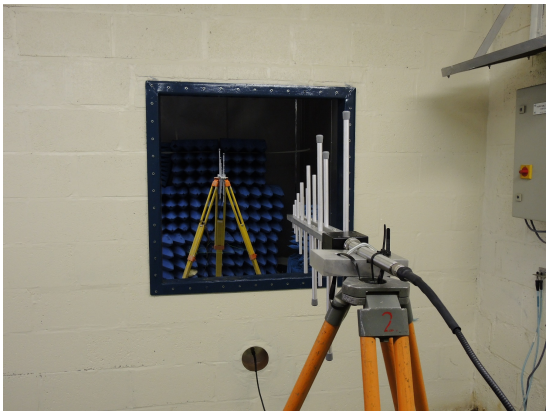

(a) Calibration without any FSS

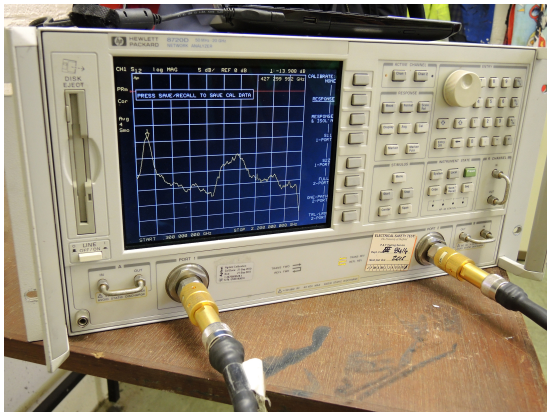

(b) VNA HP8720D was connected to two antennas Schwarzbeck UHALP 9108A1

Figure 14: Measurement setup.

Fig. 15 and 16 show the measured FSS made of a thin metallic sheet, FSS with thick edges (representing an FSS made of a thicker material), and FSS with thick edges and a mesh for optical transparency.

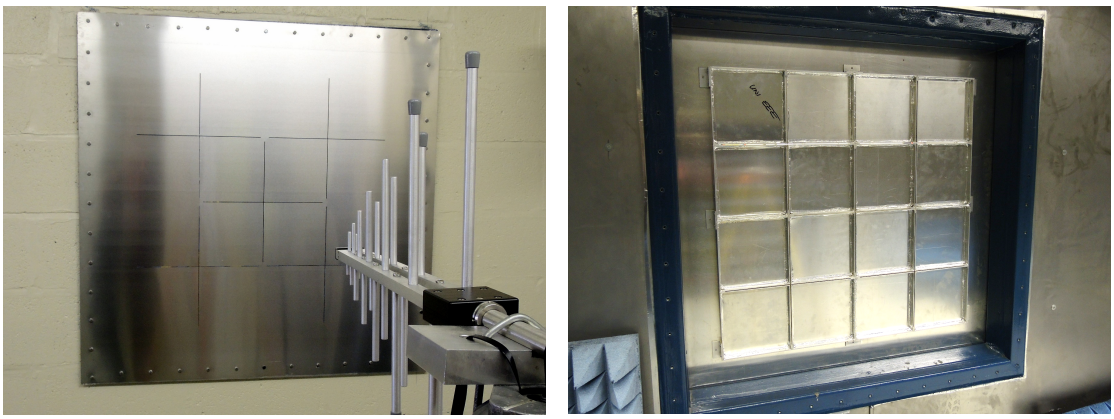

(a) FSS with thin edges

(b) FSS with thick edges

Figure 15: Measurement - optically non-transparent FSS design.

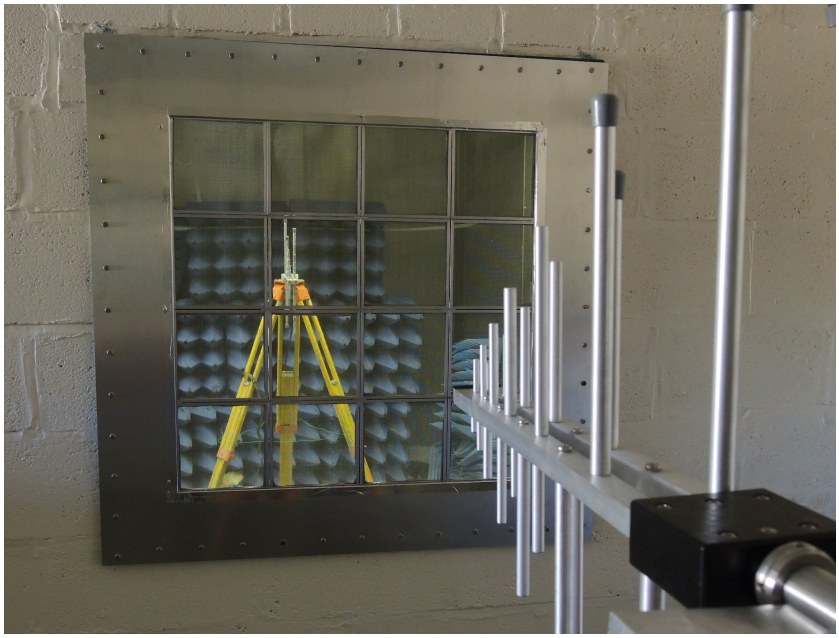

Figure 16: Measurement - optically transparent FSS design.

It was found (Fig. 17) the even small gaps in the structure decreased the attenuation (green trace). Therefore, a conductive tape was used for proper RF shielding at the edges of the plates and meshes (red and blue traces). It can be seen that the differences between the red and blue traces were negligible, so the optically transparent design did not affect the performance of the FSS.

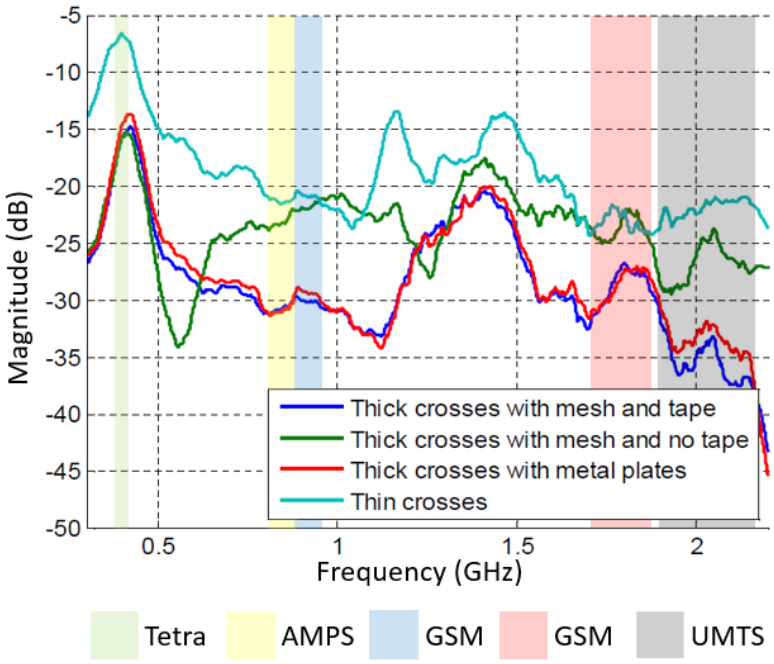

Figure 17: Measured results

6.4 GNSS Sector Antenna for Interference Mitigation and Localization Using a High-Impedance Reflector

This section presents construction details of the designed GNSS sector antenna (Fig. 18) based on high-impedance reflector. 3D printed components helped to achieve the desired angle between the reflector and the side walls.

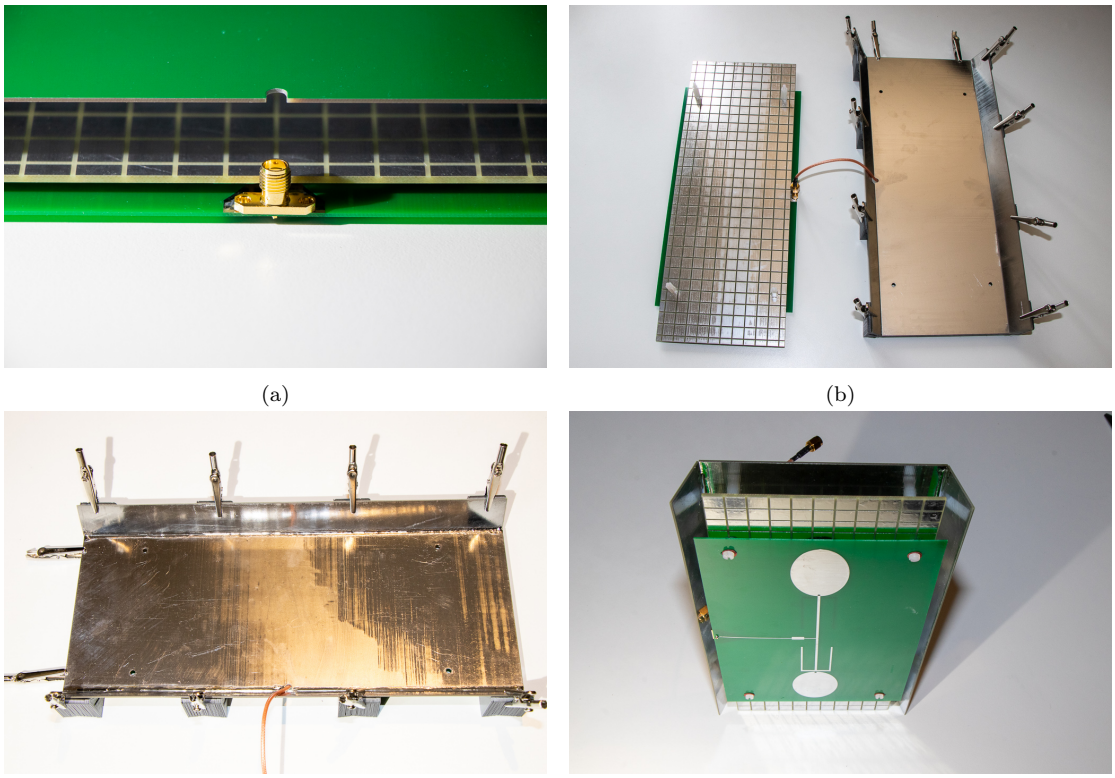

(a) (b)

(c) (d)

Figure 18: Construction details of the sector antenna.

The antenna was then tested and S11 parameters were measured (Fig. 19).

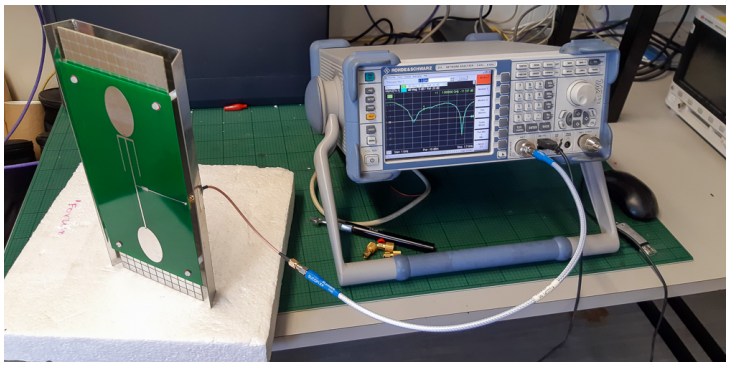

Figure 19: First measurement of S11 parameters. The final measurement was performed in the anechoic chamber.

As there was not enough space for the standard SMA male connector, the connector was later replaced with a semi-rigid coaxial cable (Fig. 20).

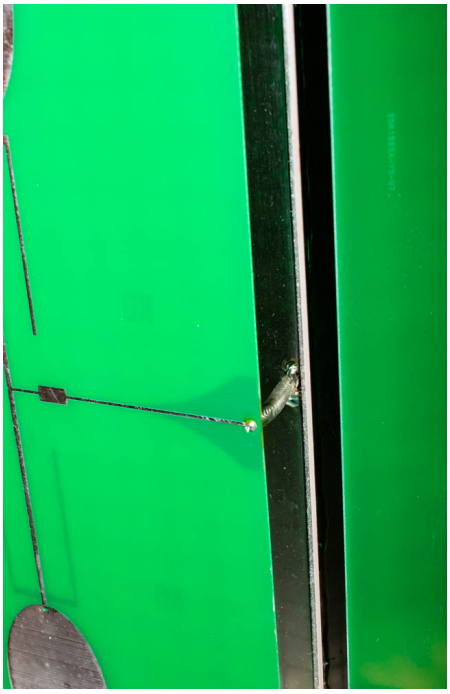

Figure 20: Final connection of the semi-rigid coaxial cable with the sector antenna.

Fig. 21 shows the connectors on the bottom of the entire antenna system and a tripod holder placed in the centre.

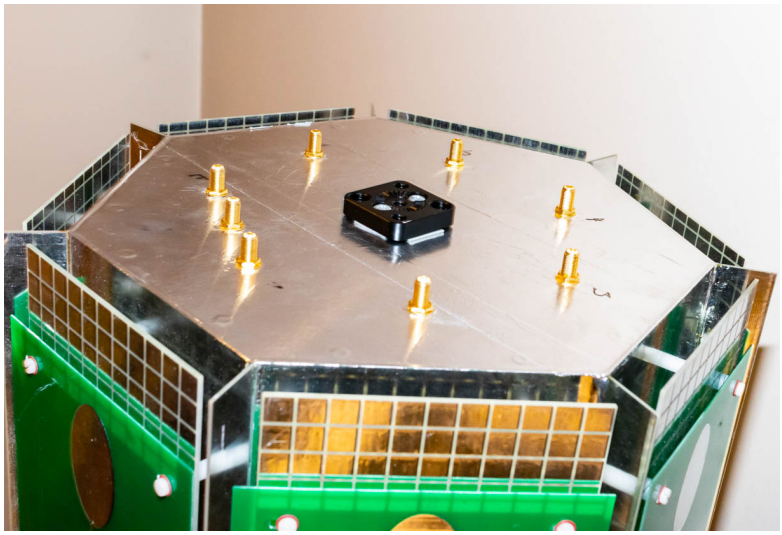

Figure 21: Bottom part of the antenna system.

The final assembled antenna system can be found in Fig. 22

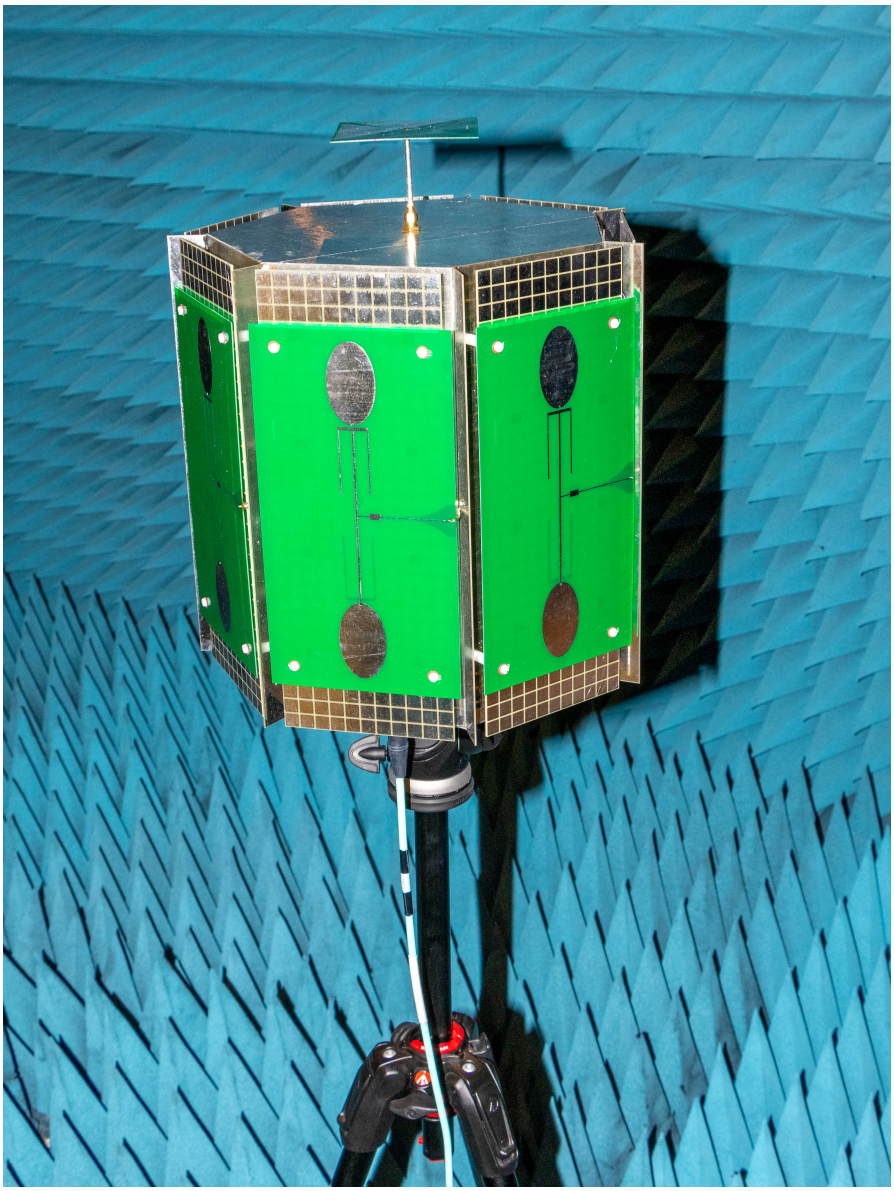

Figure 22: Anti-interference antenna system consisting of seven GNSS sector antennas based on metasurface and a top RHCP antenna based on a crossed dipole.

6.5 Compact Uplink RHCP 2.4GHz Short Backfire Antenna for Geostationary Amateur Radio Satellite Es'Hail-2 (QO-100)

This section provides details of the 2.4GHz RHCP satellite antenna.

Fig. 23 shows the main reflector. It was made of 2mm thick FR-4 material. The patch antenna made of 1.524mm thick Rogers 4350B substrate was placed and glued onto the reflector and then soldered to the SMA connector.

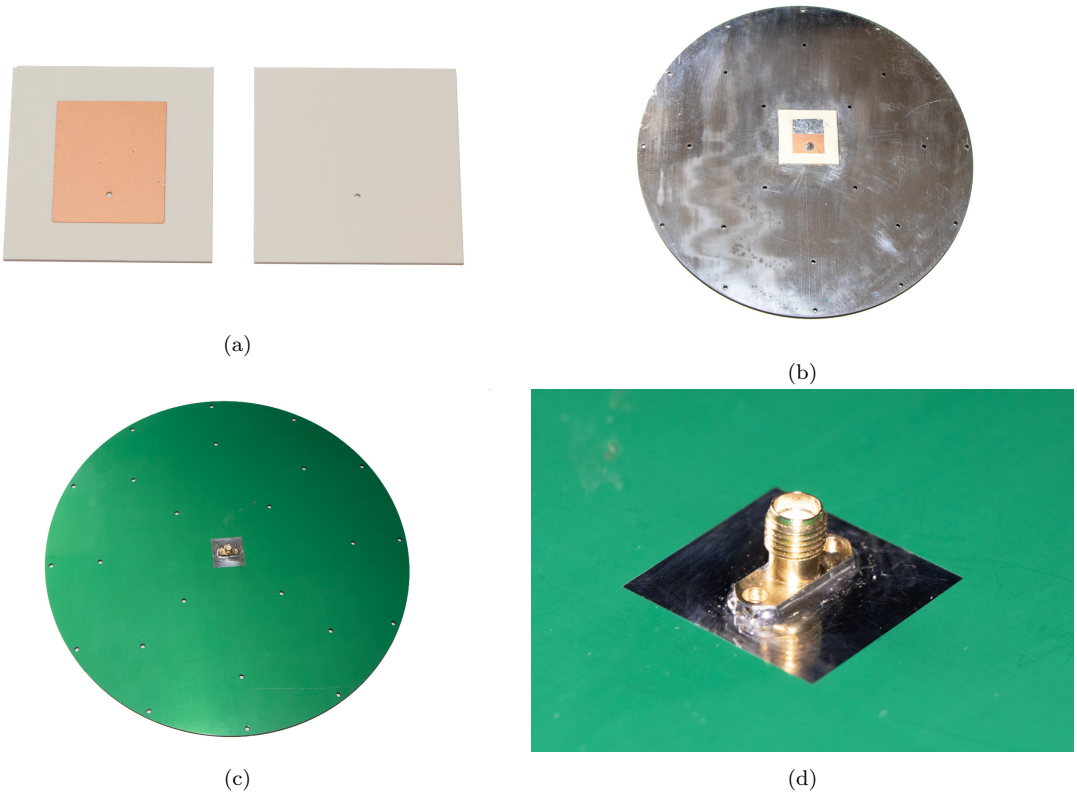

(a) (b) (c) (d)

Figure 23: Design of the main reflector: (a) patch antenna, (b) main reflector with the patch antenna (top view), (c) main reflector (bottom view), (d) detail of the SMA connector.

Furthermore, the rim was manufactured of Aluminium 6061 using a CNC machine and can be seen in Fig. 24. Fig. 25 shows the details of the tripod holder.

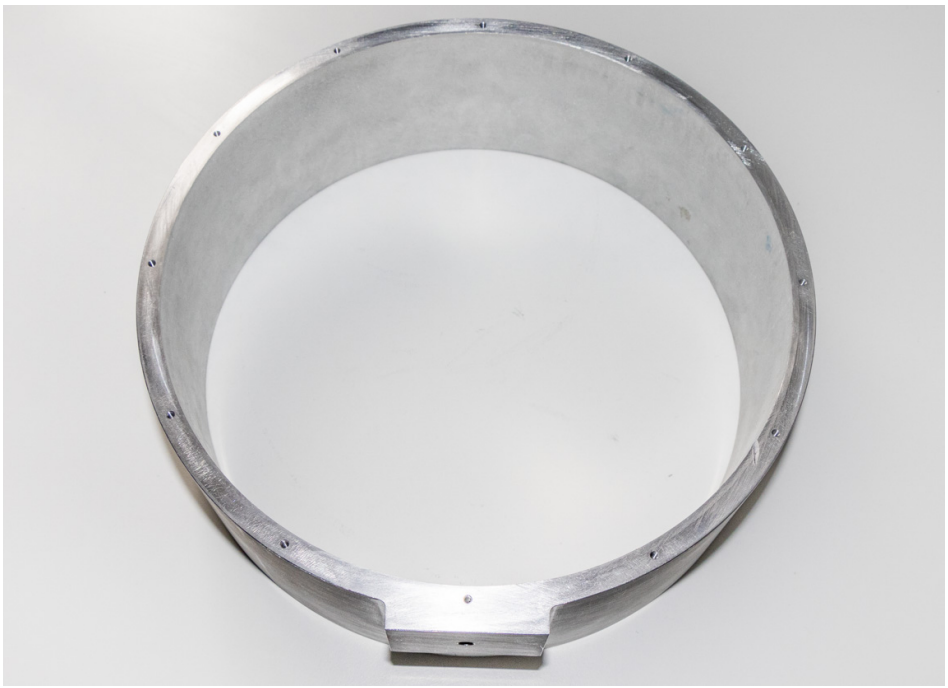

Figure 24: The back side of the rim.

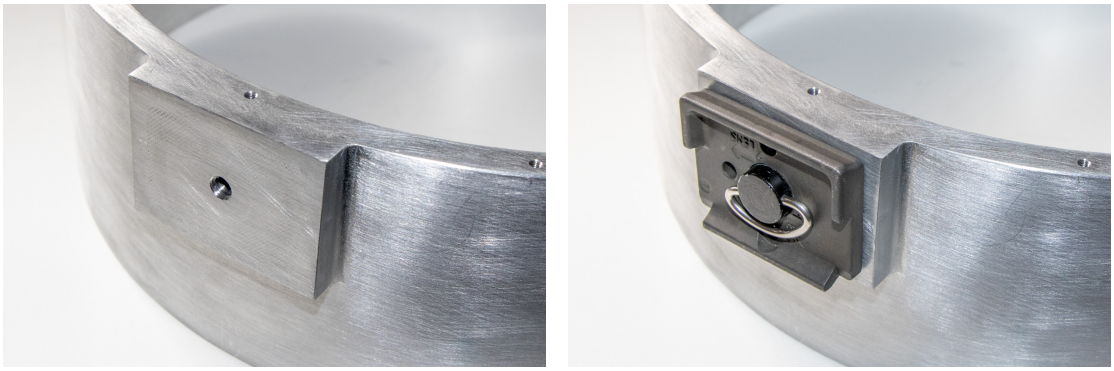

(a) (b)

Figure 25: Details of the tripod holder.

The assembled antenna without the rim is in Fig. 26. Nylon standoffs were used for creating spacing between the individual PCBs.

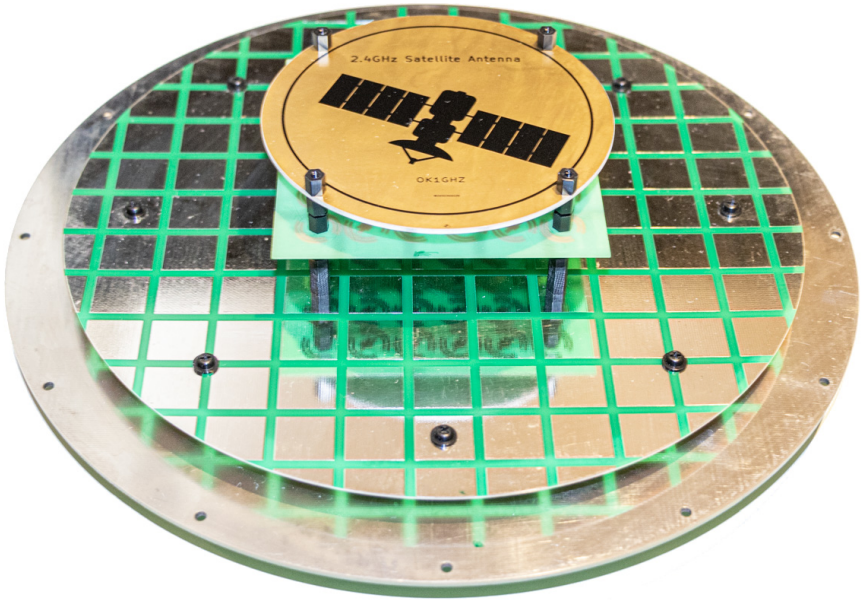

Figure 26: Assembled antenna without the rim.

Fig. 27 shows the fully assembled antenna. The antenna in the anechoic chamber prepared for the radiation pattern measurement can be seen in Fig. 28.

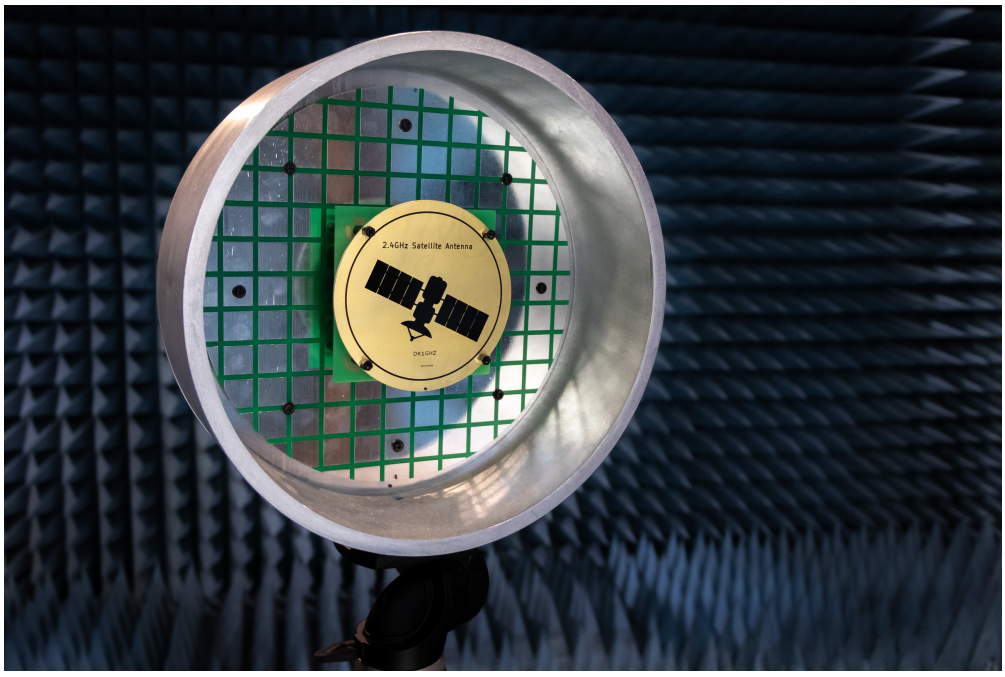

Figure 27: QO-100 2.4GHz RHCP satellite antenna based on metasurface.

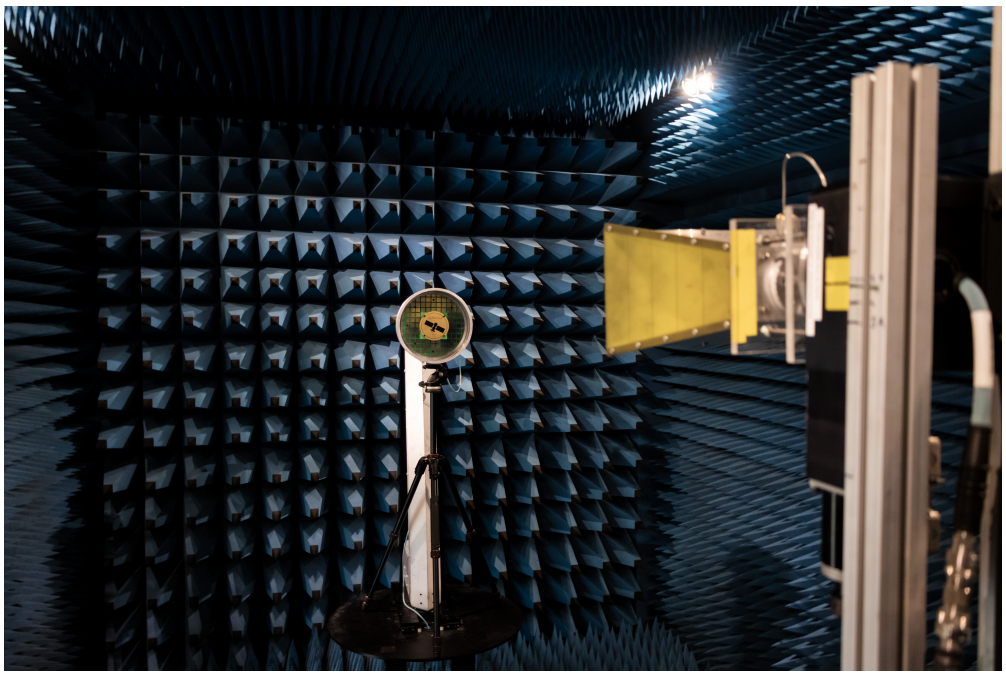

Figure 28: Antenna measurement in an anechoic chamber.

6.6 List of citations

The following list presents citations and reactions on author's publications.

- **An inductive frequency selective surface for use in secure facilities**
  - Garg, Shweta, Yadav, Sanjeev, Janyani, Vijay, Tiwari, Manish, Singh, Ghanshyam, and Minzioni, Paolo, A Triple Band-Reject Frequency Selective Surface for Broadband Applications, vol. 472. Springer Singapore, 2018, pp. 437-446. doi: 10.1007/978-981-10-7395-3_49.
  - V. Mishra, P. Singinal, S. Puthucheri, and D. Singh, "Development of a Novel Three Dimensional Frequency Selective Surface Using Polyurethane Foam for Communication Bands", in 2018 USNC-URSI Radio Science Meeting (joint with AP-S symposium): proceedings: 8-13 July 2018, The Westin Boston Waterfront, Boston, Massachusetts, USA /, 2018, pp. 133-134. doi: 10.1109/USNC-URSI.2018.8602592.
  - Garg, Shweta, Yadav, Sanjeev, Aseri, Kiran, Garg, Monika, and Noor, Darakshanda, "A novel reflective frequency selective surface for triple frequency applications," in 2017 International Conference on Computing, Communication and Automation (ICCCA), 2017, vol. 2017-January, pp. 1522-1525. doi: 10.1109/CCAA.2017.8230043.
  - S. Garg and S. Yadav, "A novel polarization independent transmissive type frequency selective surface for WiFi, WiMax & WLAN applications," in 2017 International Conference on Computer, Communications and Electronics (Comptelix), 2017, pp. 216-220. doi: 10.1109/COMPTELIX.2017.8003967.
  - P. Singhal, V. Mishra, S. Puthucheri, and D. Singh, "Analysis of three dimensional frequency selective surfaces for multiband operation," in ICIIS 2016: conference proceedings: 11th International Conference on Industrial & Information Systems: 3rd-4th December 2016., 2016, vol. 2018-January, pp. 770-773. doi: 10.1109/ICIINFS.2016.8263042.
- **A Sparse FSS for Control of Radio Coverage in Buildings**
  - A. G. Neto, J. Costa e Silva, D. C. G. Fernandes, L. M. de Sousa Duarte, and G. J. de Morais, "Recovering suppressed resonance frequency by bias lines in reconfigurable FSS," Journal of Microwaves, Optoelectronics and Electromagnetic Applications, vol. 20, no. 3, pp. 464-474, 2021, doi: 10.1590/2179-10742021V20I31193.

- **Reflective Switchable Polarization Rotator Based on Metasurface With PIN Diodes**
  - X.-M. Liu, "A Broadband Reflective Polarization Rotator", Beijing Youdian Daxue Xuebao/Journal of Beijing University of Posts and Telecommunications, vol. 44, no. 6, pp. 20-25 and 32, 2021, doi: 10.13190/j.jbupt.2021-035.
  - J. Zhang, W. Jiang, and K. Wei, "A switchable polarisation conversion/ in-phase reflection metasurface and its application", IET microwaves, antennas & propagation., vol. 15, no. 13, pp. 1688-1698, 2021, doi: 10.1049/mia2.12186.
  - X. Song et al., "Switchable metasurface for nearly perfect reflection, transmission, and absorption using PIN diodes," Optics express., vol. 29, no. 18, pp. 29320-29328, 2021, doi: 10.1364/OE.436261.
  - X. Yang, T. Qi, Y. Zeng, X. Liu, G. Lu, and Q. Cai, "Broadband Reflective Polarization Rotator Built on Single Substrate," Electronics., vol. 10, no. 8, 2021, doi: 10.3390/electronics10080916.
  - Reaction on LinkedIn